NISTIR 89-4080

NBS' Industry - Government Consortium Research Program on Flowmeter Installation Effects:

Summary Report with Emphasis on Research Period January - July 1988

G. E. Mattingly and T. T. Yeh

U.S. DEPARTMENT OF COMMERCE
National Institute of Standards and Technology
(Formerly National Bureau of Standards)
National Engineering Laboratory
Center for Chemical Engineering
Fluid Flow Group
Chemical Process Metrology Division
Gaithersburg, MD 20899

April 1989

NISTIR 89-4080

NBS' Industry - Government Consortium Research Program on Flowmeter Installation Effects:

Summary Report with Emphasis on Research Period January - July 1988

G. E. Mattingly and T. T. Yeh

U.S. DEPARTMENT OF COMMERCE
National Institute of Standards and Technology
(Formerly National Bureau of Standards)
National Engineering Laboratory
Center for Chemical Engineering
Fluid Flow Group
Chemical Process Metrology Division
Gaithersburg, MD 20899

April 1989

National Bureau of Standards became the National Institute of Standards and Technology on August 23, 1988, when the Omnibus Trade and Competitiveness Act was signed. NIST retains all NBS functions. Its new programs will encourage improved use of technology by U.S. industry.

U.S. DEPARTMENT OF COMMERCE
Robert Mosbacher, Secretary

NATIONAL INSTITUTE OF STANDARDS AND TECHNOLOGY
Raymond G. Kammer, Acting Director

NIST's INDUSTRY - GOVERNMENT CONSORTIUM RESEARCH PROGRAM ON FLOWMETER INSTALLATION EFFECTS: REPORT OF RESULTS FOR THE RESEARCH PERIOD JANUARY - JULY, 1988

G. E. MATTINGLY
T. T. YEH

FLUID FLOW GROUP
CHEMICAL PROCESS METROLOGY DIVISION
CENTER FOR CHEMICAL TECHNOLOGY
NATIONAL MEASUREMENT LABORATORY
NATIONAL INSTITUTE OF STANDARDS AND TECHNOLOGY
GAITHERSBURG, MD
20899

PREFACE

The research results reported in this document were produced with the support of a National Institute of Standards and Technology (NIST) initiated industry-government consortium. In this mode of operation, there is a high degree of interaction between the representatives of the consortium member companies and the NIST researchers. These interactions include: (1) the planning of the specific focus of the NIST research efforts, (2) the analyses of the results obtained, and (3) the conclusions drawn for the particular phase of the work. For this reason, it is pertinent to acknowledge both the support given to this phase of the research program and the technical contributions made by the representatives of the consortium members.

The current consortium members are alphabetically:

1. Ametek-McCrometer
2. Chevron Oil
3. Dow Chemical Co.
4. E.I. Dupont de Nemours
5. Ford Motor Co.
6. Gas Research Institute*
7. Gas Unie (The Netherlands)
8. Instrument Testing Service
9. ITT Barton
10. Kimmon Mfg. Ltd. (Japan)
11. NIST-B
12. Rockwell International
13. Rosemount

*Specific acknowledgment is due to Dr. Kiran Kothari of GRI. Both his support for this program and his technical inputs in the analyses of results and in the conclusions drawn are gratefully acknowledged.

NIST's Industry - Government Consortium Research Program on Flowmeter Installation Effects: Summary Report with Emphasis on Six Month Period Jan. - July, 1988.

G.E. Mattingly
T.T. Yeh

Fluid Flow Group
Chemical Process Metrology Division
Center for Chemical Technology
National Institute of Standards and Technology
Gaithersburg, Maryland 20899

ABSTRACT

This report presents results produced in a consortium-sponsored research program on Flowmeter Installation Effects. This project is a collaborative one that has been underway for three years; it is supported by an industry-government consortium that meets twice yearly to review and discuss results and to plan subsequent phases of the work. This report contains the results and conclusions of the recent meeting of this consortium at NIST-Gaithersburg, MD in Aug. 1988.

The objective of this research program is to produce improved flowmeter performance when meters are installed in "non-ideal" conditions. This objective is being attained via a strategy to (A) measure, understand, and quantify the salient features of the "non-ideal" pipe flows from such pipeline elements as elbows, reducers, valves, or combinations of these, (B) for selected types of flowmeters, correlate meter factor "shifts" relative to the features of these "non-ideal" pipe flows so as to be able to accurately predict meter performance in "non-ideal" installations, and (C) disseminate the resulting technology through appropriate channels such as publishing our results in pertinent journals and upgrading "paper" standards for flow measurement.

Specific results included in this report include research results for the pipe flow from a conventional, long radius elbow:

1. the distributions of the mean and the turbulence velocities in the axial and vertical directions,
2. the pressure loss measurements,
3. the performance of selected types of flowmeter installed downstream of this elbow, and
4. the demonstration that satisfactory performance for the selected meters can be predicted using the research results of this study.

INTRODUCTION

The increasing scarcity of fluid resources and the rising value of fluid products is placing new emphasis on improved fluid measurements. Improvement is sought from many starting points. Meters are being retrofitted into fluid systems that were not designed for them. This invariably means the flowmeters are being installed in "non-ideal" conditions. Increased accuracy levels are

desired for installed metering systems - either by upgrading the flow conditions that enter the meter or by replacing the device itself and/or its auxiliary components.

The industry-government consortium (members are listed in Appendix 1) research program currently underway at NIST is designed to help improve fluid metering performance in these situations.[1-4]* The design of the program is to produce a basic understanding of the flow phenomena that are produced in "non-ideal" pipe flows and to quantify those phenomena. When these phenomena and their quantified characteristics are correlated with the performance of specific types of meters, it becomes feasible to predict and achieve satisfactory measurements in "non-ideal" meter installations.

The experimental research program is based upon the measurements of pipe flows from selected piping configurations using laser Doppler velocimetry (LDV). Selections of piping configuration are done by consortium members; one or two such configurations can be done in one year.

The LDV techniques that have been and are being applied to determine pipe flows can also be used to measure the effects of other pipeline elements-valves, flow conditioning elements (for fluid velocity or pulsations, etc.), mixing devices, generic flowmeter geometries - or combinations of these. The resulting understanding provides the bases for improving the effectiveness of these devices and, in turn, for increasing the productivity of the continuous processes which depend upon them. [5,6]

In the present study, the fluid is water and the piping is 2 inch diameter, smooth stainless steel. Diametral Reynolds numbers range up to 10^5. According to the concepts of dynamic similitude, the results of the present research program should predict a range of other flows - both liquids and gases when pertinent parameters match those in our experiments.

It is concluded that when the performances of flowmeters - similar to or different from those selected to demonstrate the predictive scheme put forth here - are determined via calibration tests in these flows, it should be possible to produce correlations between meter performance and appropriate pipe flow parameters. When this is achieved - by flowmeter manufacturers or users alike - it should then be possible to predict satisfactory metering performance for these meters in similar "non-ideal" installations.

EXPERIMENTAL RESULTS:

In what follows, results are presented for the pipe flow from a single conventional, long-radius elbow oriented vertically so as to turn a fully developed, equilibrated, turbulent pipe flow into the horizontal pipe in which the measurements were made. Results include:

1. Mean Velocity Measurements. The right hand coordinate system used in what follows has an origin at the pipe centerline at the exit plane of the weld

* Square bracketed integers refer to references given below.

neck flange attached to our elbow. This origin is 1.21 pipe diameters downstream from the exit plane of our elbow.

The positive Z direction is downstream; the positive Y direction is upward; the X direction is therefore to the right looking upstream. The mean velocities in the X, Y, and Z directions are U, V, and W, respectively; the corresponding turbulence velocities, are u',v', and w'.

In the legends on the figures that will graph our measurement results, a letter convention will be used to indicate the piping configuration being studied. The letter "L" is used to indicate that long radius elbows are used (radius of centerline curvature is 1.5 times the inside pipe diameter) and when this "L" is followed by a letter designation such as "-Y" this means the inlet pipe length has flow directed in the negative Y direction of the coordinate system described above. Thus, "L-Y" indicates that a single elbow receives a downwardly directed pipe flow and turns it horizontally into the positive Z direction.

All quantities are nondimensionalized using the bulk average pipe flow velocity to normalize all velocities and using the pipe inside diameter to normalize lengths. For the single elbow configuration, the distributions of the mean components of the streamwise velocity along the horizontal and vertical diameters for successive downstream locations are plotted in Figure 1(a) and (b). The diametral Reynolds number is 10^5. The dashed line in both figures is the corresponding power law profile for these conditions i.e., smooth pipe; the exponent for this profile is n = 7 as shown on the figure. These results show the symmetry about the pipe centerline of the streamwise velocity profile along the horizontal diameter. The deviations from the power law profile at the most upstream location of Z = 1.5 indicate that the slow core of this profile is about 40% of the bulk velocity slower. With downstream distance these deviations diminish. Near the pipewall there are layers of fluid which move faster than the power law values by some 20% of the bulk velocity.

Figure 1(b) shows similar deviations in the center core of this pipeflow and the measured profile along the vertical diameter is not symmetrical about the center of the pipe. The fast layers of fluid near the bottom of the pipe are some 30% of the bulk flow faster than the power law values. With downstream distance, these deviations decrease so that at the Z = 22 location, the core flow is only 10% of the bulk velocity slower than the power law values at the center of the pipe.

Figures 2(a) and (b) present the streamwise velocity profiles along horizontal and vertical diameters, respectively, for diametral Reynolds number of 10^4. As before, the dashed line shows the corresponding power law profile, for which n = 6.3 as shown on these figures. For the profile along the horizontal diameter deviations similar to those shown in figure 1(a) are noted at both Z = 1.5 and Z = 5. However, at the Z = 22 location this lower Reynolds number pipeflow closely agrees with the power law distribution. Similar results are found for the profiles along the vertical diameter.

Figures 3(a) and (b) present the vertical velocity profiles along horizontal and vertical diameters, respectively, for diametral Reynolds number of 10^5. Here, the fully developed pipeflow is shown by the dashed line which is everywhere zero. The distributions shown in figure 3(a) indicate that at Z = 1.5 the upward vertical velocities near the pipewall are 15% of the bulk velocity. At the centerline; the downward velocity is 20% of the bulk velocity. As before, with downstream distance these deviations diminish so that at Z = 22 the vertical velocity is only about 1 - 2% of the bulk velocity at radial locations of X = $\pm$ 0.3 to 0.4.

Figure 3(b) shows that the vertical velocity along the vertical diameter is negative everywhere. Again, the dashed line pertains to the corresponding fully developed profile. Just above the pipe centerline at Z = 1.5 the magnitude of the negative velocity is 25% of the bulk velocity.

Figures 4(a) and (b) show the vertical velocity distributions along horizontal and vertical diameters for dimetral Reynolds number 10^4. The deviations from the dashed (fully developed) profile are noted to be smaller than their counterparts in figures 3(a) and (b).

Some early conclusions that can be drawn from figures 1 - 4 are that several Reynolds number effects can be noted. The first is that the initial secondary flows produced by this elbow in these pipeflows have greater non-dimensional velocities at the higher Reynolds number. Secondly, these secondary flows diminish more rapidly with downstream distance at the lower Reynolds numbers due to increased viscous diffusion. The decay of these secondary flows with downstream distance should occur more rapidly if the inner pipe wall were less smooth, [6].

2. Turbulence Measurements. Turbulent velocity components in both the streamwise and vertical directions were measured traversing both horizontal and vertical diameters. Results are normalized using the bulk average velocity and comparisons are made with results previously available.

Figures 5(a) and (b) present results for the streamwise component of the turbulent velocity at successive streamwise locations for diametral Reynolds number 10^5. Given also in these figures by the dashed lines are the distributions measured by Laufer [8] in an airflow at Reynolds number 4×10^5. These results show both qualitative and quantitative differences from Laufer's results. At the most upstream location the horizontal profile is symmetrical about the pipe centerline. The peaks in this profile rise to about 14% of the bulk average velocity and these occur at radial locations beyond the zero crossing points of the vertical velocity profile shown in figure 3(a). With downstream distance these profiles change to conform qualitatively with Laufer's results, but quantitative differences remain. The profile along the vertical diameter shown in figure 5(b) indicates that at the most upstream location the profile peaks at a single location about midway between the centerline and the bottom of the pipe. This peak value is some 14% of the bulk average velocity. With downstream distance, this distribution changes rapidly so that at Z = 5, the peaked distribution has decreased to some 10% of the bulk velocity and the profile is quite flat. By Z = 22 the profile approaches at least qualitatively that of Laufer as shown by the dashed line.

Figures 6(a) and (b) present results for the vertical component of the turbulent velocity as measured along horizontal and vertical diameters, respectively, for Reynolds number of 10^5. Laufer's data is again shown by the dashed line. At the most upstream station the distribution along the horizontal diameter is symmetrical about the pipe centerline with peaks of about 15% of the bulk velocity occurring at about $X = \pm 0.10$. With downstream distance, these peaks diminish and their radial locations occur further from the pipe centerline. At $Z = 22$, the measured distribution approximates qualitatively that of Laufer but again quantitative differences are evident. Figure 6(b) presents the profile of the vertical component of the turbulent velocity along the vertical diameter for Reynolds number of 10^5. At the most upstream location the peak in this distribution occurs below the pipe centerline as noted in the profile of the streamwise component of the turbulent velocity shown in figure 5(b). However, this peak - while rising to about the same value of 14% of the bulk velocity - is a broader one and is located nearer the pipe centerline. With downstream distance this peak diminishes rapidly. However, at $Z = 22$ it is noted that both qualitative and quantitative differences from the Laufer results remain.

It is concluded from these turbulence measurements shown in figures 5 and 6 that this pipeflow from this elbow contains very energetic turbulence. These levels of turbulence and the pipelengths over which they prevail produce potentially useful mixing environments, see [5].

3. Skew Angle Distributions. The secondary flow measurements described above can be characterized and parameterized in many ways. In order to productively use the resulting parameters to predict the performance of a flowmeter in these "non-ideal" flows, the operational principles of the flowmeter need to be considered. For example if the meter is sensitive to particular vorticity distributions, then particular vorticity parameters should be explored. On the other hand, if the meter is sensitive to turbulence parameters, then turbulence parameters should be examined. The next step in the process of devising the scheme to predict the performance of the specific meter in these "non-ideal" pipe flows is to correlate the developed parameters with calibration data for the specific meter in these flows. Then, using the parameter for which the correlation is the most successful, the performance of this meter can then be predicted for meter installation positions downstream of the particular piping configuration for the pertinent parameters, etc.

To quantify the time averaged swirl features of these pipe flows, a range of parameters were formulated. These involve both linear and angular momentum flow characteristics. These include:

Skew Angle = $\tan^{-1}(V/W)$

Skew Flux = WV

Swirl Fluxes:

1) $S_x = W(W-1)Y$
2) $S_y = W(W-1)X$
3) $S_z = WVX$
4) $S_\theta = WV(X-X_i)$
5) $S_i = WV_i r_i$

where, in addition to the quantities defined above X_1 and X_2 indicate the X coordinates where V = 0 along the negative X axis and the positive X axis, respectively, (i.e., approximately $\pm$ 0.25); r_1 and r_2 are the displacements along the X axis from the positions where V = 0, i.e., $\pm$ 0.25.

Parameters are presented graphically.

Figures 7(a) and (b) present skew angle distributions along horizontal and vertical diameters, respectively, for diametral Reynolds number 10^5 for successive downstream locations. Extreme values in figure 7 (a) are almost -15° on the centerline and about +8° near the pipe wall at the most upstream location. With downstream distance, the cross-stream distribution decreases rapidly, so that by Z = 22, the angle is less than 1°. In figure 7(b), it is noted that, at the most upstream location, the skew angle reaches a negative peak of more than -15°. This occurs about 10% of the pipe diameter above the pipe centerline. At the Z = 5 location, this extreme value is reduced to about -6° and it occurs closer to the centerline, at about 5% of the pipe diameter above it.

Figures 8(a) and (b) present the skew flux distributions over horizontal and vertical diameters, respectively, at different streamwise locations for diametral Reynolds number 10^5. Although the quantitative differences are noted by comparison to figures 7(a) and (b), the qualitative characteristics are identical.

Figure 9 presents the swirl flux (defined above as s_x) distributions over the vertical diameter for diametral Reynolds number 10^5. At Z = 1.5, the distribution has the extreme value of about -0.12 near the bottom of the pipe. The interpretation could be made here that, relative to the bulk average velocity, the pipeflow is imparted a positive torque about the X axis at this streamwise station. From this extreme value, the distribution increases through zero at a radial location about 30% of the diameter below the pipe centerline. From this point to the pipe centerline, this swirl flux is positive because the streamwise velocity W is less than unity (the bulk velocity) everywhere above this radial position as shown in figure 1(b). Accordingly, the swirl flux s_x is negative above the pipe centerline indicating this pipe flow is imparted, relative to the bulk flow, a negative torque. With downstream distance, figure 9 shows that this swirl flux decreases monotonically toward the "S" shaped distribution for the ideal flow that is approximated by the profile shown for the Z = 22 position.

Figure 10 presents the results for swirl flux, s_y along the horizontal diameter at successive axial locations for diametral Reynolds number 10^5. Again, it is noted that considerable variations occur between the results at the different axial locations. However, there is a monotonic progression toward the S-shaped "ideal" distribution that is approximated by the dotted line through the "x" symbols.

Results for the swirl flux, s_z along the horizontal diameter are shown via figure 11 for Reynolds number 10^5. The "ideal" distribution is everywhere zero. These distributions indicate the alternating nature of the torque about the Z axis imparted to the fluid in this flow configuration.

Because the results presented via figures 1-4 clearly indicate the dual-eddy nature of this pipeflow, a swirl flux parameter can be devised to quantify the strength of these. The eddy swirl flux, s_e is such a parameter and results for it along the horizontal diameter for Reynolds number of 10^5 are shown in figure 12. The decrease with downstream distance of these distributions quantifies the axial decay in the Z direction of the torque about the axis of the eddy. At Z = 22, the distribution is essentially zero all along the horizontal diameter.

3. Axial Decay Characteristics. As noted in all of the above figures, the secondary flow characteristics decay with downstream distance. Most of these results have shown data measured for the case of diametral Reynolds number 10^5. Although not shown here, the decay for the lower Reynolds number case of 10^4 is more rapid than that of 10^5. Results for these decay phenomena will be shown below for the integrated swirl characteristics:

1) Pipe swirl number:

$$S_p = \int_{-0.5}^{0.5} |WVX| dX$$

2) Eddy swirl number:

$$S_e = \int_{-0.5}^{0} WV(X-X_1)dX + \int_{0}^{0.5} WV(X-X_2)dX$$

3) Model eddy swirl number:

$$S_m = \int_{-0.5}^{0.5} W\ (V_2 r_2 - V_1 r_1)dX,$$

where V_1 and V_2 are the vertical velocities due, respectively, to the model vortex distributions placed along the negative and positive X axes, and r_1 and r_2 are the radial displacements from the axes of the eddies, respectively, along the negative and positive X axis.

4) Lateral swirl number:

$$S_x = \int_{-0.5}^{0.5} W(W-1)YdY$$

5) Skew angle:

$$S_a = (A_+ - A_-)/2$$

where A_+ and A_- are, respectively, the maximum positive and minimum negative values of the local swirl angle, i.e., $\tan^{-1}(V/W)$ in degrees regardless of where these occur along the horizontal diameter.

The decay of the above described parameters with distance downstream from the exit plane of this elbow for a diametral Reynolds number of 10^5 are given in figure 13. To contain all these distributions on this ordinate scale, it has been necessary to reverse the sign of S_x and to divide S_a by 500. The significant feature that pervades all of these decays is that they do not occur linearly with downstream distance.

The mean velocity measurements presented in figures 1-4 enable further modeling to be applied to characterize these eddies. Results are presented in Appendix 2.

The pipeflow measurement results presented above can be characterized in terms of their deviations from the corresponding ideal flow. To do this, "deviant" parameters are defined as follows:

$$DWO = W_c - W_{cs}$$

$$DW1 = \int |W(W-1)|\,dX$$

$$DW2 = \int W(W-1)\,dX$$

$$DW3 = \int |W(W-1)|\,dY$$

$$DW4 = \int W(W-1)\,dY$$

$$DVO = V_c$$

$$DV1 = \int |WV|\,dX$$

$$DV2 = \int WV\,dX$$

$$DV3 = \int |WV|\,dY$$

$$DV4 = \int WV dY$$

where quantities are those described previously and where the subsricpt "c" refers to the respective centerline quantity and the subscript "cs" refers to the centerline quantity for the ideal, straight pipe situation.

Figure 14 presents several of these deviant parameters versus downstream distance for the $Re_D = 10^5$ condition. All of these indicate non-linear decay with donwstream distance. The centerline deviations have been plotted with the sign reversed for convenient appearance on this graph. It is noted that the deviant for the vertical component on the centerline, -DVO decays to essentially zero within about twenty diameters. The deviant for streamwise component, -DWO indicates that at the twenty diameter point, the difference is between 15% and 20% of the bulk velocity. The integrated deviants DW1 and DV1 show similar trends. The vertical velocity deviant decays to essentially a zero level by the twenty diameter point, but the streamwise deviant decays only to the 5% level by this twenty diameter position.

It is concluded from these deviant distributions that the different velocity component profiles do not decay together. The streamwise component requires greater pipelength distances to dissipate deviant parameters - both local and integrated effects.

Figure 15 presents results for the axial decay of the parameter, S_p for $Re_D = 10^6$. The two lines shown correspond to the fitted exponential relationships given in the figure. It is noted that the exponential decay constants are about 1/7. Comparing this decay constant with that for the double elbow-out-of-plane configurations, it is noted that this constant is about three times larger, i.e., 1/7 vs. 1/20, [1-2]. Furthermore, it is expected that for reduced Reynolds number, this decay constant for the single elbow flow would increase.

Figure 16 presents comparisons between our data for the deviant DVO and two exponential fits to this data for $Re_D = 10^5$. The exponential constants are noted to be about 1/5. As indicated in figure 14, the decay constant for the deviant DVO is larger than that for DWO. Therefore, the decay constant for DWO would be greater than 1/5.

Figure 17 presents decay constant results versus Reynolds number for a range of swirl and deviant parameters. As noted above, the decay constants decrease with Reynolds number. The swirl parameters do not decrease as rapidly with Reynolds number as do the deviant parameters DWO and DW1.

Table 1 presents the quantitative results for the decay constants for the secondary flow parameters for our pipeflow from our single elbow for Reynolds numbers 10^4 and 10^5. As noted previously, the earlier described Reynolds number effects of reduced decay rates with increasing Reynolds numbers pervades all of these parameters. The two-parameter power law that describes these relationships has constants that are given in the two columns at the right of this table.

FLOWMETER RESULTS:

In the descriptions that follow, specific types of meters are selected and used to demonstrate the degree of success that can be expected in using the strategy described in the INTRODUCTION section above in attaining accurate flowmetering when meters are installed in "non-ideal" locations. The specific types of meters selected are turbine-type and orifice-type. For the orifice-type meters several beta ratios (orifice hole to inner pipe diameter) were used.

1. Turbine-type meter. As described in the INTRODUCTION above the initial step in the procedure is to calibrate the selected meter in several locations at varying distances from the piping configuration that produces the non-ideal pipe flows - in this case the single elbow. Results are shown in figure 18 where the turbine constant is given via the Strouhal number:

$$St = fD/W_b$$

where, in compatible units, f is the output frequency of the turbine meter, D is the inner pipe diameter and W_b is the bulk average velocity through the pipe. Since the pipe diameter, D is a constant under the constant temperature conditions of these tests, this Strouhal number is directly proportional to the meter's K factor (in pulses per volume) that is the conventional manner of describing turbine meter performance. The abscissa in figure 18 is given in terms of Reynolds number

$$R_e = DW_b/\nu$$

where, in compatible units, D and W_b are as described above and ν is the fluid's kinematic viscosity. Again, since the diameter D is constant and since the bulk average velocity is essentially proportional to the turbine output frequency, f, the Reynolds number is proportional to the ratio f/ν which is the conventional abscissa for plotting turbine meter performance-the universal viscosity curve.

The data points plotted are averages of five individual determinations of the meter factor; standard deviations about these means would produce error bars that are of the same order as the scale of the symbol used to plot the mean value. Figure 19 shows this by plotting together each data point from the calibration of this meter in the ideal installation condition - i.e., with more than 200 diameters of straight, constant diameter piping preceding this meter.

Figure 18 shows data for this meter taken in four locations - an "ideal" location which in these tests means more than 200 diameters of straight constant diameter pipe precede the meter. The three other locations are given in the legend of figure 18 where the downstream distance in diameters from our single elbow is given. These results show that this meter's K factor is reduced when this meter is installed near this single elbow and the nearer the meter is installed to this elbow the more the reduction. If this meter was used in these "non-ideal" installation conditions with the "ideal" K factor

assumed to apply, this meter would "under-read" the fluid flow rate since flow rate varies inversely with meter factor in pulses per volume. The results shown in figure 18 indicate that when this meter is installed twenty or more diameters downstream of this elbow, these secondary flows do not perturb the performance of this meter. Figure 19 shows the uncertainty bands ($\pm$ one standard deviation) at each flowrate for the turbine meter calibration data in the "ideal" installation.

To correlate this meter's performance with the specific parameters, we have opted to take the average of the mean Strouhal numbers for Reynolds numbers above 40000. In this way, a single value of Strouhal number and the standard deviation error bars over this Reynolds number range can be used to describe this meter's performance at each location. Thus, the desired correlation can be done using this average value and the corresponding value of the profile parameter. This is shown in figure 19; the average value and the error bars are indicated on the right ordinate of the figure.

Figure 20 presents the normalized meter constants - i.e., Strouhal numbers as these are found to depend on downstream distance from this single elbow. Normalization is done using the Strouhal number obtained in the "ideal" installations. The dashed lines connect the error bars described above. The meter performance for the ideal installation - i.e. unity with pertinent error bars is shown along the right hand ordinate scale and labelled "straight pipe". The vertical spacing between the dashed lines is a measure of the standard deviation of all the data taken over this flow range. Thus, these error bars are indicative of the meter's non-linearity and do not indicate imprecision at a single flow rate.[9] When these normalized meter factors are plotted versus the different profile parameters one obtains a picture of the respective correlation. Figure 21 presents the normalized meter performance versus the pipe swirl number, S_p. The dashed lines connect the error bars for the two extreme installations: 1) the "ideal" one for which $S_p = 0$ and 2) for that where the meter was installed closest to the elbow. The dotted line connects the mean meter factors from these same locations.

Now, if one were to use this dotted line connecting these means as the basis for predicting the meter's performance at any installation location between these extremes, the success of this prediction method can be judged by the differences between the dotted line and the meter results obtained at $Z = 8.7$ and 20.3, respectively. It is noted that this prediction scheme works well and appears to give a more accurate prediction at the $Z = 8.7$ location than at $Z = 20.3$.

Figure 22 presents normalized meter performance plotted versus the skew angles, S_a. The dashed and dotted lines are drawn as described above. Here, the dotted prediction line is found to give slightly improved results compared to the pipe swirl number, S_p. In addition, it is noted that this process gives better results at the $Z = 8.7$ location than at $Z = 20.3$.

It is therefore concluded that our strategy for predicting flowmeter performance in "non-ideal" installations is successful. It is noted to work with different degrees of success depending upon the particular profile parameter chosen to correlate meter performance. It also should be noted that

although the above described process works slightly better with the skew angle parameter, S_a compared to the pipe swirl number, S_p - this is not to say that all turbine meters will duplicate this correlation. It may well be that other designs will correlate better with other parameters - either those listed above or perhaps others.

2. Orifice-type meters. When an orifice-type meter is selected for demonstration of the degree of success that can be expected using our strategy, results are shown in what follows for three different beta ratios. The three beta values selected for this demonstration are 0.363, 0.500, and 0.750.

a) Beta = 0.500. Figure 23 presents the results for the calibration tests performed on the orifice-type meter containing an orifice plate having beta ratio 0.500. The data presented pertain to differential pressures measured via flange taps oriented at the top of the pipe. The streamwise locations of the orifice plate are Z = 1.7, 7.5, 19.1 and the "ideal" location which, as specified above for the turbine-type flowmeter, is the installation where the meter is preceded by more than 200 diameters of straight, constant diameter piping. The values plotted in figure 23 are the averages of five individual determinations made at each flowrate. The standard deviations of these means produces error bars which are of the order of the size of the symbols used to plot the points on figure 23. These error bars are shown in figure 24 for this orifice-type meter installed 19.1 diameters downstream of the elbow.

The results shown in figure 23 indicate that the secondary flows produced by this elbow cause the orifice discharge coefficient to decrease from the value for the ideal installation. Thus, if this were not known and if this meter were used in these "non-ideal" locations with the ideal discharge coefficient assumed to apply, this meter would "over-read" the actual flowrate since, conventionally, flowrate is proportional to discharge coefficient. From the data presented in figure 23, this "over-reading" could amount to about 2%. Since orifice-type flow meter accuracies have been conventionally specified-depending upon a number of other factors - to be about $\pm$ 0.5%, this 2% systematic offset is almost a factor of four in excess of this specified accuracy.

From the pipeflow profile measurements presented previously, it is tentatively concluded that the reasons for the decreased discharge coefficients shown in figure 23 are the influences these secondary flow effects have on the differential pressure measurements made across this meter. The form of the non-dimensional discharge coefficient indicates that a reduction of this ratio can be produced by several individual, or combinatorial effects. For example, any artificial increase in the pressure measured at the upstream tap location could be a cause. Such an artificial increase could be due either to centrifugal effects of the mean flow or to the enhanced levels of the turbulence producing over-registration in our pressure sensing configuration. Alternatively, the discharge coefficient could be reduced through a reduction in the pressure sensed at the downstream tap. This could occur if the secondary flow effects produced by this elbow were to pass through this 0.5 beta orifice plate and cause the pressure in the eddy system trapped behind this plate to be reduced. Of course, combinations of both of the above

descriptions could also occur to produce the trends noted. From the data shown in figure 23, this meter - even 19.1 diameters downstream of this elbow - has its discharge coefficient shifted downward between about 0.2% to 0.5%.

As done before for the case of the turbine-type meter, the performance of this orifice-type meter will be based upon averaged discharge coefficient. To do this we select the flowrate range for diametral Reynolds numbers greater than or equal to 30,000. Over this range the individual means for discharge coefficient are themselves averaged and error bars are based upon the maximum and minimum differences between the extreme values and this average. Results can be plotted versus distance from the elbow.

Figure 25 shows these discharge coefficient results as normalized using the "ideal" values. The ideal installation performance is shown at the right hand ordinate and labelled "straight pipe". Again, the mean values in this plot are connected by the dotted line; the dashed lines connect the error bars about these means. It is noted that this distribution for discharge coefficient is not linear with distance from the elbow.

Figure 26 presents normalized discharge coefficient results for the beta 0.500 orifice plate plotted versus the pipe swirl number, S_p. The dotted line connects the averages of the means for the ideal installation conditions and for the results obtained for this meter installed 1.7 diameters from the elbow. Using the dotted line as the basis of our prediction scheme, then at the Z = 7.5 or 19.1 installation positions where the pipe swirl numbers are 0.010 and 0.002, respectively, the predictions for the normalized discharge coefficients would have been 0.9925 and 0.998. When our meter is installed in these locations the actual values were found to be 0.993 and 0.9975, respectively. On the bases of these agreements, it is concluded that our strategy works very well for this orifice-type meter.

b) <u>Beta = 0.363</u>. Figure 27 presents orifice-type meter calibration results for our case of a beta 0.363 plate. The positions of this meter relative to the single elbow are the same as those for the beta 0.500 plate described above. The position of the pressure taps for this meter are oriented at the top of the pipe. It is noted that, for these results, the discharge coefficient is reduced due to the effects of these secondary flows. However, the reduction in these discharge coefficients is in each case smaller than for the beta 0.500 plate. To characterize these disturbance effects at each of the installation positions, a flowrate range is selected to be

$$14000 \leq Re \leq 45000$$

and over this range the average of the means is taken together with error bars produced in the same manner as described above. These results can be plotted as before.

Figure 28 presents results for the normalized discharge coefficient versus distance downstream from the elbow. Again, the non-linear characteristics of the distribution is noted. The ideal installation performance - i.e., unity with appropriate error bars is labelled "straight pipe" on the right ordinate scale.

Figure 29 presents, for the beta 0.363 orifice plate, the normalized discharge coefficient results plotted versus the pipe swirl number, S_p. The dotted and dashed lines are as before. Using the ordinate values of the dotted line to predict the respective "non-ideal" installation performance as done in the previously described cases, the open circle points with the error bars are the corresponding test results for this meter in these positions. The differences are considered small and the conclusion is drawn that our strategy is successful for the beta 0.363 orifice plate.

c) Beta = 0.750. The last orifice-type test is done for a beta 0.750 plate. Results for the calibration testing for this meter downstream of the single elbow are presented in figure 30 for the same positions as described for the previous cases. The pressure taps are oriented at the top of the pipe. These results indicate that this beta ratio shows that the discharge coefficient is reduced by these secondary flows. This reduction is also noted to be the largest of the three cases tested - the downward shift noted from figure 30 is about 6%.

Figure 31 presents the results for the averaged discharge coefficients - taken over the flowrate range:

$$40000 \leq Re \leq 100,000$$

normalized as done previously and plotted versus the downstream distance from the single elbow. Dotted and dashed lines are drawn as before. The distribution is noted to be non-linear in the Z coordinate. The non-linearity of the calibration test data shown in figure 30 is reflected in the close vertical spacing of the dashed lines.

When the normalized discharge coefficients are plotted versus the pipe swirl number, S_p the results are shown in figure 32. Dotted and dashed lines are drawn as before. The success of the strategy is shown by the close agreement between the open circle points and the corresponding ordinates of the dotted line. Again, it is concluded that the strategy works very well.

It is therefore concluded that our prediction scheme works very well for all three of the beta ratios tested. The shifts determined for the discharge coefficients for these plates relative to the "ideal" installation values is negative for all cases; this could lead to meter "over-registration" where the "ideal" orifice meter discharge coefficient were assumed to apply to an orifice-type meter in one of the "non-ideal" installations. The shifts observed in these conditions are larger in magnitude for the larger beta values tested. Although the results of our measurement program are not capable of specifying the detailed quantitative effects of these secondary flows on these specific types of meters, it is apparent that these effects can significantly perturb meter performance but it is also apparent that our prediction scheme can successfully produce, to within the uncertainties shown, both the direction and magnitude of the shifts when these meters are installed in piping downstream of the single elbow.

d. Effects of Different Pressure Tap Orientations. The effects of different

pressure tap orientations was tested. Figure 33 presents results in normalized form. The ordinate scale is that for the mean orifice discharge coefficients taken over certain flowrates as done previously and normalized by the respective values for the ideal installation in each case. The ranges of Reynolds numbers selected are 14,000-45,000, 30,000-90,000, and 40,000-100,000 for beta ratios of 0.363, 0.500, and 0.750 respectively. Three pressure tap orientations were tested: (a) at the top of the pipe - these are referred to as "0 deg.", (b) at the right side of the pipe, looking upstream - these are referred to as "90 deg.", and (c) at the bottom of the pipe - these are referred to as "180 deg.". The results shown in figure 33 do not conclusively indicate a trend regarding tap position. The figure clearly indicates the previously noted trends regarding the beta ratio of the orifice plate; it is noted that the single elbow effects reduce discharge coefficients from the "ideal" installation values.

Figure 34 shows the shifts in discharge coefficient that are obtained when the results from the different tap orientations are averaged. These results also show the monotonic nature of the discharge coefficient change with beta ratio and the respective quantitative differences.

DESCRIPTIONS OF SECONDARY FLOW FROM A SINGLE ELBOW

The measurements made of the secondary flow from the single elbow and the results presented in figures 1-6 now enable a description of the vorticity distributions in this flow field. The vertical components of the mean velocity profile along the X axis that are shown in figures 3(a) and 4(a) clearly indicate the presence of two secondary vortices located on either side of the pipe centerline. The centers of rotation of these vortices probably do not lie on the horizontal diameter; they probably lie above this diameter and their precise locations probably depend on such parameters as Reynolds and Dean numbers, etc. Dean number is $(Re/2)(D/2r)^{1/2}$, where, in compatible units, Re is the diametral Reynolds number, D is the inside pipe diameter, and r is the radius of curvature of the centerline of the pipe elbow. When $Re = 10^5$, our Dean number is 28,900. The Dean number is a measure of the centrifugal effects produced by the elbow. These secondary vortices can be considered to have their vorticity vectors essentially parallel to the Z axis. In accordance with right-hand rule convention, the vortex lying on the negative X axis can - with its clockwise (looking upstream) direction of rotation - be considered as $-S_z$ and that lying on the positive X axis as $+S_z$, see figure 35(a). As the fluid flows through this single elbow, the distribution of mean axial velocity along the vertical diameter, see figures 1(b) and 2(b) indicates that the flow exiting this elbow also has a net vorticity component $-S_x$ see figure 35(b). In figure 35(c) the circles are intended to show this $-S_x$ vorticity, using a sequence of these circles in solid and dashed lines positioned along the flow direction through the elbow and into the downstream piping: the initial generation of this vorticity, its growth as shown by the darkness of the lines, and its decay in the downstream piping. These sketches are not drawn to scale.

These vorticity vectors must, of course, conform to the vorticity transport relationships. As the results of these, one can begin to understand both the qualitative and the quantitative characteristics of the pipeflows exiting

multiple elbow configurations. For example, in the case of two elbows-out-of-plane where the spacing between the elbows is small, the orientation of the second elbow with the vorticity vector dictates the rotational direction of the axial vorticity in this pipe flow. This is sketched in figure 36. In figure 36(a), the three letter piping configuration convention "L + X - Ys" indicates that the inlet pipe directs flow in the positive X direction; the "-Ys" indicates that long radius elbow turns this inlet flow into the negative Y direction and the second elbow turns the flow again through 90° into the positive Z direction. Thus, figure 36(a) shows the elbow orientations to change the directions of the pipe flow, Q. Figure 36(b) indicates the vorticity components generated by both elbows. The letters, S_x, S_y, and S_z indicate the directions of the vorticity generated. The arrows indicate the sense of the vorticity in our coordinate system. Therefore, when the two elbows are closely spaced there are generated six vorticity vectors, the relative interactions of which dictate the nature of the secondary flow observed in the downstream piping. In figure 36(c) are sketched these six vorticity vectors. The survival of these vorticities greatly depends on the orientation of the vorticity vector with respect to the pipe line. The three in the Z direction are aligned to combine according to their relative magnitudes and locations in the pipe cross-section. These vortices will tend to survive in the downstream pipe because their axes of rotation tend to align with the pipe centerline. The remaining three vorticity vectors are all normal to the pipe line and because of this mis-alignment these vortices can be expected to decay rapidly.

It is concluded from the orientations of these two elbows in the arrangement shown in figure 36 that when the spacing, s, between the elbows is small, the vorticity component, S_z generated by the first elbow has not time to decay appreciably and therefore will be significant in determining the nature of the secondary flow produced in the piping downstream of the elbows-out-of-plane configuration. On the other hand, when the spacing, s, between the two elbows is large, the S_z vorticity has already decayed, then the axial vorticity in the downstream piping could be dominated by the dual eddy distributions produced by the second of the two elbows. This, in fact, has been observed, [1].

With the resulting understanding of the vorticity features generated by pipe elbows, it is now feasible to speculate on the secondary flow characteristics found in the downstream piping from other, untested, double elbow configurations. Figure 37 sketches two of these. In figure 37(a) is shown a sketch of the two-elbow-in-plane configuration where inlet and outlet flows are in the same sense in the Z direction. As shown, the six (6) components of the vorticity in the downstream piping should be oriented so that there are two components in each of the three coordinate directions. In each of the three directions, the pairs of vectors have opposite senses and thus the interpretation could be that, depending upon conditions, these might cancel each other and the resulting secondary flow might not be significant.

Figure 37(b) shows a sketch of the two elbows in plane where the configuration reverses the direction of the inlet flow. The six components of vorticity again are arranged so that there are two in each of the three coordinate directions. In the Y and Z directions, the vorticity senses have opposite

directions and so, depending on conditions, canceling is feasible. However, in the X direction both components have the same sense and thus, depending upon conditions, the flow in the downstream piping should show the effects of these two components of vorticity reinforcing each other. When the spacer length between these two elbows is short, the influence of the X component of the vorticity should be strong. The effects that this should have on the axial component of the mean flow velocity would be that its profile along the vertical diameter could be skewed even more than that shown in figures 1(b) and 2(b). Because of this, the decay of these effects with downstream distance could be expected to be reduced in comparison to that of the single elbow.

CONCLUSIONS

The secondary pipe flows produced by a conventional, single, long-radius elbow configuration have been surveyed for two diametral Reynolds numbers, 10^4 and 10^5. This secondary flow pattern is found to be a dual-eddy one which decays, for these conditions, within 20-30 diameters downstream of the exit plane of the elbow. Additionally, there is found another vorticity component oriented perpendicular to the axis of the downstream pipe and perpendicular to the plane of the elbow.

A range of parameters were defined to describe these secondary flows. Using the measured data, these parameters were computed, plotted, and analysed for a succession of axial positions in the piping downstream of the elbow.

Two different types of flowmeters were selected - a turbine-type and an orifice-type to demonstrate the level of success that can be attained when our strategy is applied to predict the shifted meter factor or discharge coefficient pertinent to these flowmeters being installed in a "non-ideal" location downstream of a single elbow. Three different orifice plates were tested. It was found that these two types of meters had significant shifts when installed within 20-30 pipe diameters downstream of the elbow.

Correlation of the shifts of these meters and the parameters produced for the disturbed flows in the pipe downstream of this elbow indicated that a pipe swirl parameter was the most successful of those tried for predicting the performance of these meters in these flows.

Using this pipe swirl parameter, it was found that very accurate metering could be predicted for these types of meters in these flows using the strategy put forth in this flowmeter installation effects research program.

REFERENCES

1. Mattingly, G.E. and Yeh, T.T. NIST's Industry-Government Consortium Research Program on Flowmeter Installation Effects: Report of Results for the Research Period June - December 1987. NISTIR-88-3898. Sept. 1988.

2. Mattingly, G.E., Yeh, T.T., and Robertson, B., Flowmeter Installation-Effects: A New Approach to an Old but Prevalent Problem. Procs. Int'l Symp. on Flow Measm't in the 1980's, NEL UK East Kilbride, Scotland U.K., June 1986.

3. Mattingly, G.E., Yeh, T.T., Robertson, B. and Kothari, K., NBS Research on In-Situ Flowmeter Installations, Procs. AGA Distribution and Transmission Confr. Las Vegas NV, May 1987.

4. Mottram, R.C. and Hutton, S.P., Installation Effects: Turbine and Vortex Flowmeters, Rept. No. 3 Flow Measurement and Instrumentation Consortium, Cranfield Inst. of Tech., Bedfordshire, U.K. Dec. 1987.

5. Yeh, T.T. and Mattingly, G.E. Mixing Motions Produced by Pipe Elbows, Procs. AIChE Winter Annual Meeting. Wash. D.C., Dec. 1988.

6. McManus, S.E., Bateman, B.R., Brennan, J.A., Pantoja, I.V. and Mann, D.B. The Decay of Swirling Gas Flow in Long Pipes, Procs., AGA Distribution and Transmission Conf. Boston, MA. May, 1985.

7. Mottram, R.C. and Rawat, M.S., Attenuation Effects of Pipe Roughness on Swirl and The Implications for Flowmeter Installation. International Symposium on Fluid Flow Measurement, American Gas Association (1986).

8. Laufer, J., The Structure of Turbulence in Fully Developed Pipe Flow, NBS Rept 1974, 1Sept 1952. Alternatively see Hinze, J.O., Turbulence, McGraw-Hill, New York (1959) (Laufer's data in chapter 7).

9. ASME Standard MFC-1M Glossary of Terms, published by the American Society of Mechanical Engineers, New York, NY.

10. Schlichting, H. Boundary Layer Theory, McGraw-Hill Book Co., New York.

11. Dryden, H., Murnaighan, F.D, and Bateman, H., Hydrodynamics, Dover Publ. Co., New York, NY 1956.

APPENDIX 1

NIST INDUSTRY-GOVERNMENT CONSORTIUM MEMBERSHIP

As of the 1989 research period, the NIST Industry-Government Consortium Research Program on Flowmeter Installation Effects included the following members, in alphabetical order:

1. Ametek-McCrometer
2. Chevron Oil
3. Dow Chemical Co.
4. E.I. DuPont de Nemours
5. Ford Motor Co.
6. Gas Research Institute
7. Gas Unie (The Netherlands)
8. Instrument Testing Service
9. ITT Barton
10. Kimmon Mfg. Ltd. (Japan)
11. NIST-Boulder
12. Rockwell International
13. Rosemount

APPENDIX 2

VORTEX MODELING

The vertical mean flow velocity measurements made along the horizontal diameter enable a sequence of vortex models to be tested to determine the relative success of applying these models to the secondary vorticies present in the pipe flow downstream of our single elbow. Three such models that were tested were:

1. Euler Vortex:

$$V = G/2\pi r$$

where, in compatible units:
V is the azimuthal velocity
r is the radial distance from center of the vortex
G is the circulation of the vortex.

2. Hamel-Oseen Vortex:

$$V = G/2\pi r\ [1 - \exp(-cr^2)]$$

where c is a constant

3. G.I. Taylor Vortex:

$$V = Cr \exp(-1/2\ (r/r_o)^2)$$

where: C is another constant

r_o is a measure of the core size of the vortex and the radial position where the maximum velocity V occurs.

Of these three, the G.I. Taylor vortex appeared to produce the best agreement with our measurements. Figure A1 presents the vertical mean velocity as it distributes over the X axis for diametral Reynolds number of 10^5 when a G.I. Taylor vortex is positioned on either side of the pipe centerline at $\pm$ 0.25D from the centerline. The constant C is selected to conform to the velocity distribution shown in Figure 3(a) for Z = 1.5. The core size, r_o is taken to be 0.2. Figure A1 presents individual distributions of velocity, V1 and V2 as noted from symbols given in the legend of the figure. The sum of the two velocities is Va.

The distribution of Va across the horizontal diameter is noted to closely approximate that in figure 3(a) for Z = 1.5. The maximum and minimum values conform closely to counterparts in figure A1. Slight deviations are noted in figure A1 at the locations X = $\pm$ 0.15 where the Va distribution appears to change curvature in ways not noticed in figure 3(b).

Figure A2 presents distributions along the horizontal diameter for the swirl flux

$$Si = WV_i r_i$$

where S1 is the swirl flux due to the vortex positioned at X = 0.25; S2 is that for the vortex positioned at X = +0.25. The sum of these, as noted in the legend of figure A2, is the middle curve plotted using the asterisk symbol. This distribution is to be compared with that for Z = 1.5 on figure 11. It is noted that while the shapes of the two curves are qualitatively the same, there are quantitative differences near the wall of the pipe.

DECAY CONSTANTS

for Single Elbow Pipe Flows

Fun. = b * exp(-c Z)

	Re = 10^4		Re = 10^5		c = d Re^e	
	b	c	b	c	d	e
Sp	0.030	0.177	0.028	0.136	0.508	-0.114
Se	0.018	0.185	0.020	0.151	0.235	-0.039
Sm	0.018	0.187	0.022	0.157	0.214	-0.027
Sx	-0.039	0.237	-0.020	0.201	0.459	-0.072
Sa	12.80	0.202	15.92	0.187	0.275	-0.034
DW0	-0.471	0.124	-0.338	0.053	3.715	-0.369
DW1	0.251	0.119	0.191	0.069	1.053	-0.237
DW3	0.242	0.111	0.195	0.088	0.788	-0.213
DV0	-0.155	0.173	-0.285	0.191	0.116	+0.043
DV1	0.103	0.180	0.122	0.143	0.251	-0.049
DV3	0.092	0.181	0.155	0.202	0.117	+0.048

TABLE 1 DECAY CONSTANTS OF SECONDARY FLOW PARAMETERS FOR THE SINGLE ELBOW FOR $Re_D = 10^4$ and 10^5.

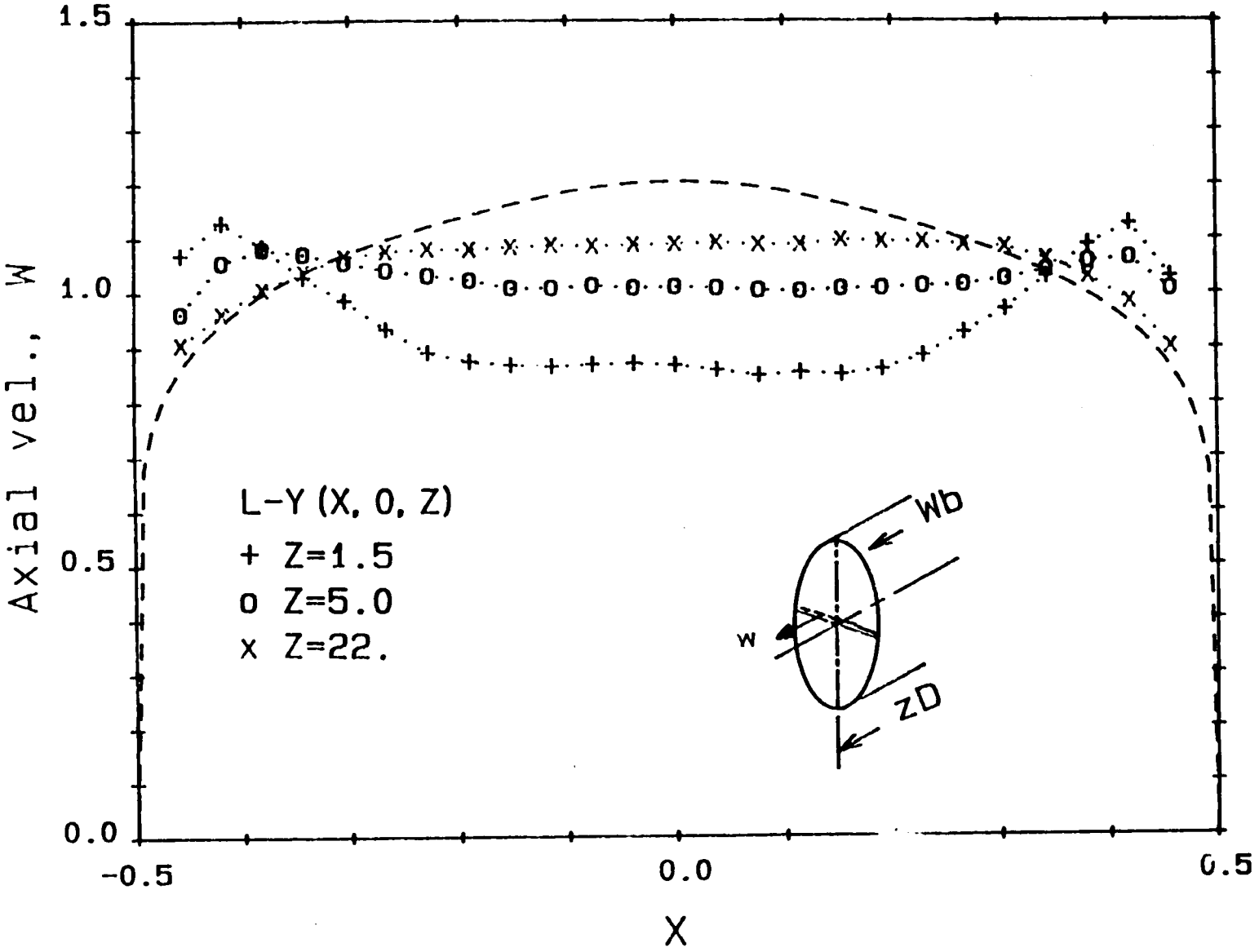

FIGURE 1 (a). Mean Axial Velocity Distributions Along the Horizontal Diameter for Different Axial Positions at $Re_D = 10^5$. The dashed line is the Power Law Distribution for n = 7.0.

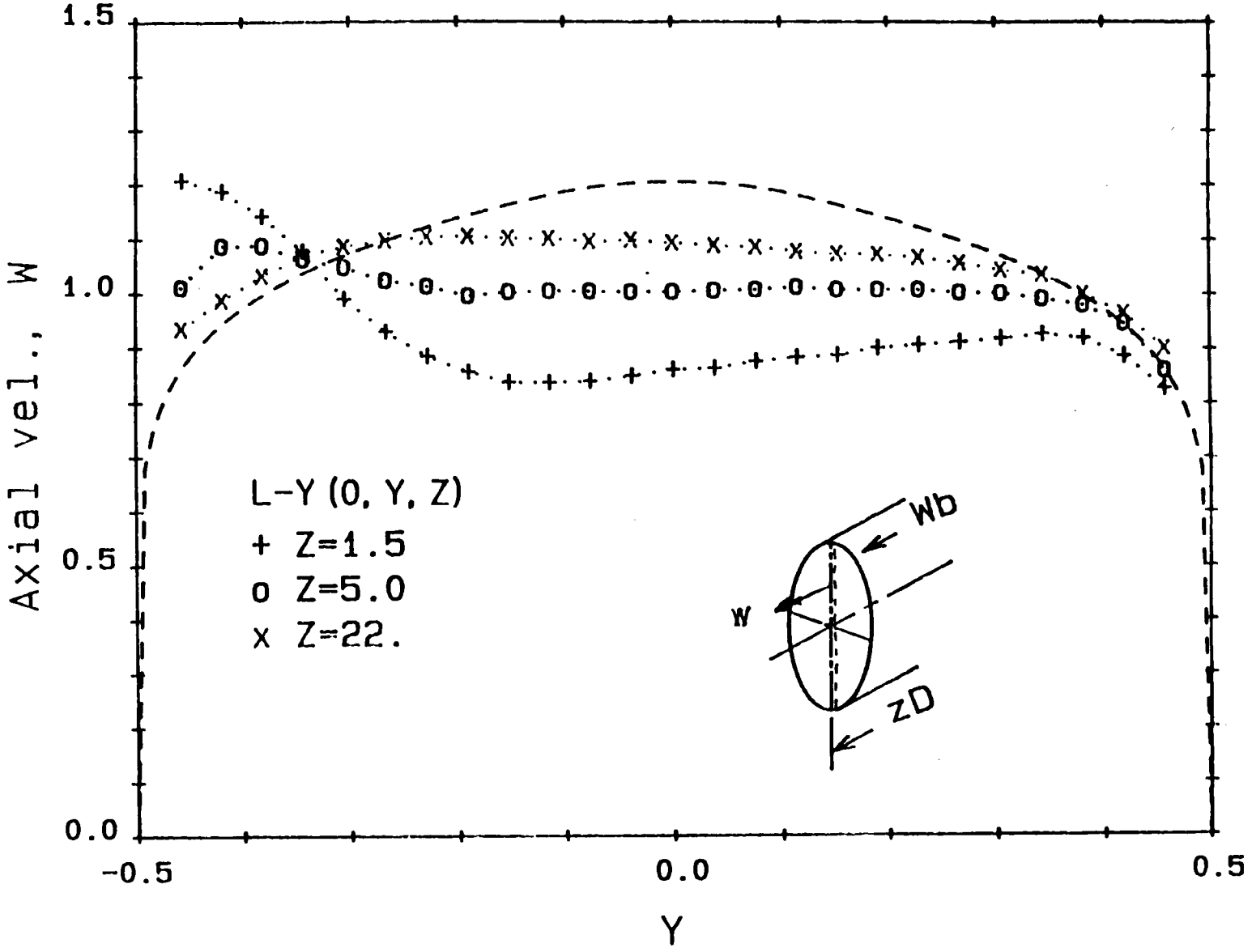

FIGURE 1 (b). Mean Axial Velocity Distributions Along the Vertical Diameter for Different Axial Positions at $Re_D = 10^5$. The dashed line is the Power Law Distribution for n = 7.0.

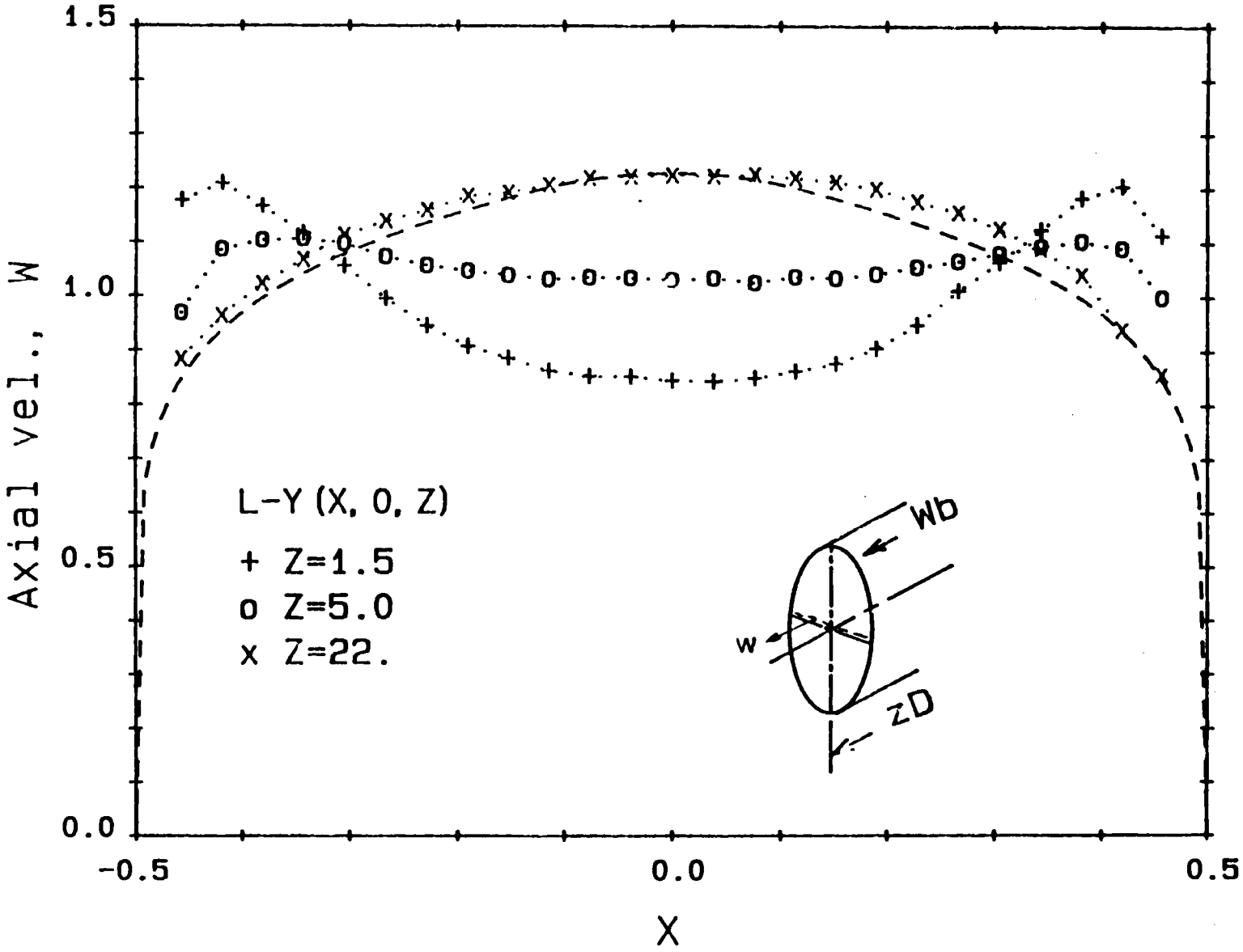

FIGURE 2 (a). Mean Axial Velocity Distributions Along the Horizontal Diameter for Different Axial Positions at $Re_D = 10^4$. The dashed line is the Power Law Distribution for n = 6.3.

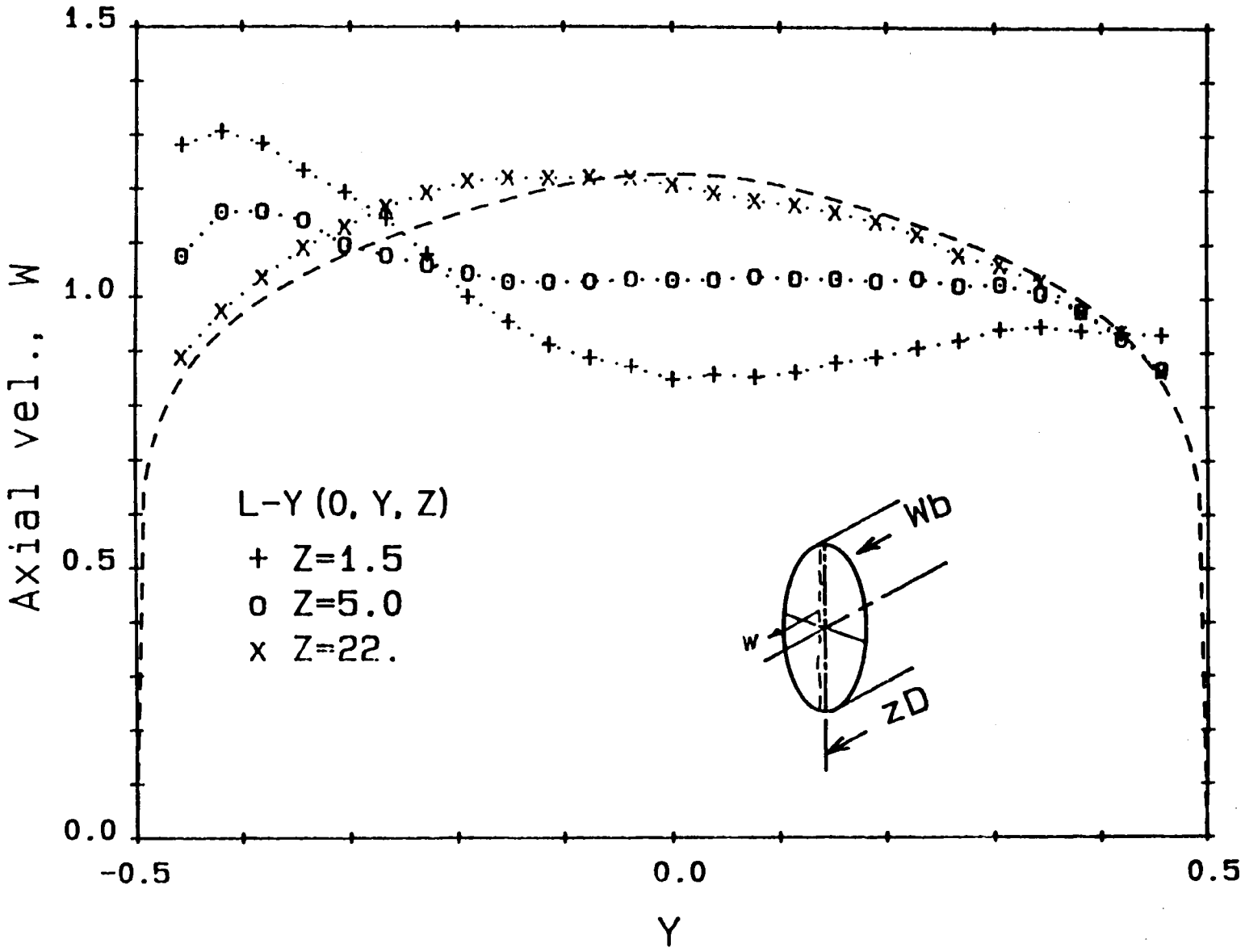

FIGURE 2 (b). Mean Axial Velocity Distribution Along the Vertical Diameter for Different Axial Positions at $Re_D = 10^4$. The dashed line is the Power Law Distribution for n = 6.3.

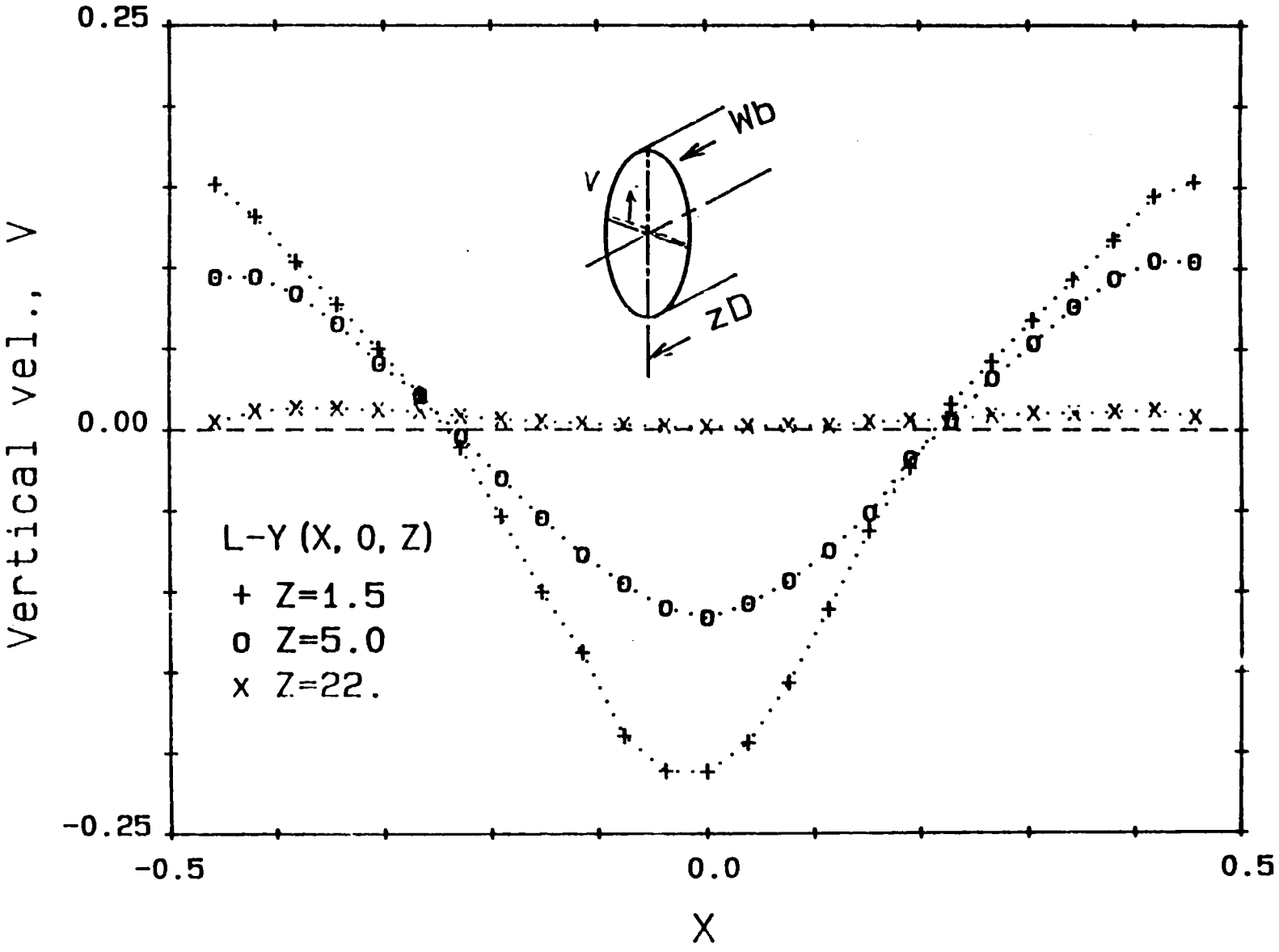

FIGURE 3 (a). Mean Vertical Velocity Distribution Along the Horizontal Diameter for Different Axial Positions at $Re_D = 10^5$.

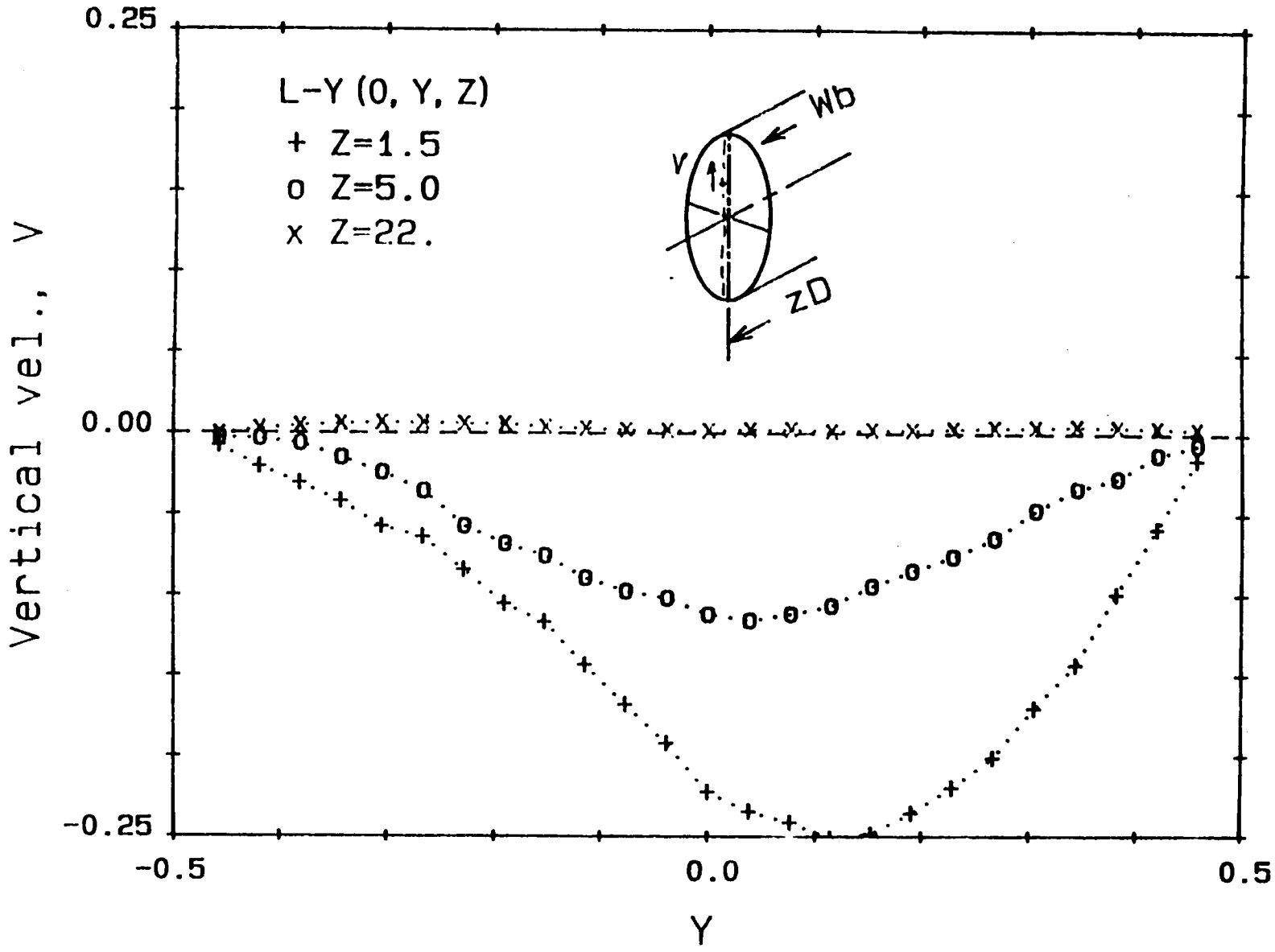

FIGURE 3 (b). Mean Vertical Velocity Distribution Along the Vertical Diameter for Different Axial Positions at $Re_D = 10^5$.

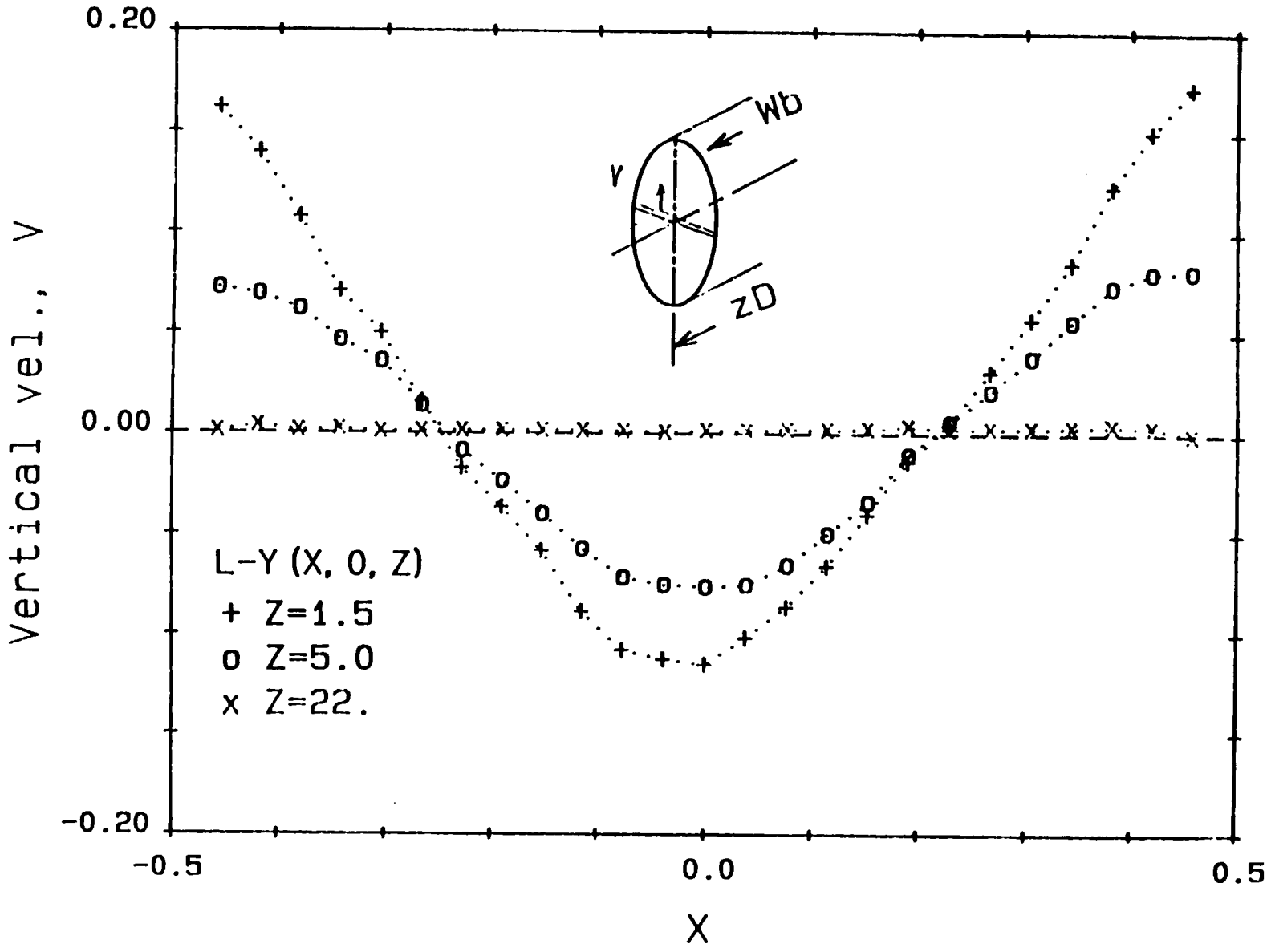

FIGURE 4 (a). Mean Vertical Velocity Distribution Along the Horizontal Diameter for Different Axial Positions at $Re_D = 10^4$.

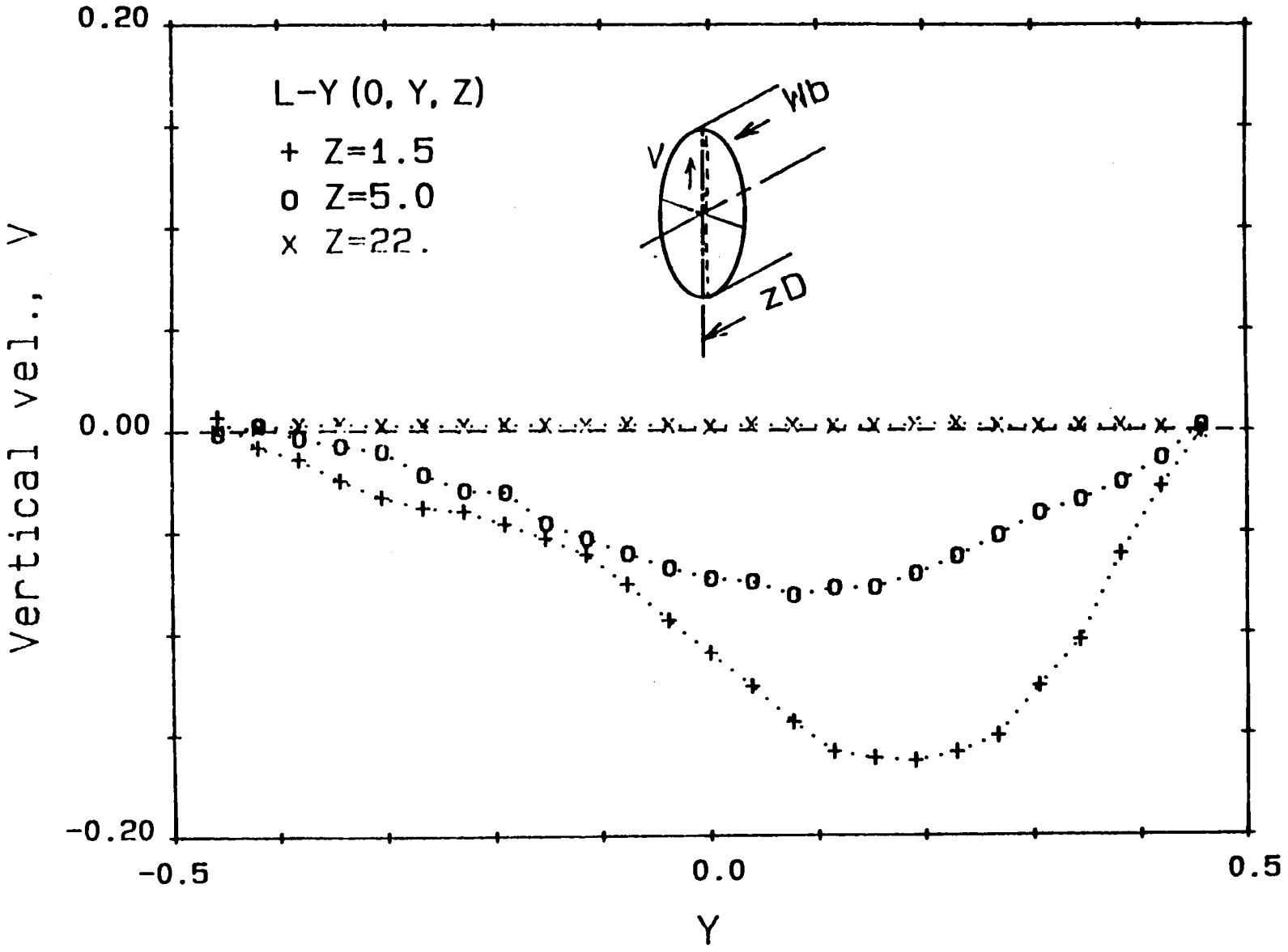

FIGURE 4 (b). Mean Vertical Velocity Distribution Along the Vertical Diameter for Different Axial Positions at $Re_D = 10^4$.

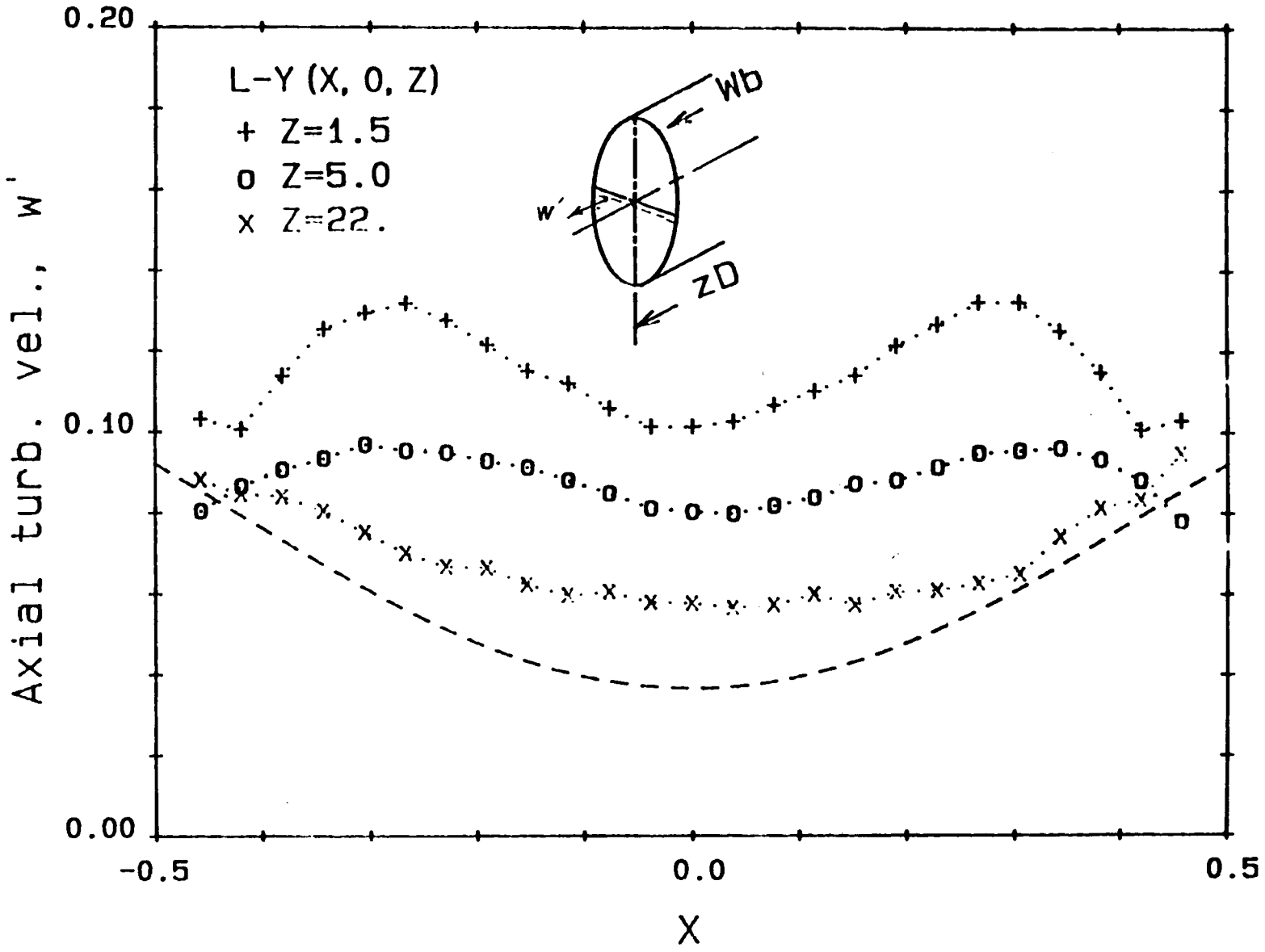

FIGURE 5 (a). Root-Mean-Square (r.m.s.) Distributions for the Axial Turbulence Along the Horizontal Diameter for Different Axial Positions at $Re_D = 10^5$. The dashed line is the Laufer data.

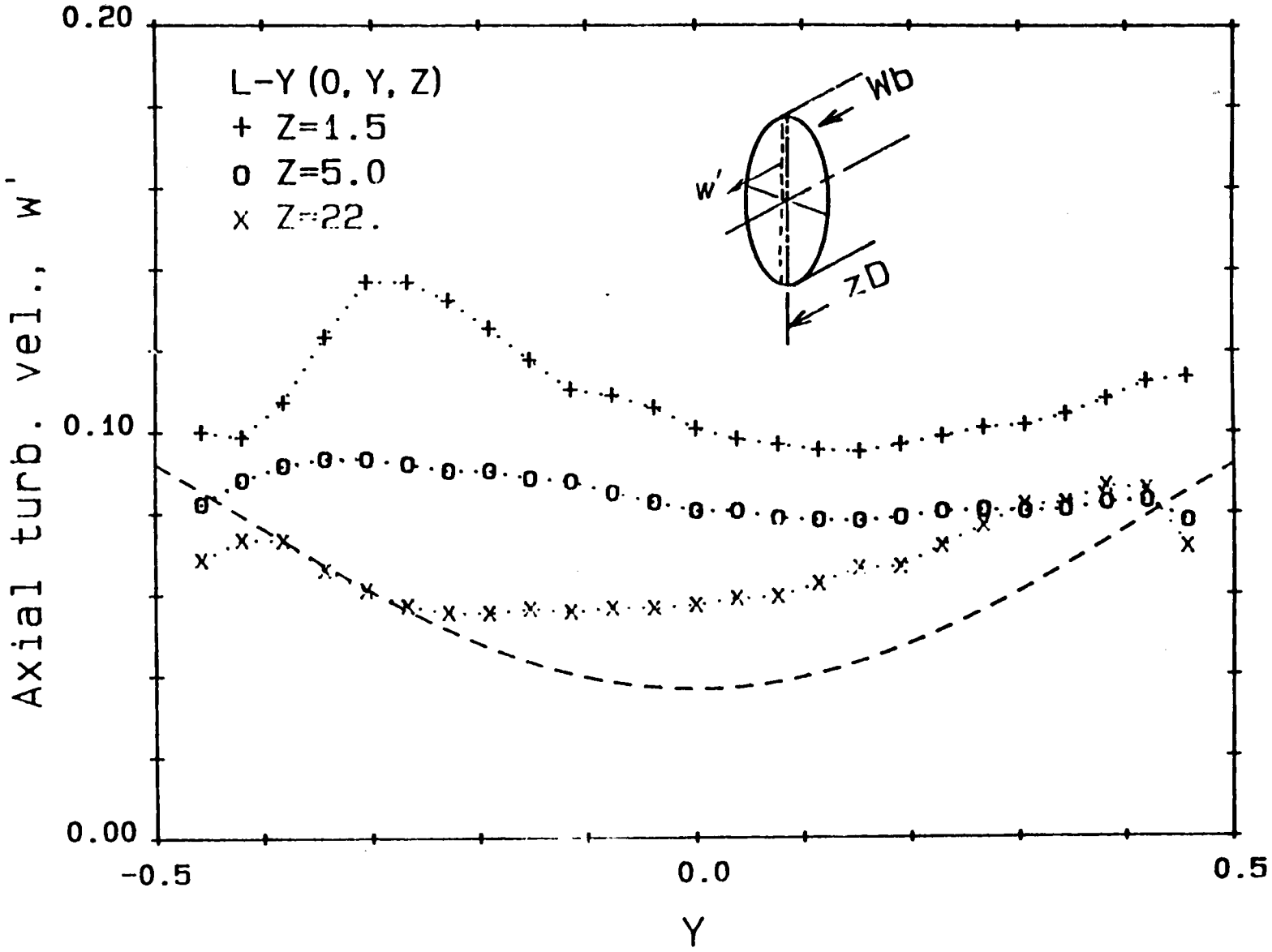

FIGURE 5 (b). Root-Mean-Square (r.m.s.) Distributions for the Axial Turbulence Along the Vertical Diameter for Different Axial Positions at $Re_D = 10^5$. The dashed line is the Laufer data.

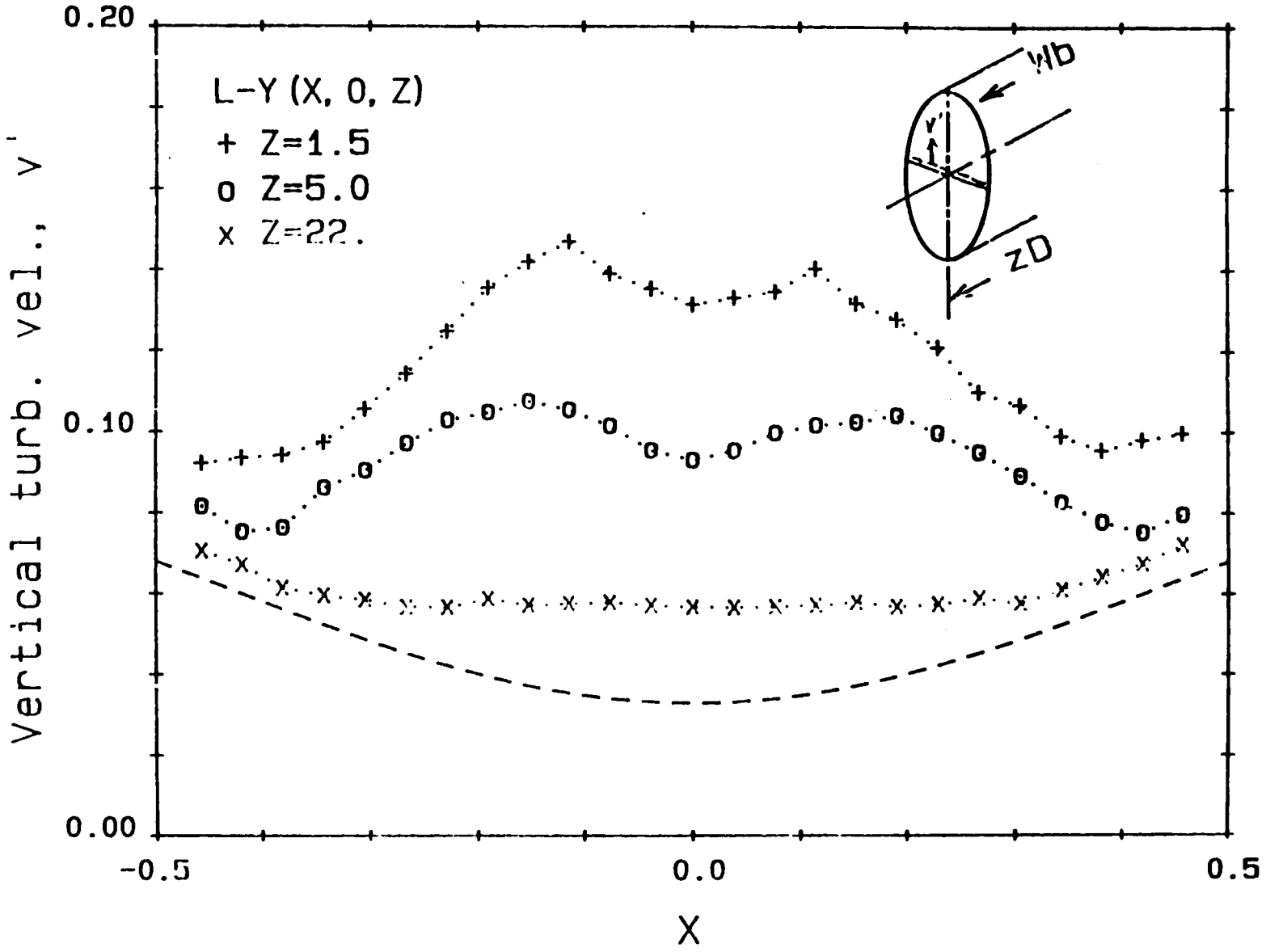

FIGURE 6 (a). Root-Mean-Square (r.m.s.) Distribution for the Vertical Component of the Turbulence Along the Horizontal Diameter for Different Axial Positions at $Re_D = 10^5$. The dashed line is the Laufer data.

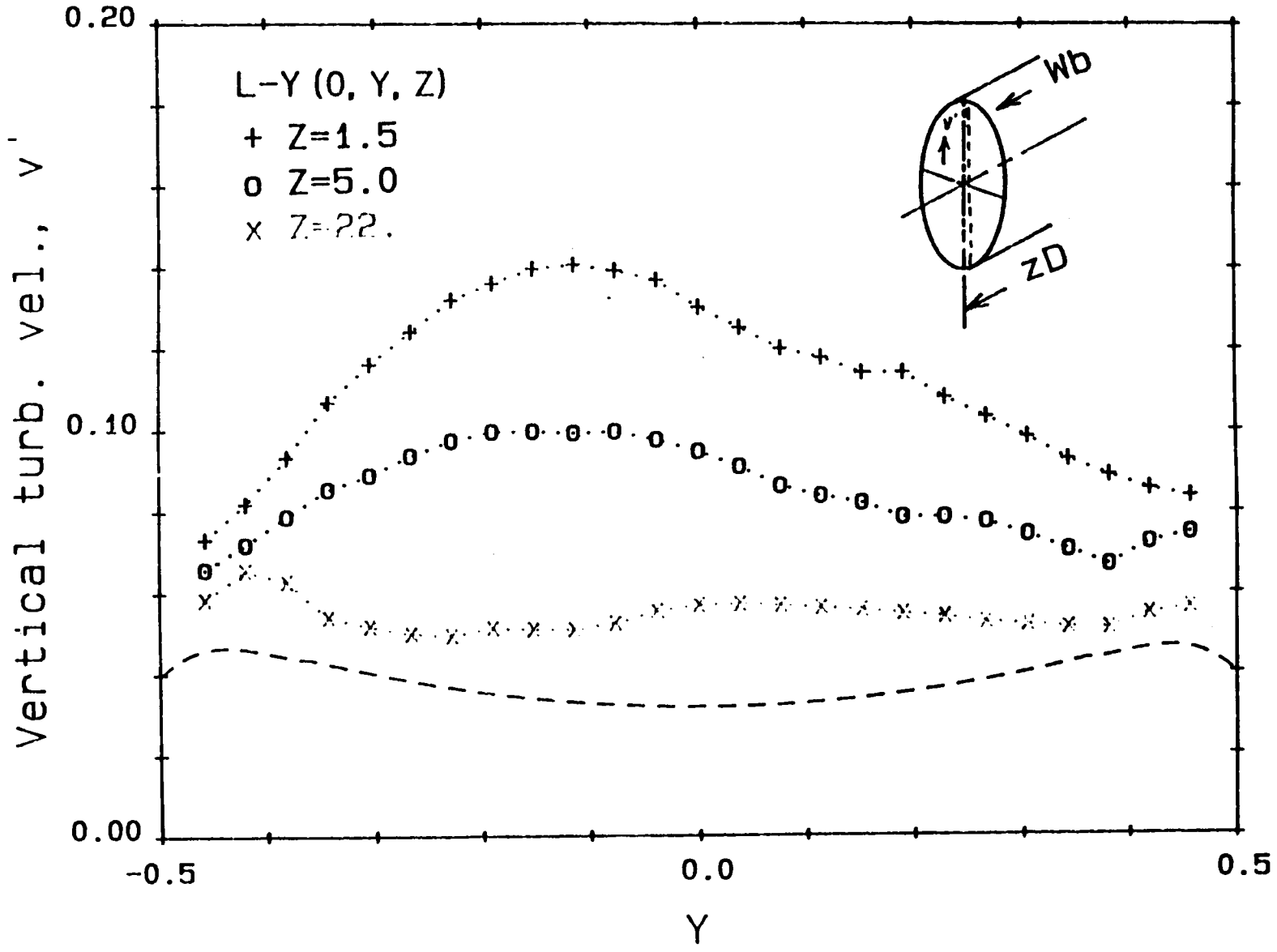

FIGURE 6 (b). Root-Mean-Square (r.m.s.) Distribution for the Vertical Component of the Turbulence Along the Vertical Diameter for Different Axial Positions at $Re_D = 10^5$. The dashed line is the Laufer data.

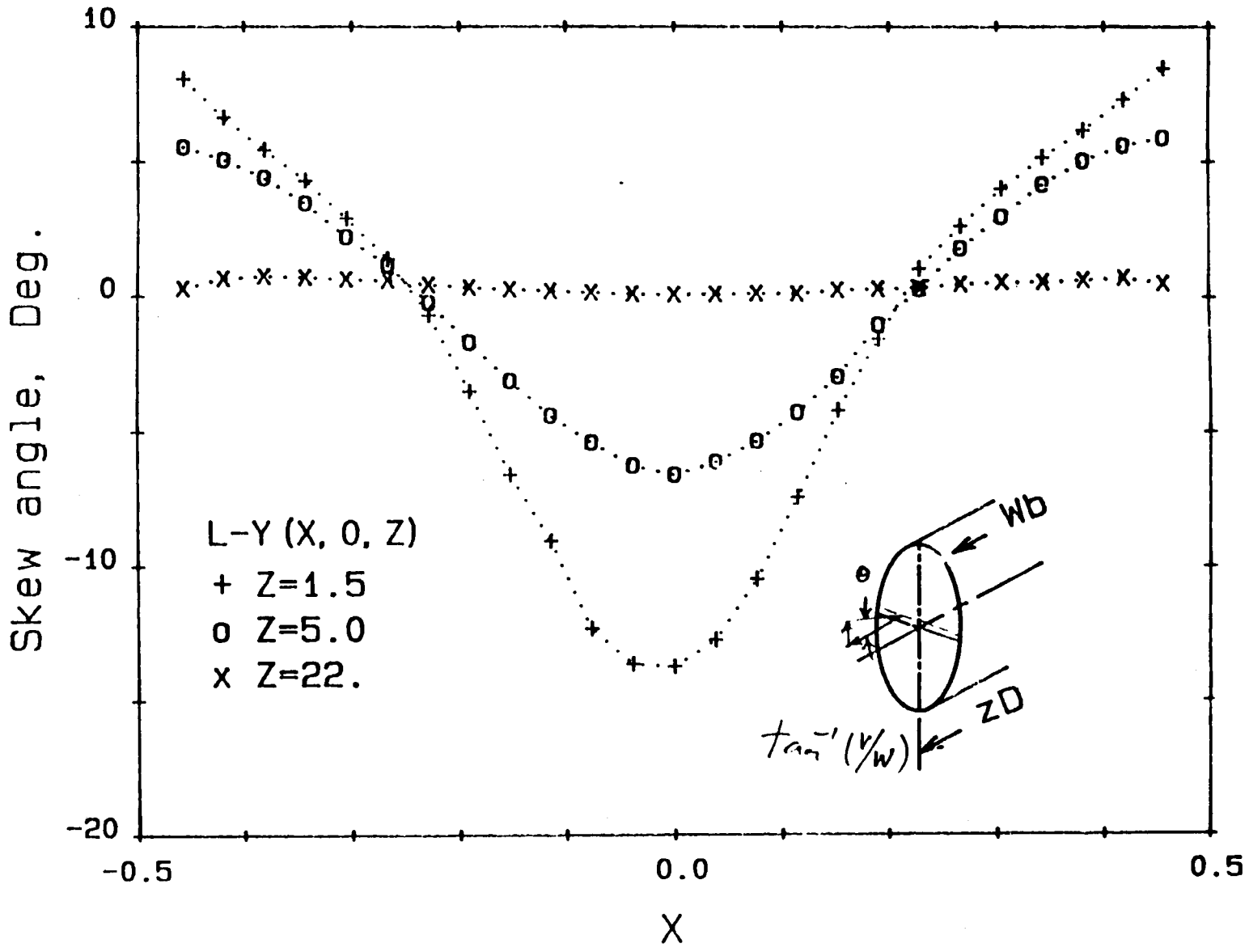

FIGURE 7 (a). Skew Angle Distribution Along the Horizontal Diameter for Different Axial Positions at $Re_D = 10^5$.

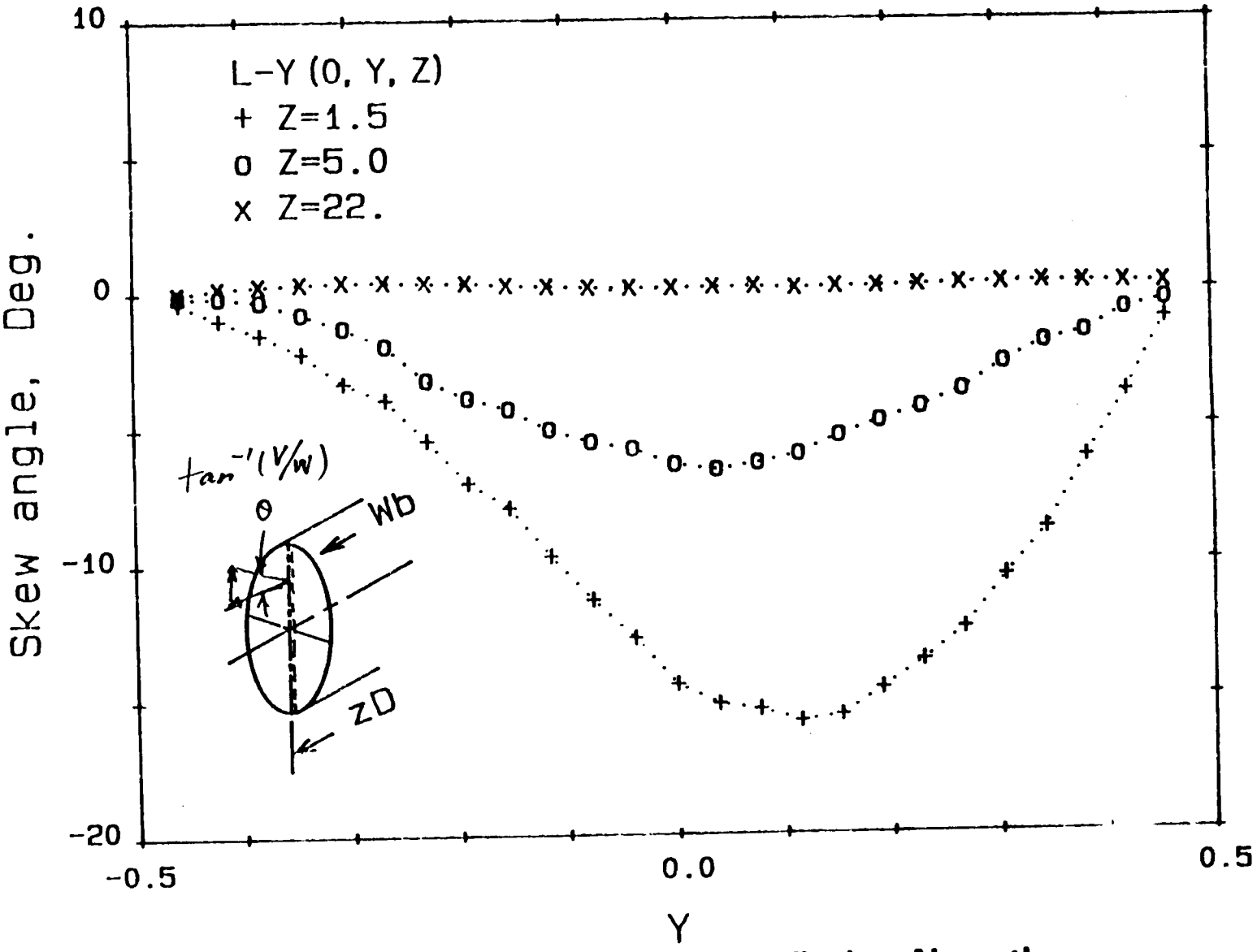

FIGURE 7 (b). Skew Angle Distribution Along the Vertical Diameter for Different Axial Positions at $Re_D = 10^5$.

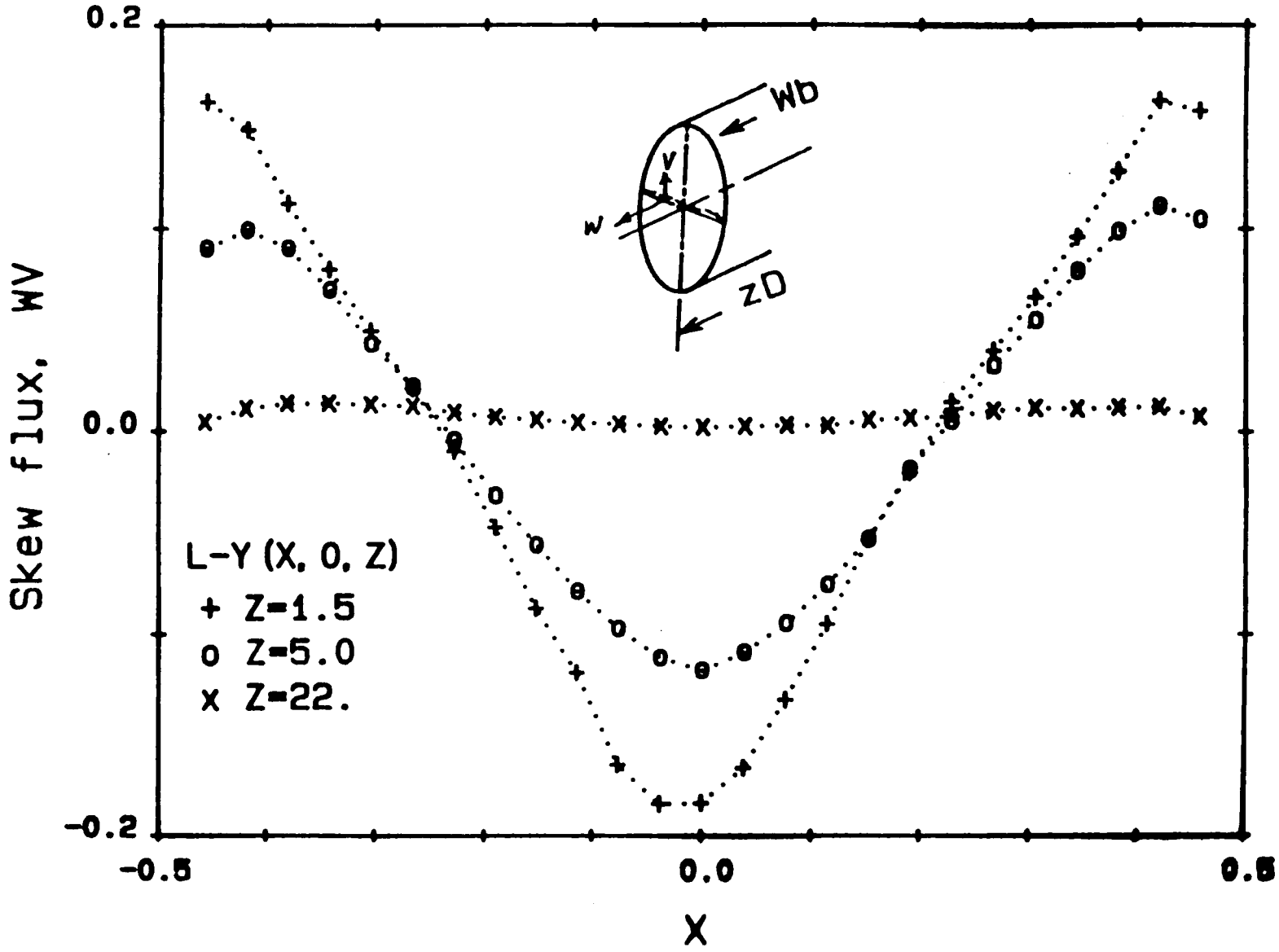

FIGURE 8 (a). Skew Flux Distribution Along the Horizontal Diameter for Different Axial Positions at $Re_D = 10^5$.

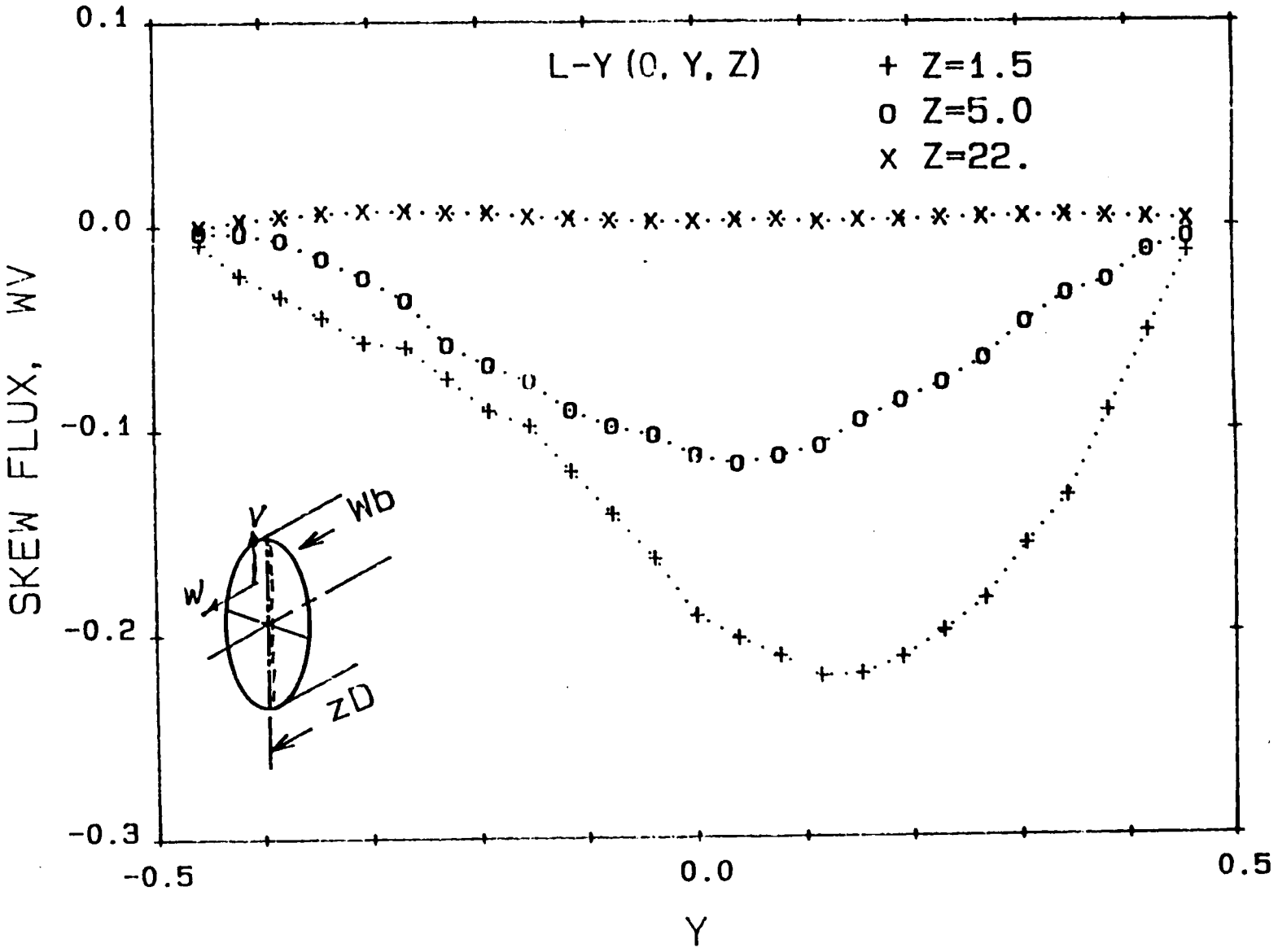

FIGURE 8 (b). Skew Flux Distribution Along the Vertical Diameter for Different Axial Positions at $Re_D = 10^5$.

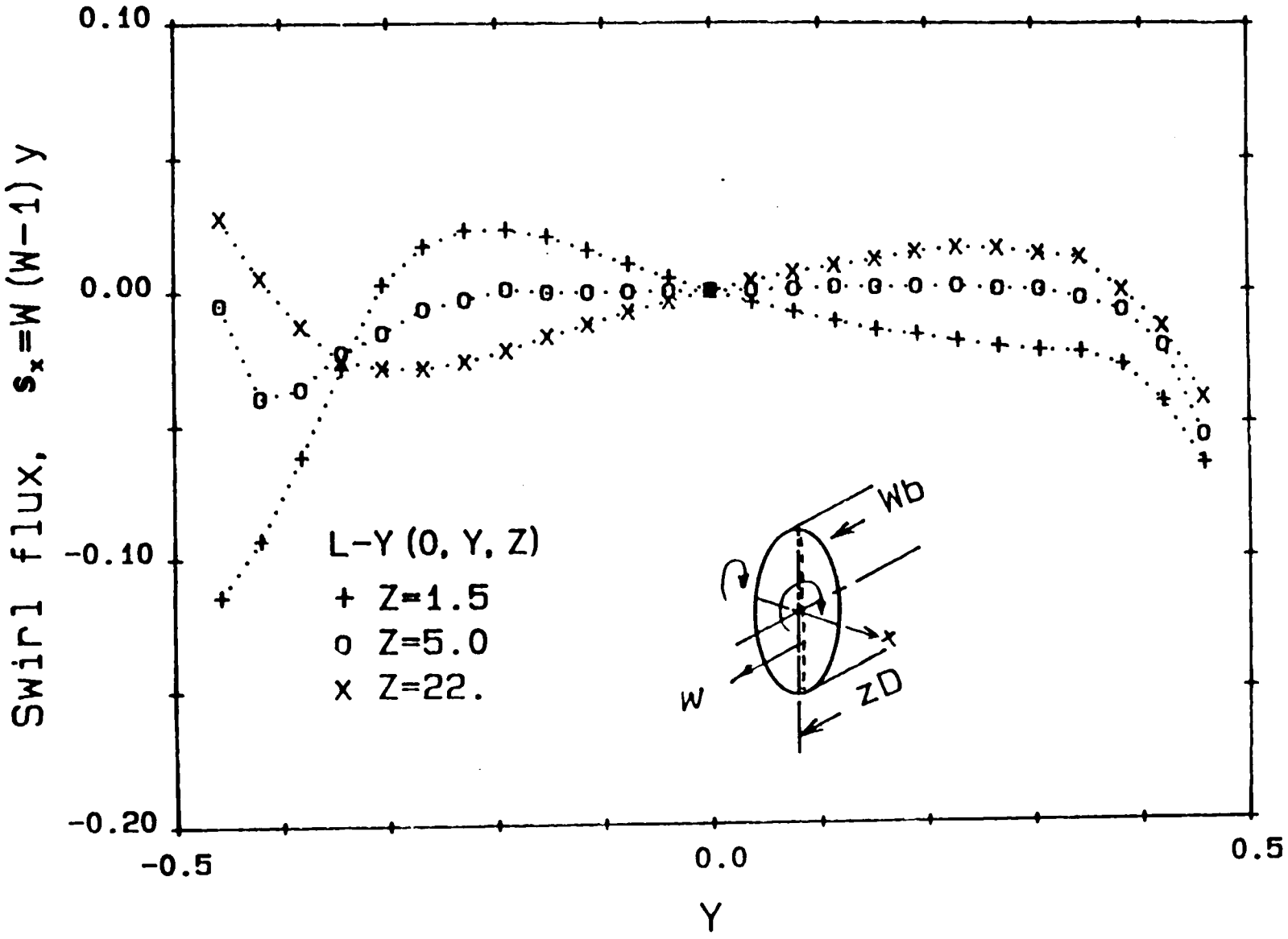

FIGURE 9. Swirl Flux s_x, Distribution Along the Vertical Diameter for Different Axial Positions at $Re_D = 10^5$.

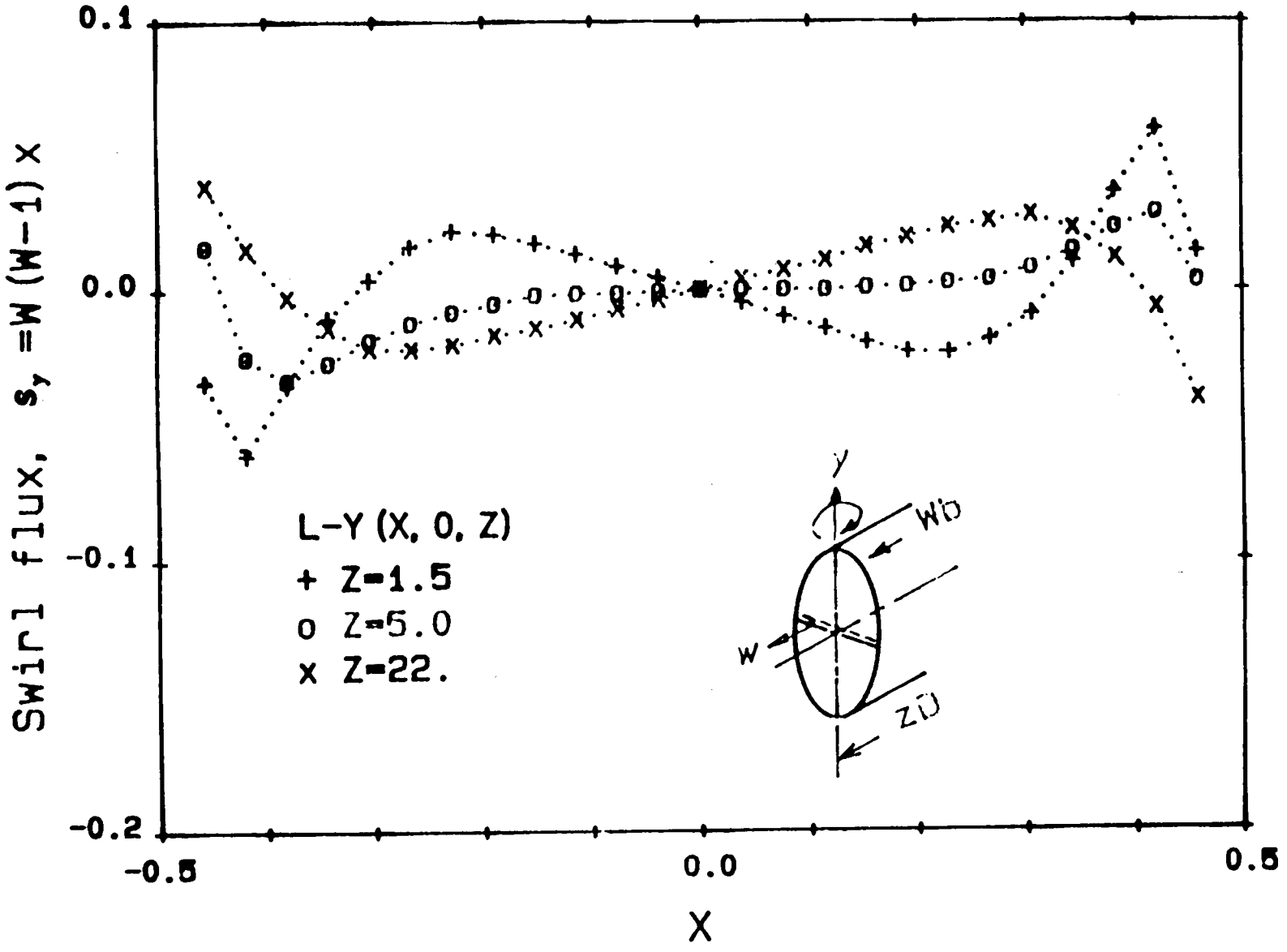

FIGURE 10. Swirl Flux, s_y Distribution Along the Horizontal Diameter for Different Axial Positions at $Re_D = 10^6$.

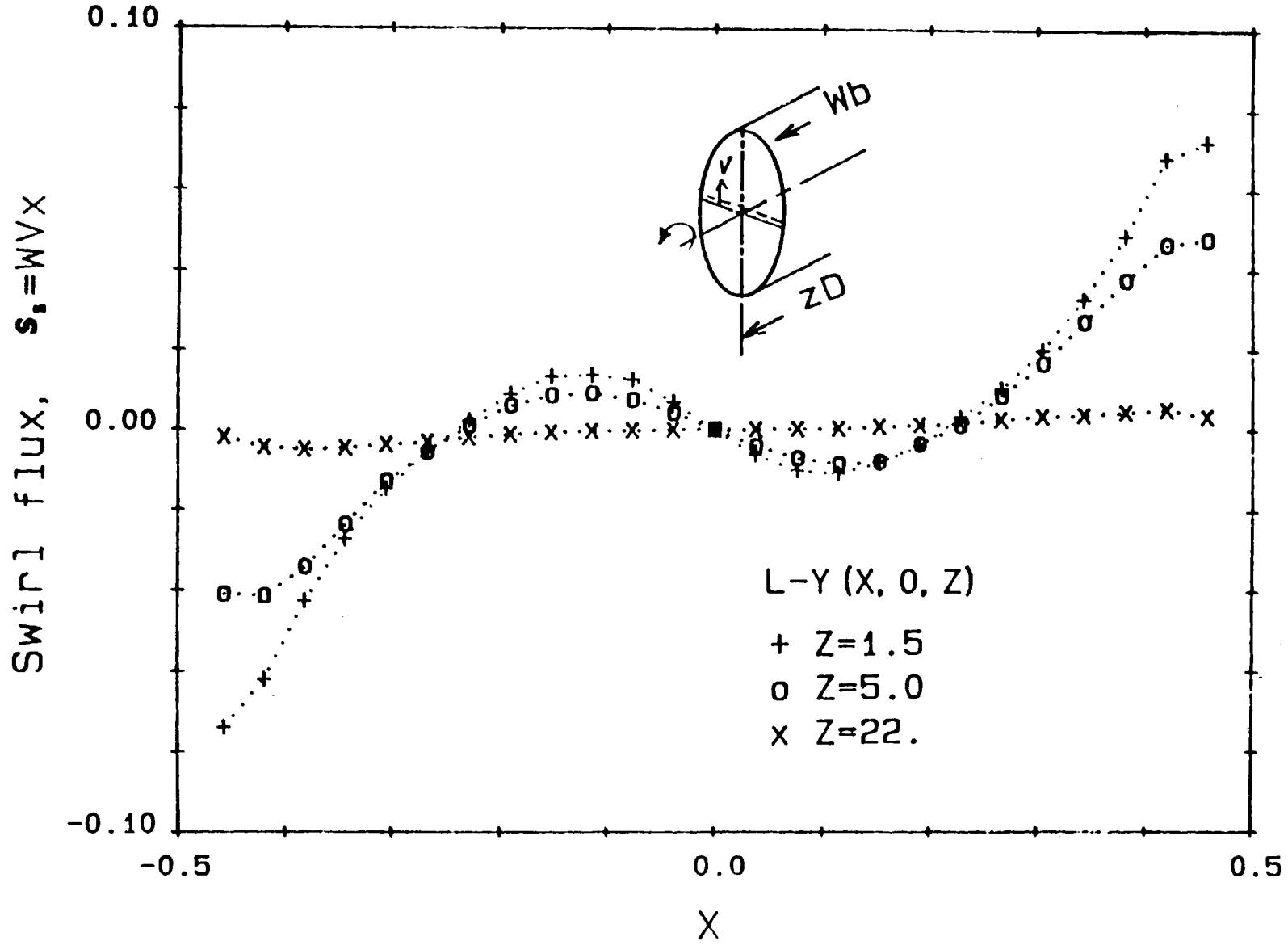

FIGURE 11. Swirl Flux, s_x, Distribution Along the Horizontal Diameter for Different Axial Positions at $Re_D = 10^5$.

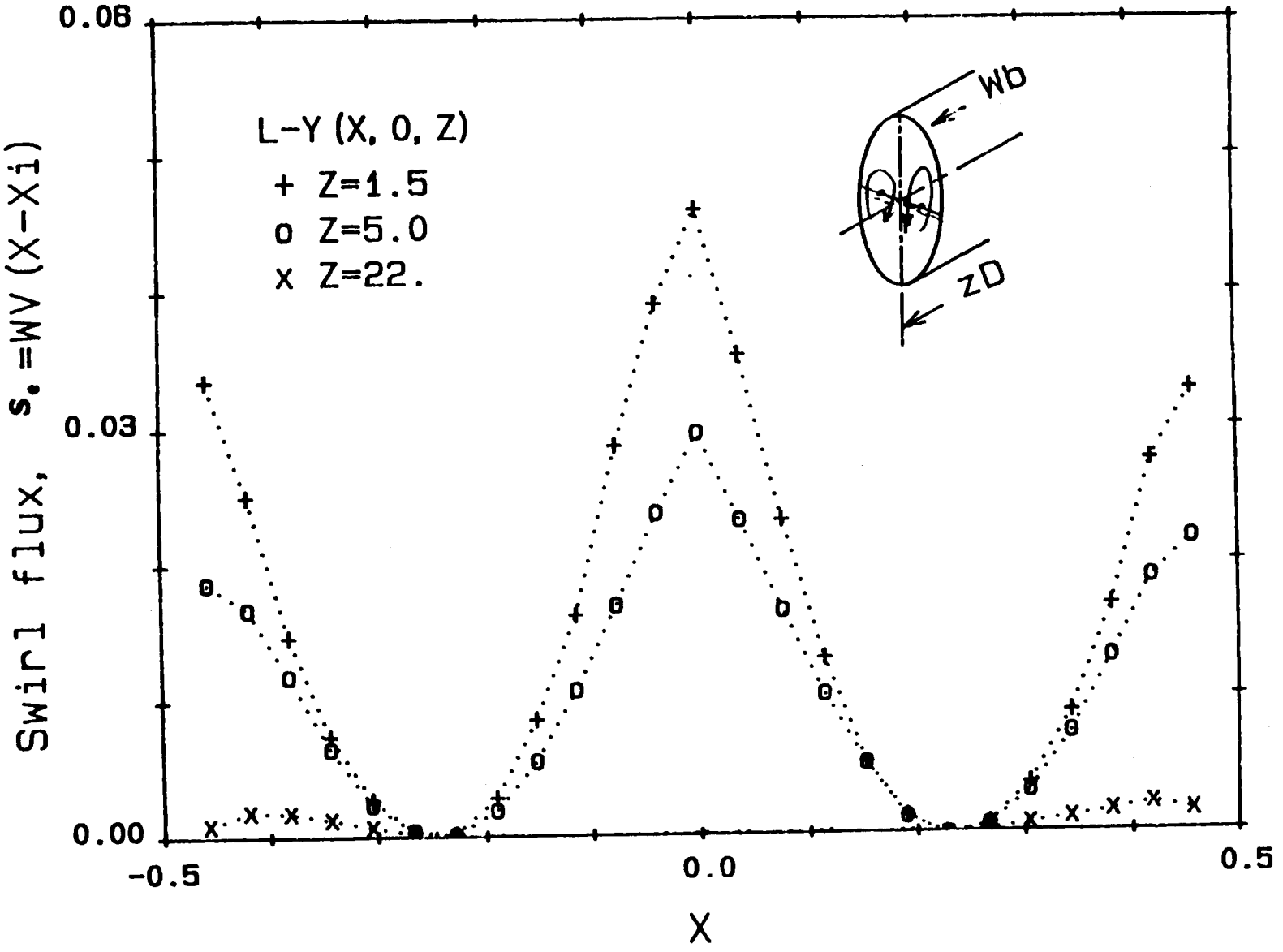

FIGURE 12. Swirl Flux, s_θ, Distribution Along the Horizontal Diameter for Different Axial Positions at $Re_D = 10^5$.

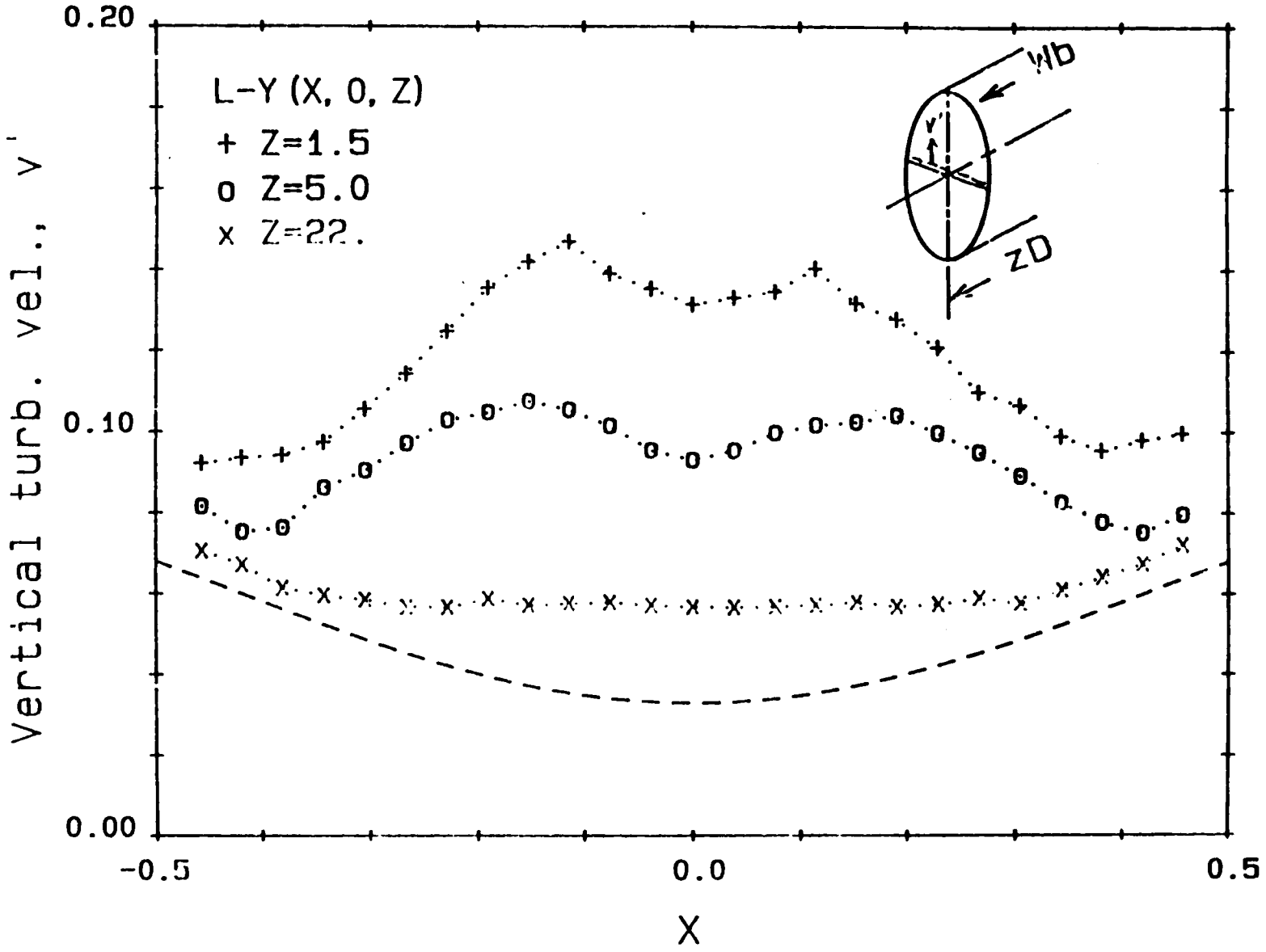

FIGURE 6 (a). Root-Mean-Square (r.m.s.) Distribution for the Vertical Component of the Turbulence Along the Horizontal Diameter for Different Axial Positions at $Re_D = 10^5$. The dashed line is the Laufer data.

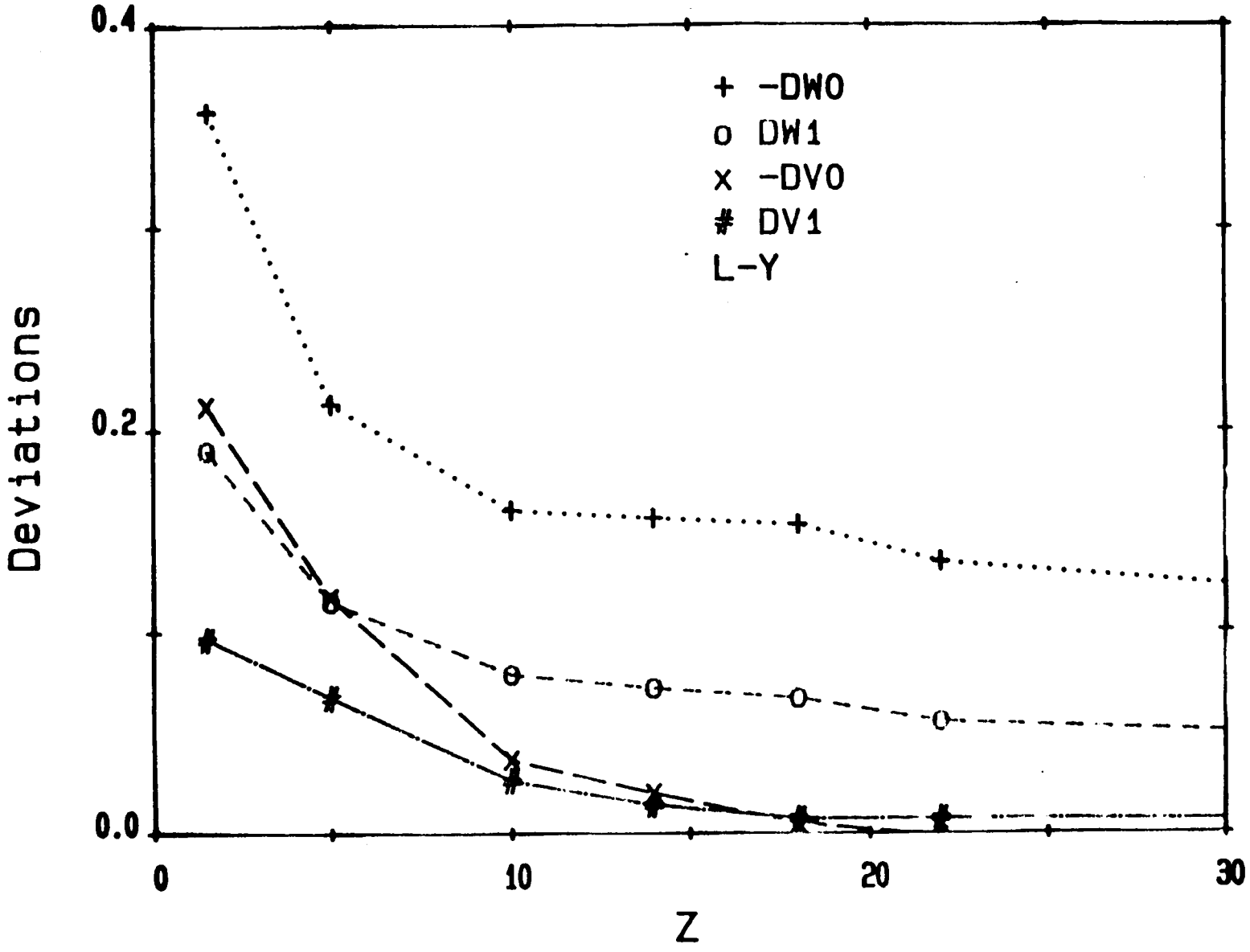

FIGURE 14. Axial Distribution of Deviations From Ideal Flows for $Re_D = 10^5$.

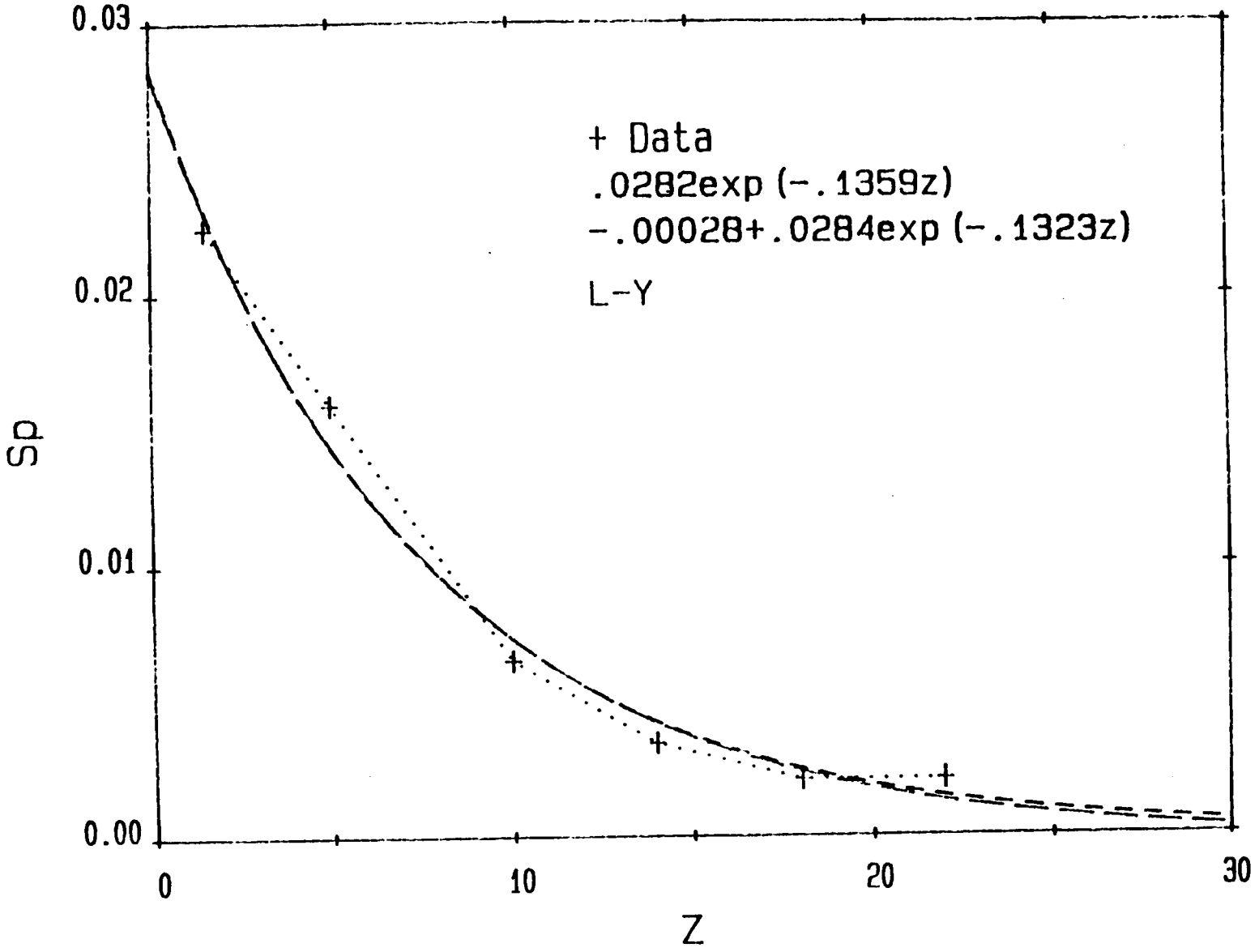

FIGURE 15. Axial Distribution of the Pipe Swirl Number, S_p, for $Re_D = 10^5$.

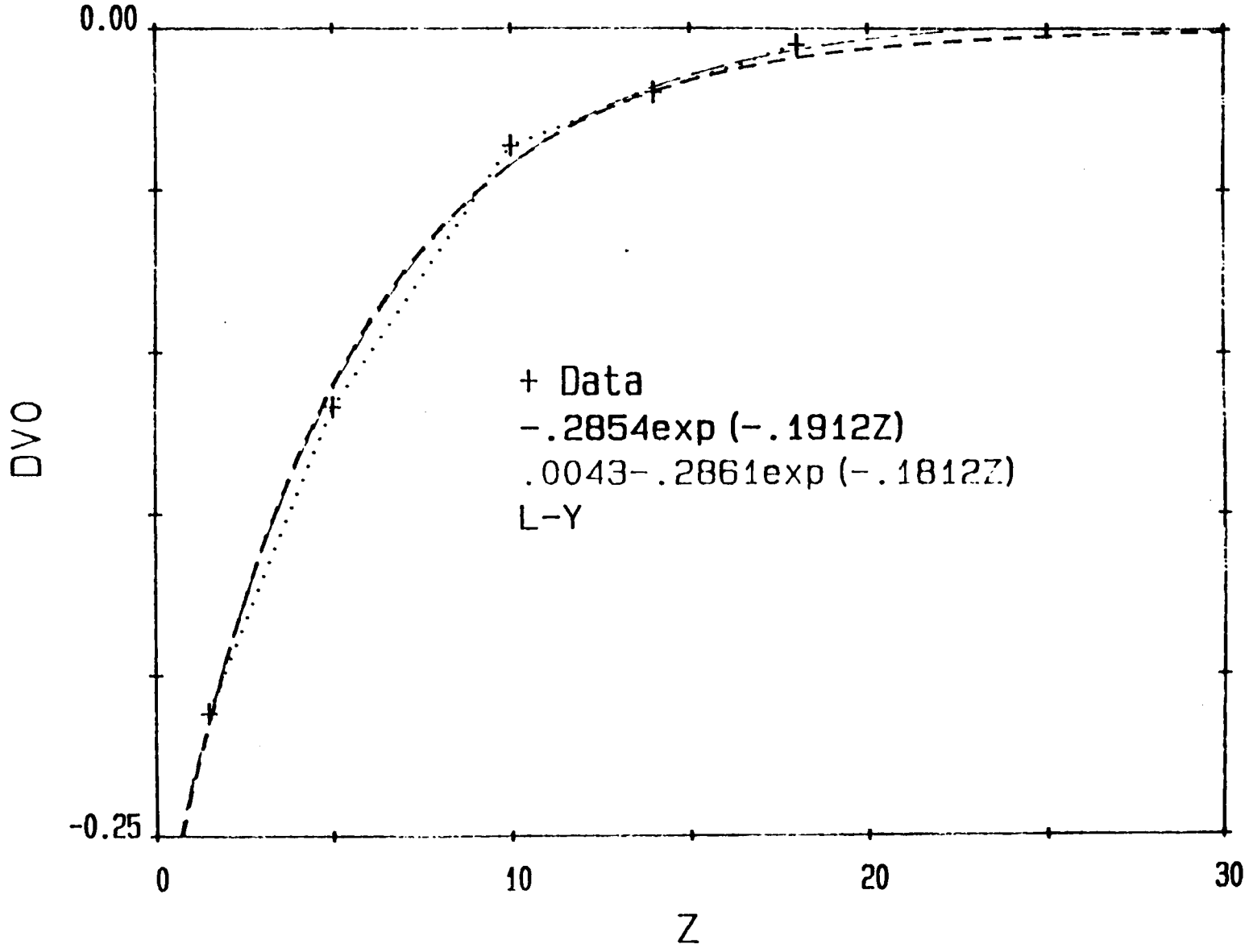

FIGURE 16. Axial Distribution of Deviation, DVO for $Re_D = 10^5$.

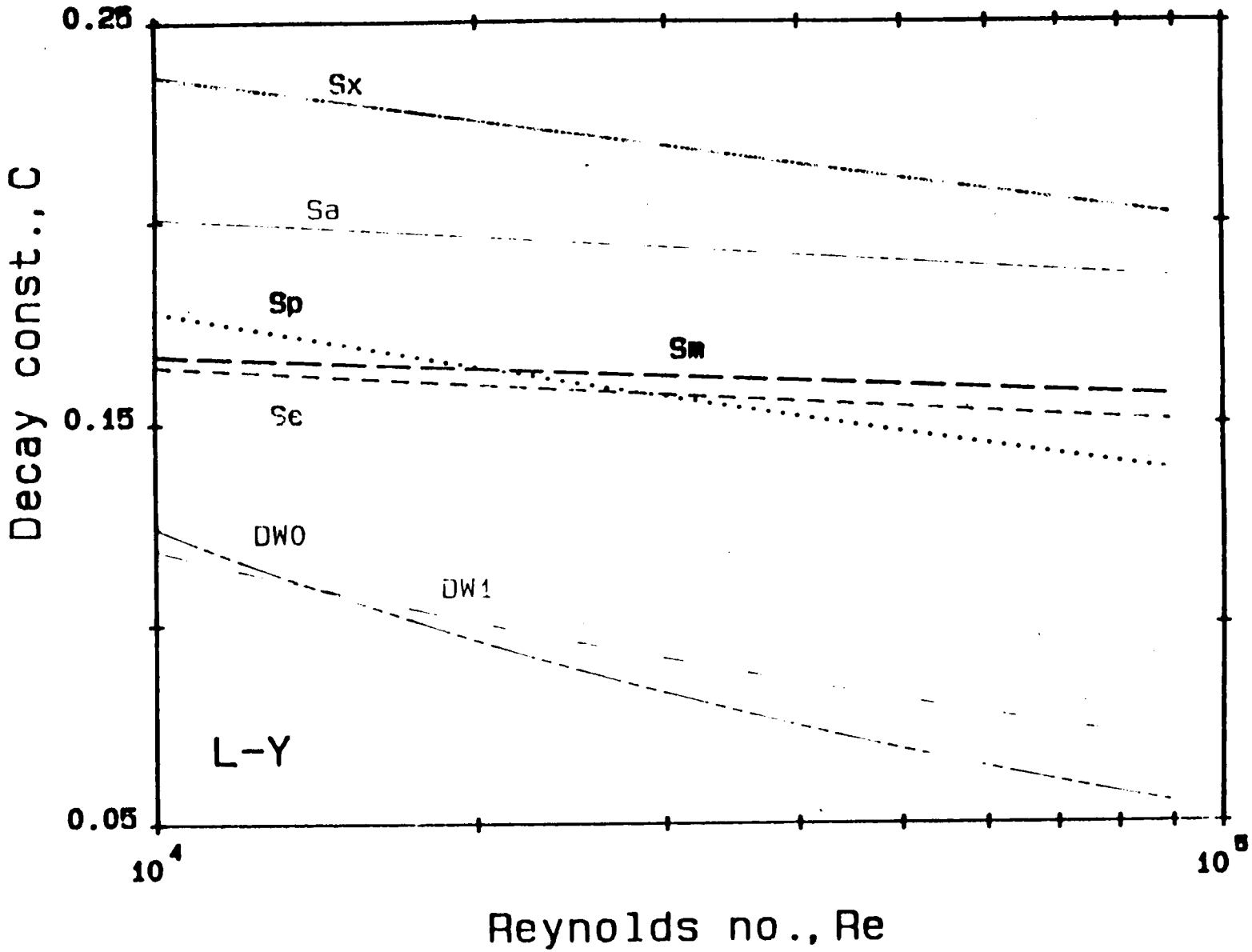

FIGURE 17. Decay Constants of Secondary Flow Prameters Versus Diametral Reynolds Number For The Single Elbow.

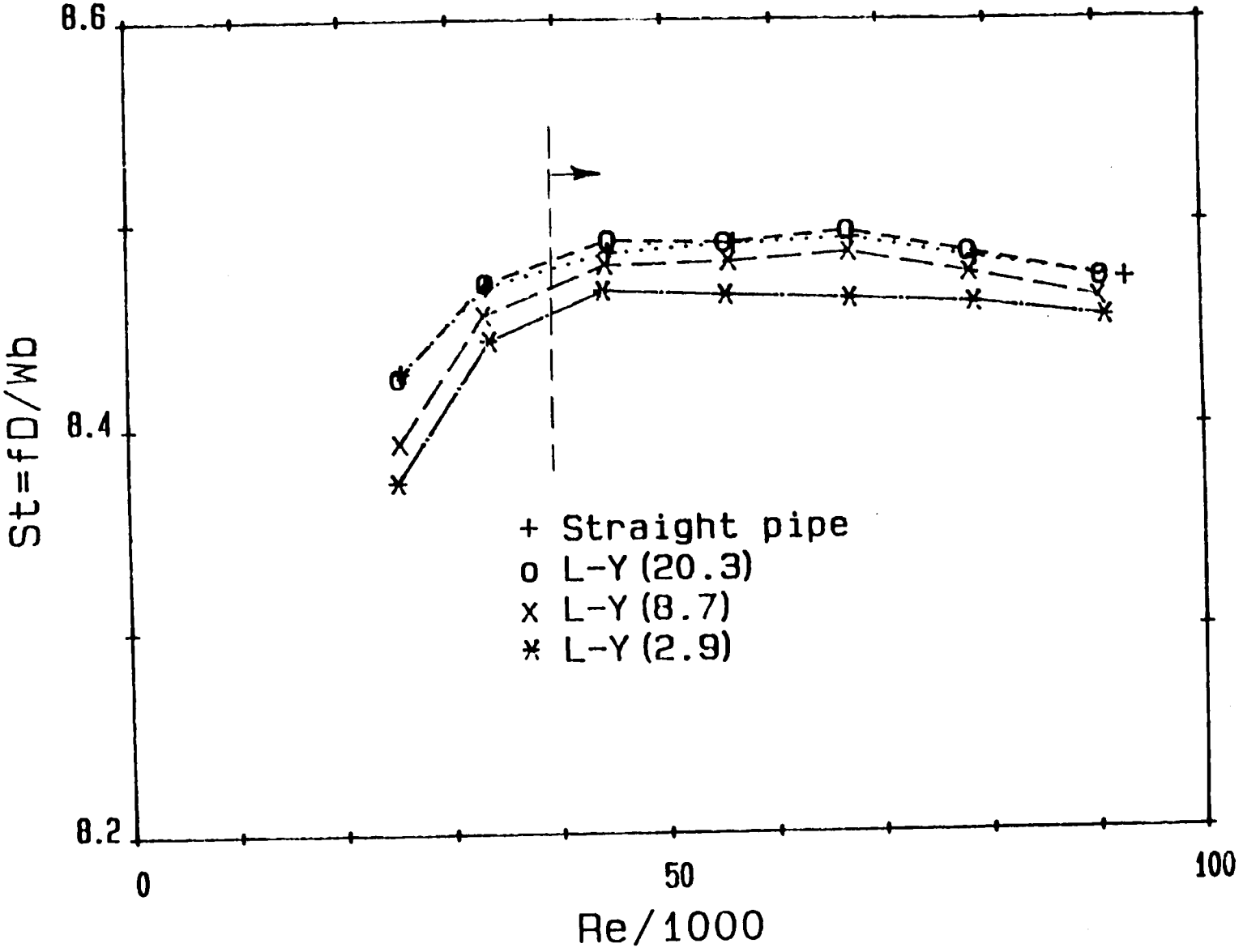

FIGURE 18. Turbine-Type Meter Calibration Data.

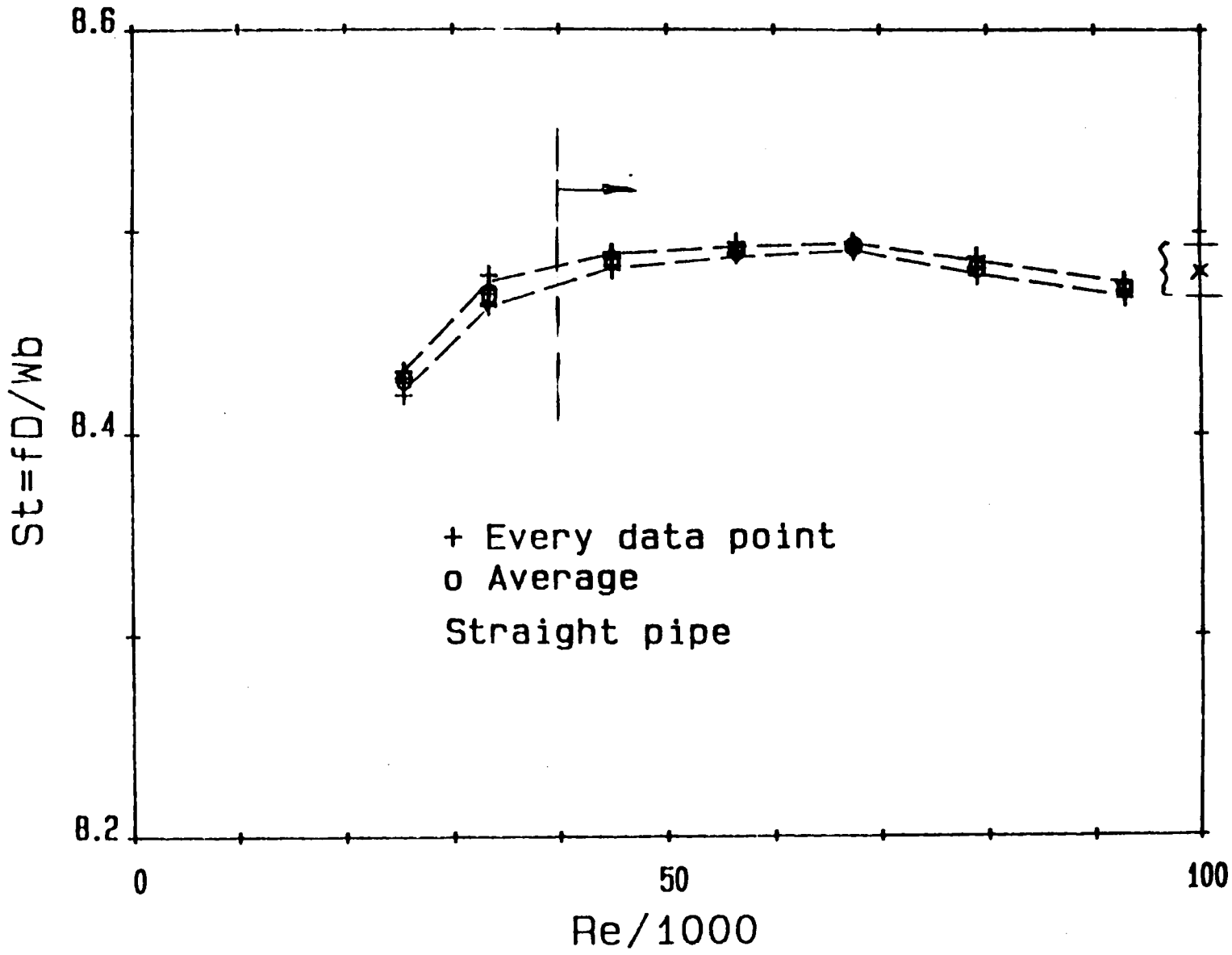

FIGURE 19. Uncertainty Bands About The Calibration Data For The Turbine-Type Flowmeter.

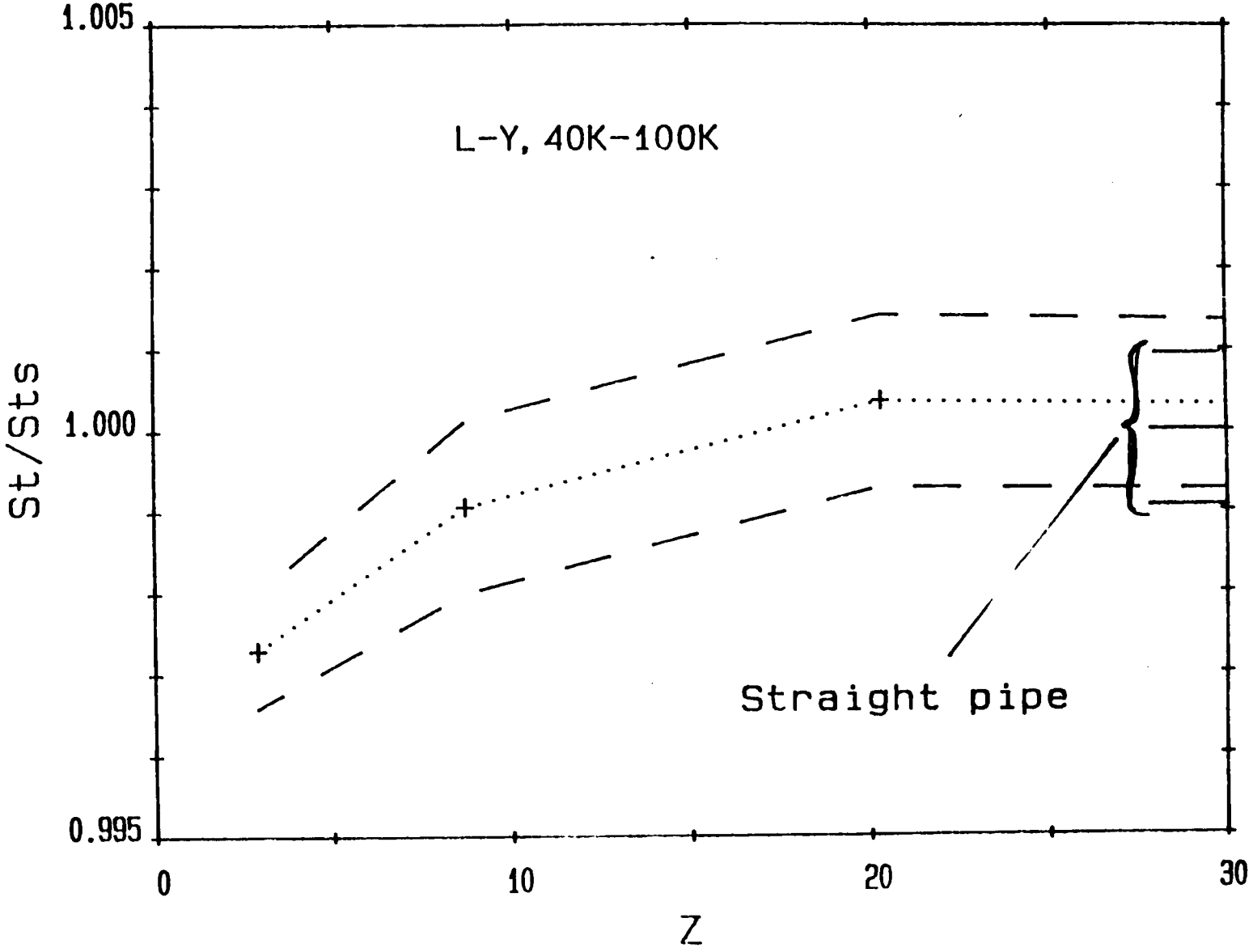

FIGURE 20. Normalized Calibration Data For a Turbine-Type Flowmeter Installed in Non-Ideal Locations.

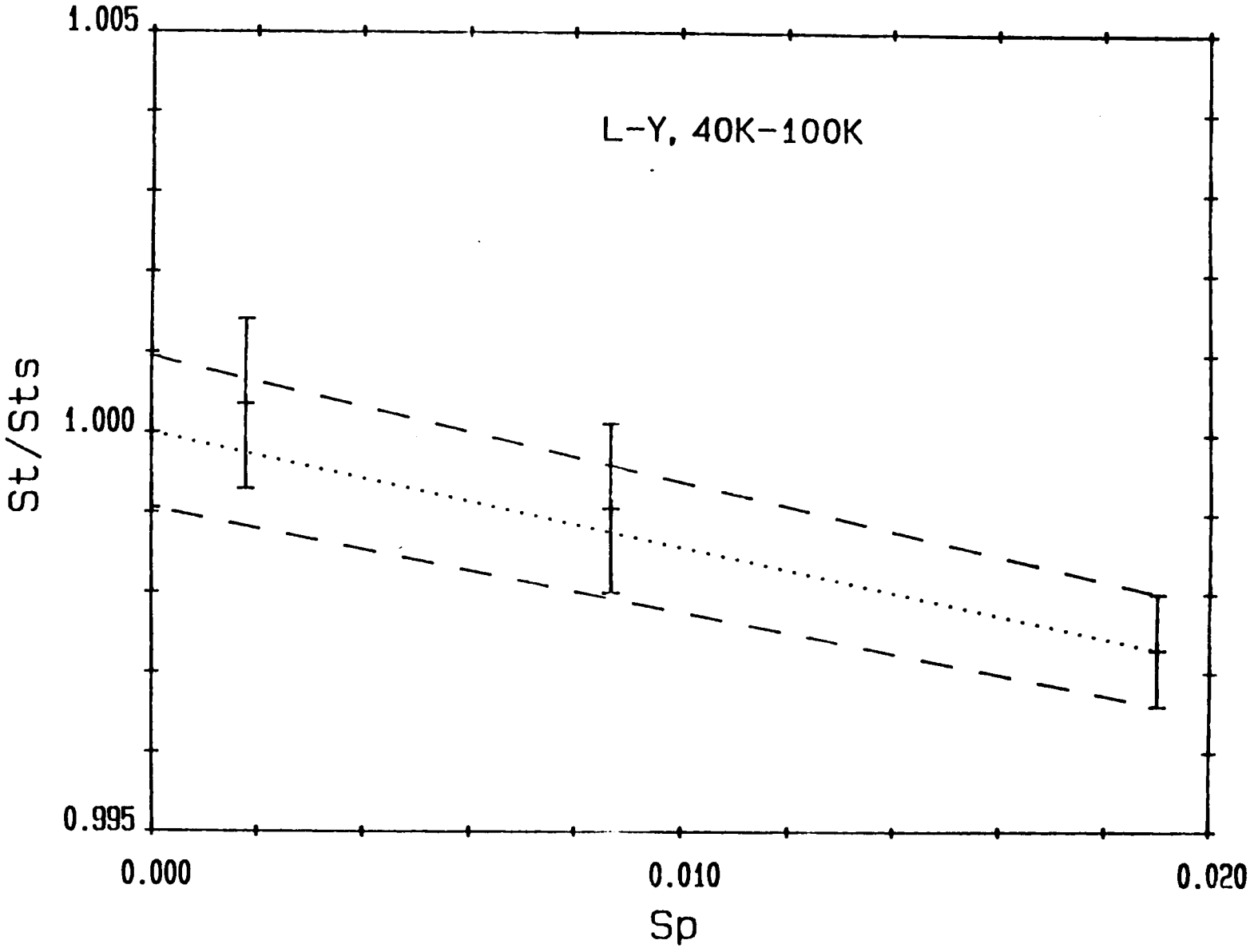

FIGURE 21. Correlation Results For The Pipe Swirl Parameter, S_p For A Turbine-Type Flowmeter.

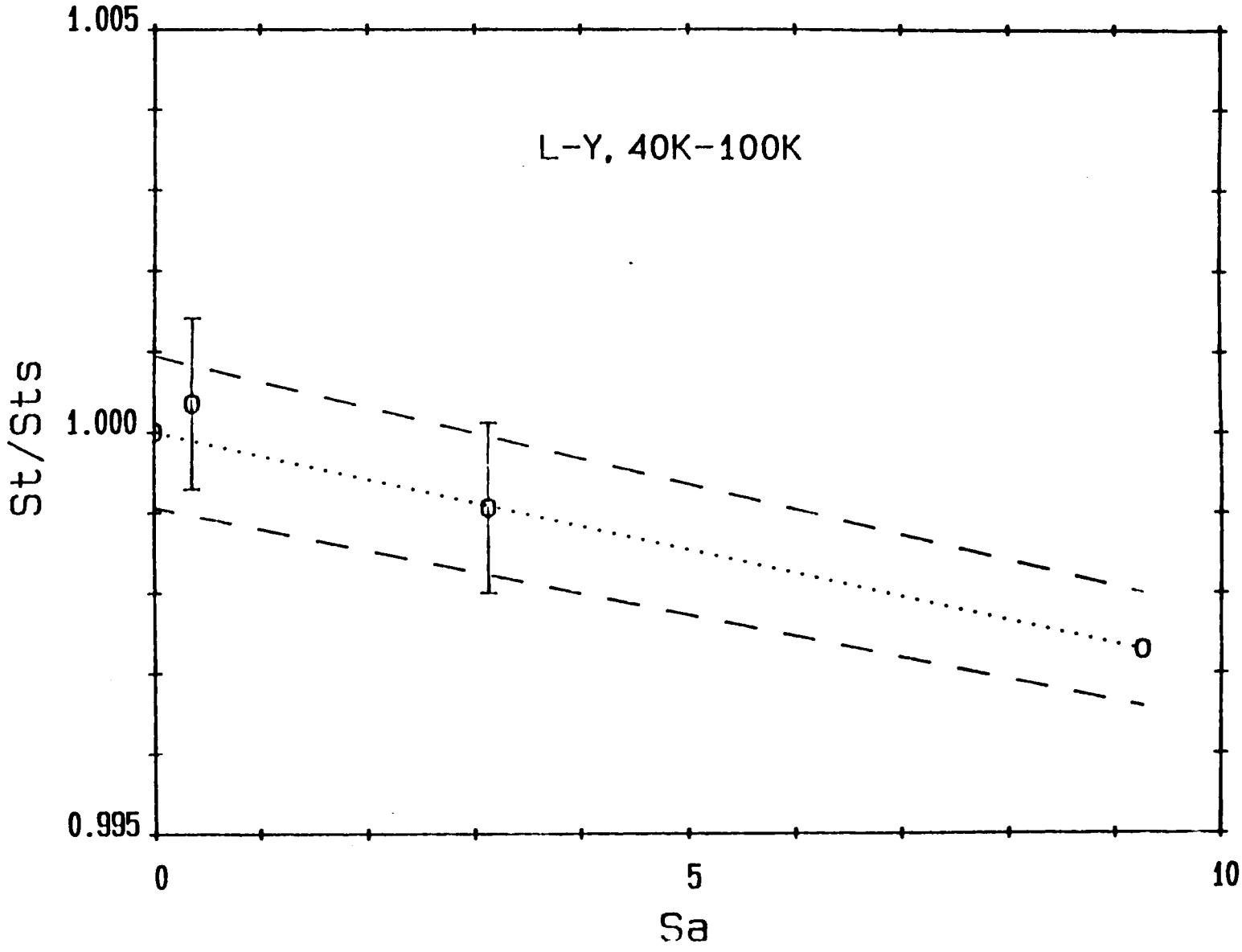

FIGURE 22. Correlation Results For The Skew Angle Parameter, Sa For A Turbine-Type Flowmeter.

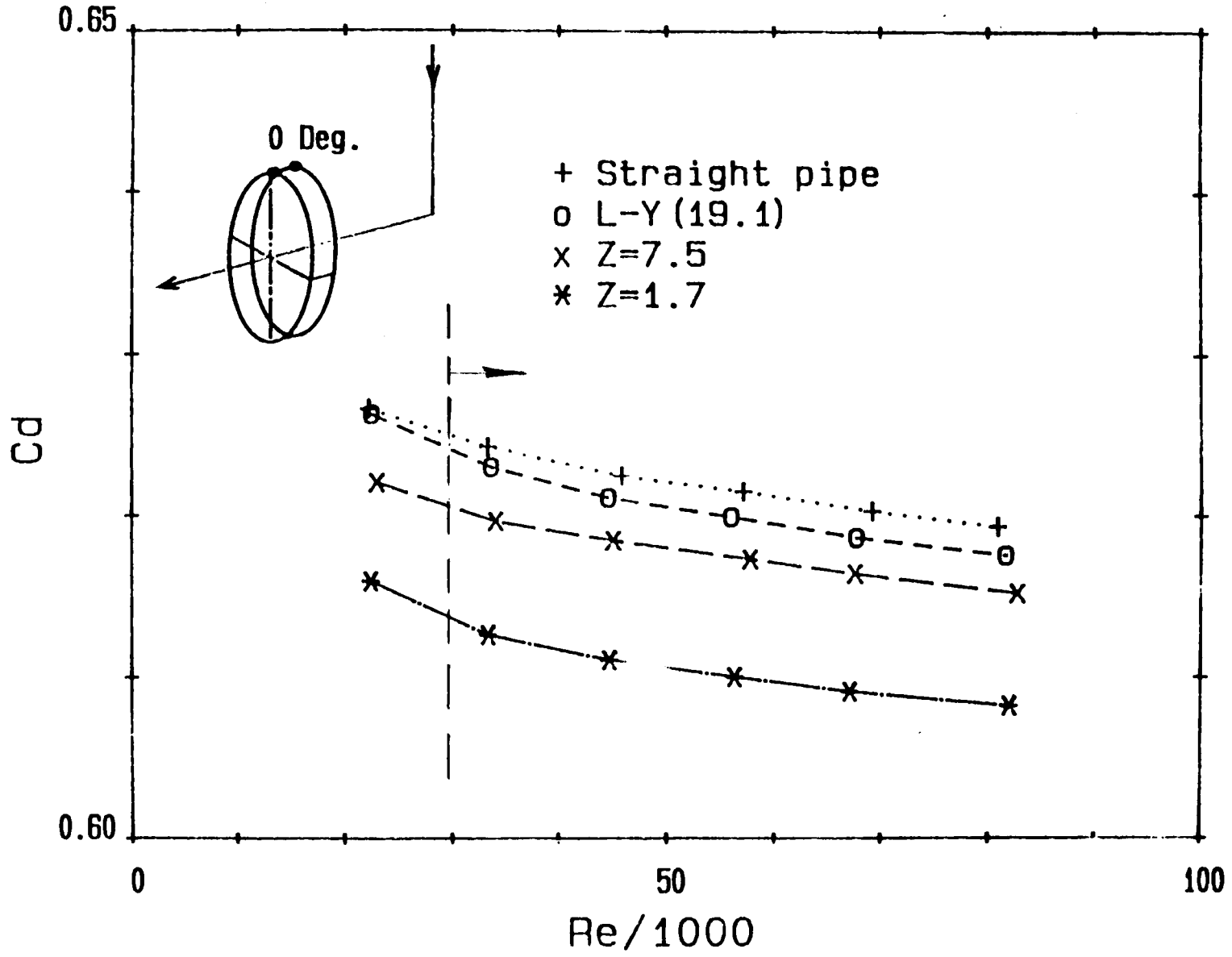

FIGURE 23. Calibration Data For An Orifice-Type Flowmeter Having Beta Ratio 0.500.

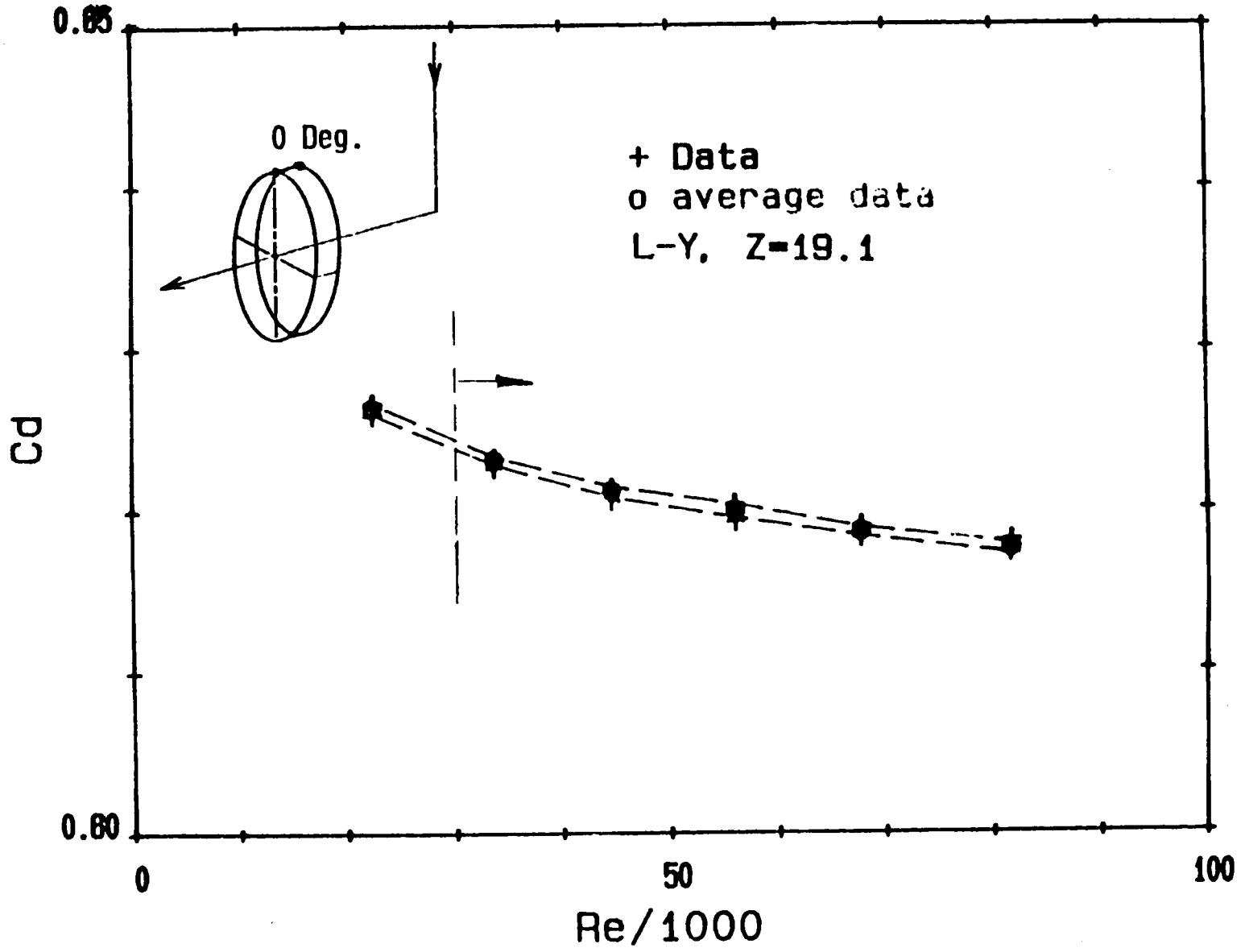

FIGURE 24. Uncertainty Bands About The Calibration Data For The Orifice-Type Flowmeter Having Beta Ratio 0.500.

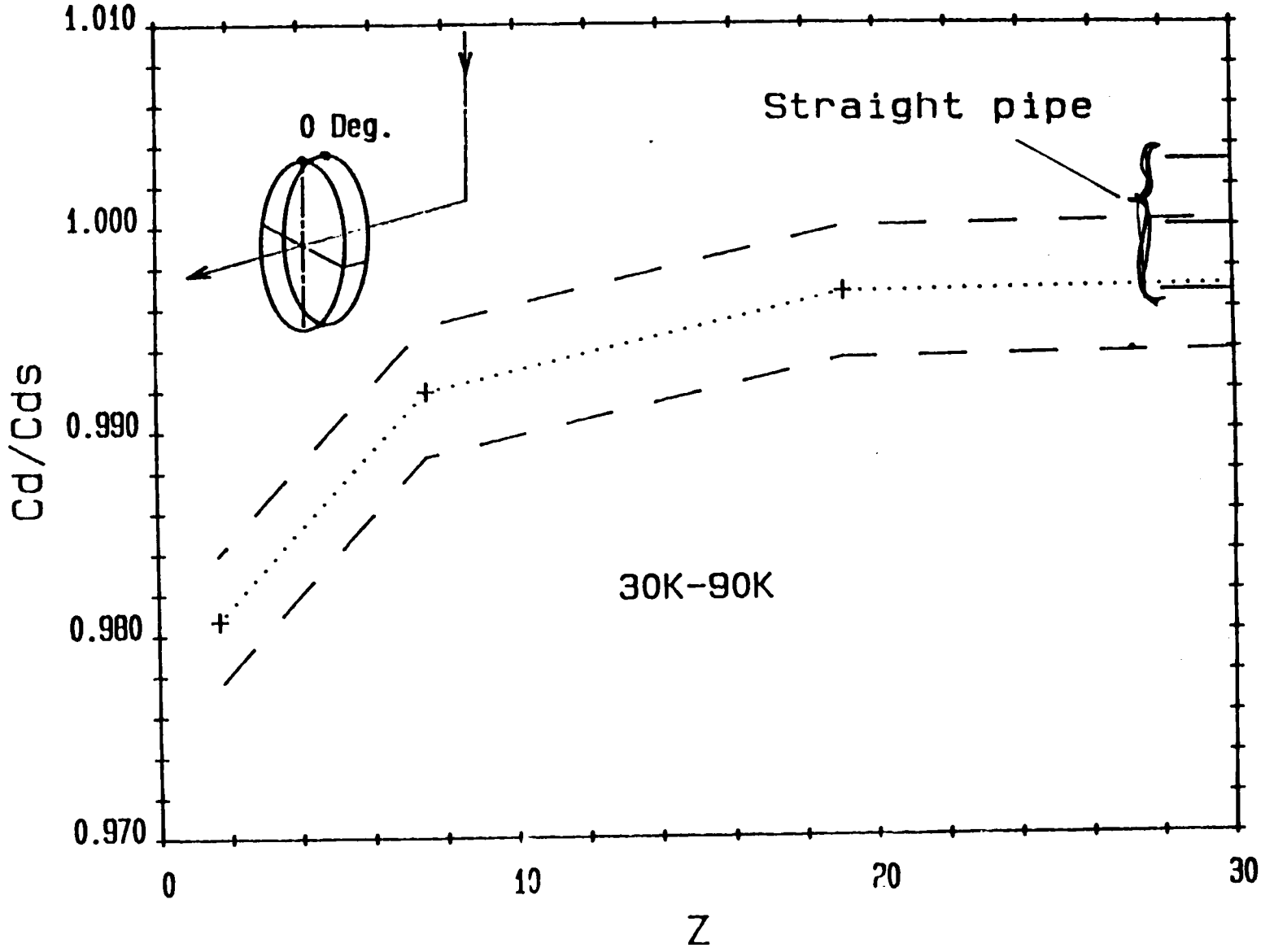

FIGURE 25. Normalized Calibration Data For An Orifice-Type Flowmeter Having Beta Ratio 0.500.

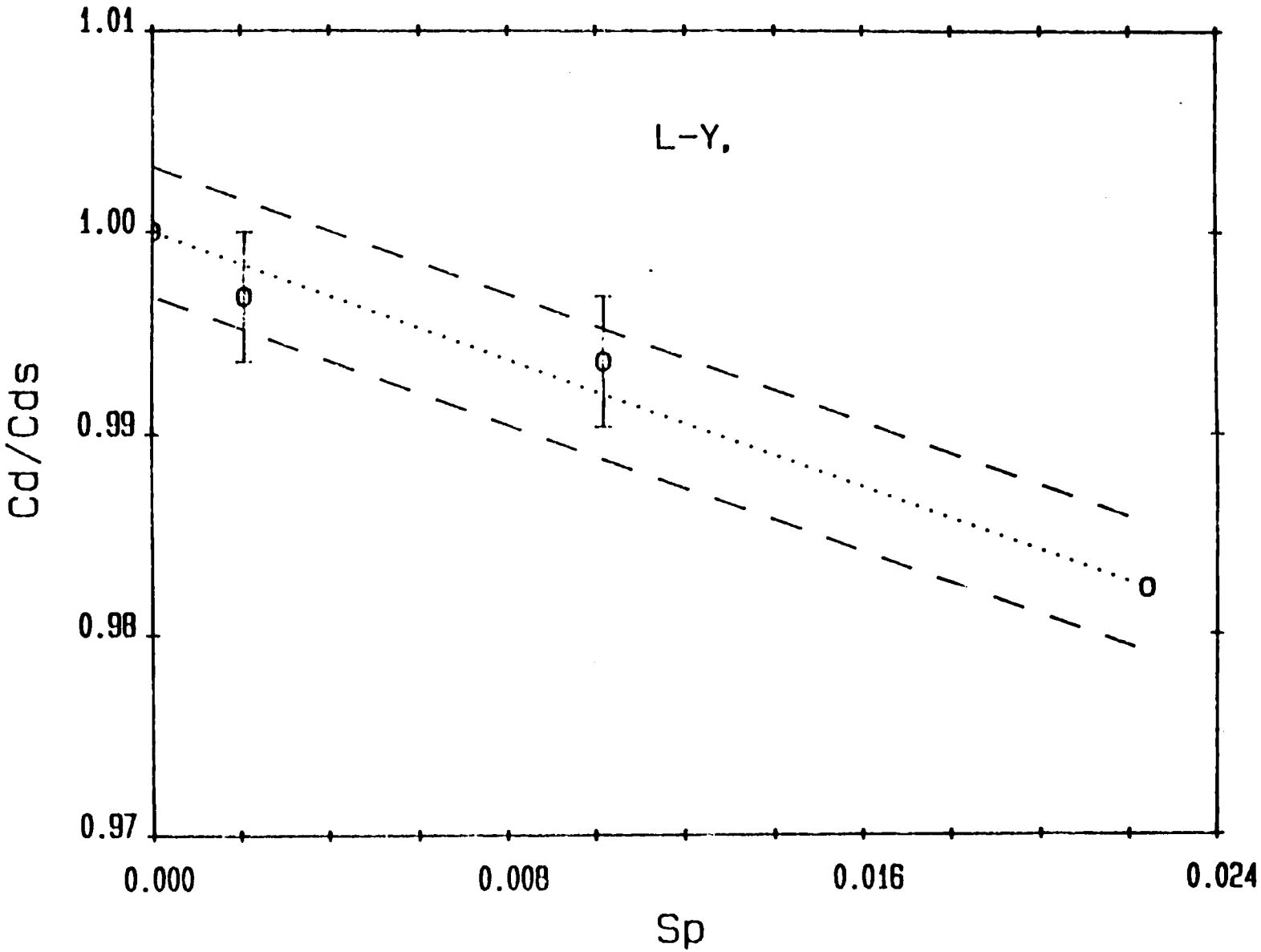

FIGURE 26. Correlation Results For The Pipe Swirl Parameter, S_p, For An Orifice-Type Flowmeter Having Beta Ratio 0.500.

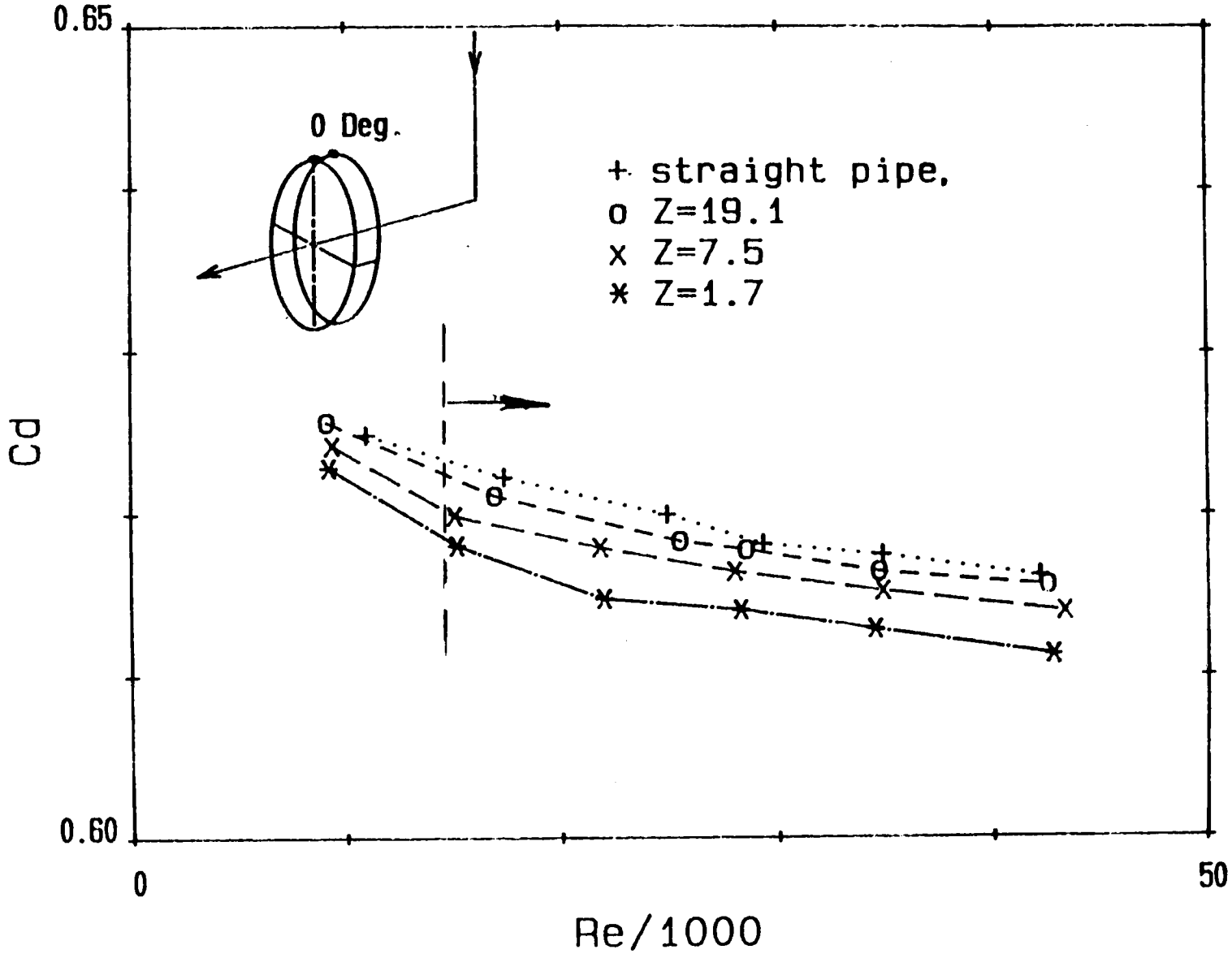

FIGURE 27. Calibration Data For An Orifice-Type Flowmeter Having Beta Ratio 0.363.

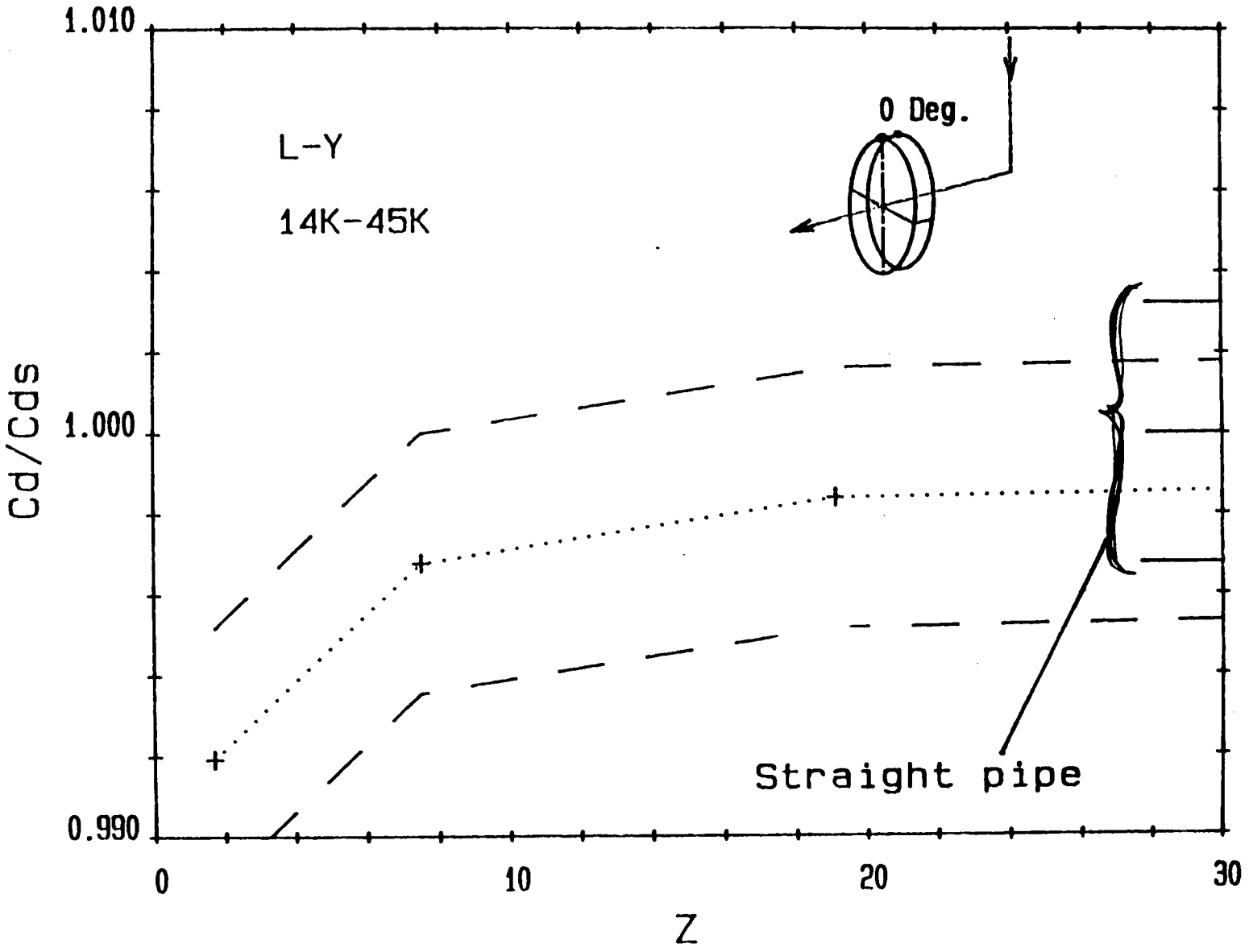

FIGURE 28. Normalized Calibration Data For An Orifice-Type Flowmeter Having Beta Ratio 0.363.

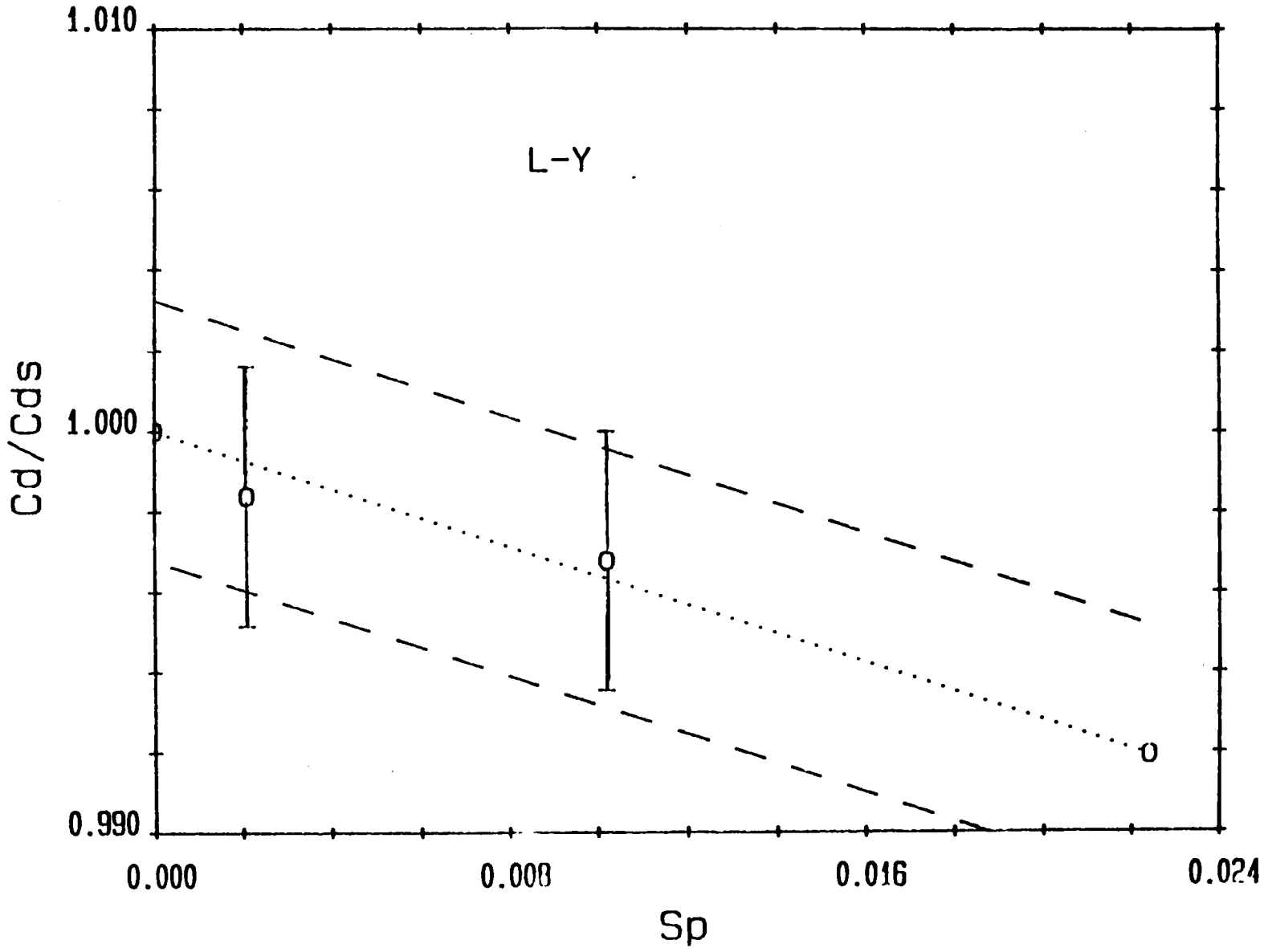

FIGURE 29. Correlation Results For The Pipe Swirl Parameter, S_p, For An Orifice-Type Flowmeter Having Beta Ratio 0.363.

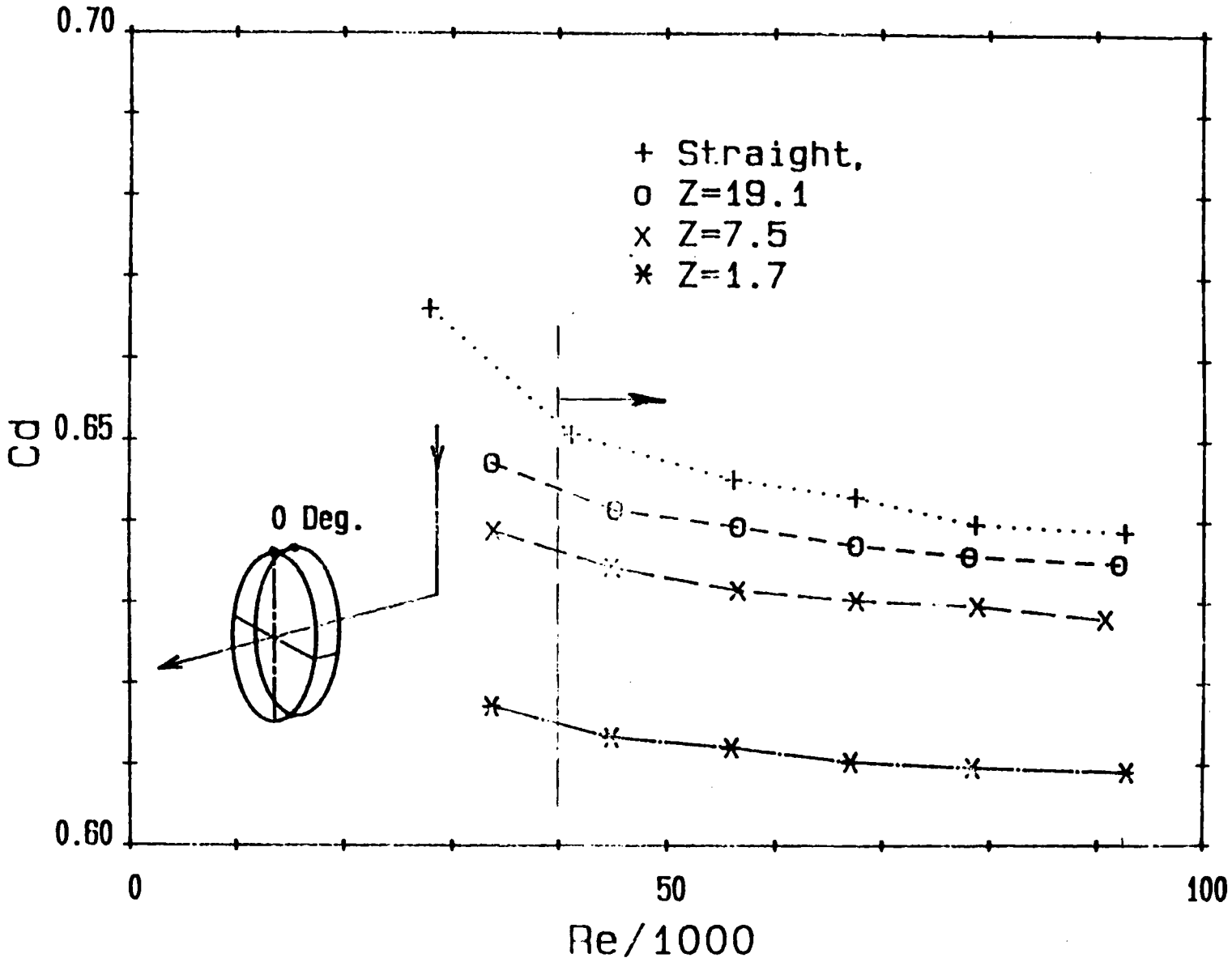

FIGURE 30. Calibration Data For An Orifice-Type Flowmeter Having Beta Ratio 0.750.

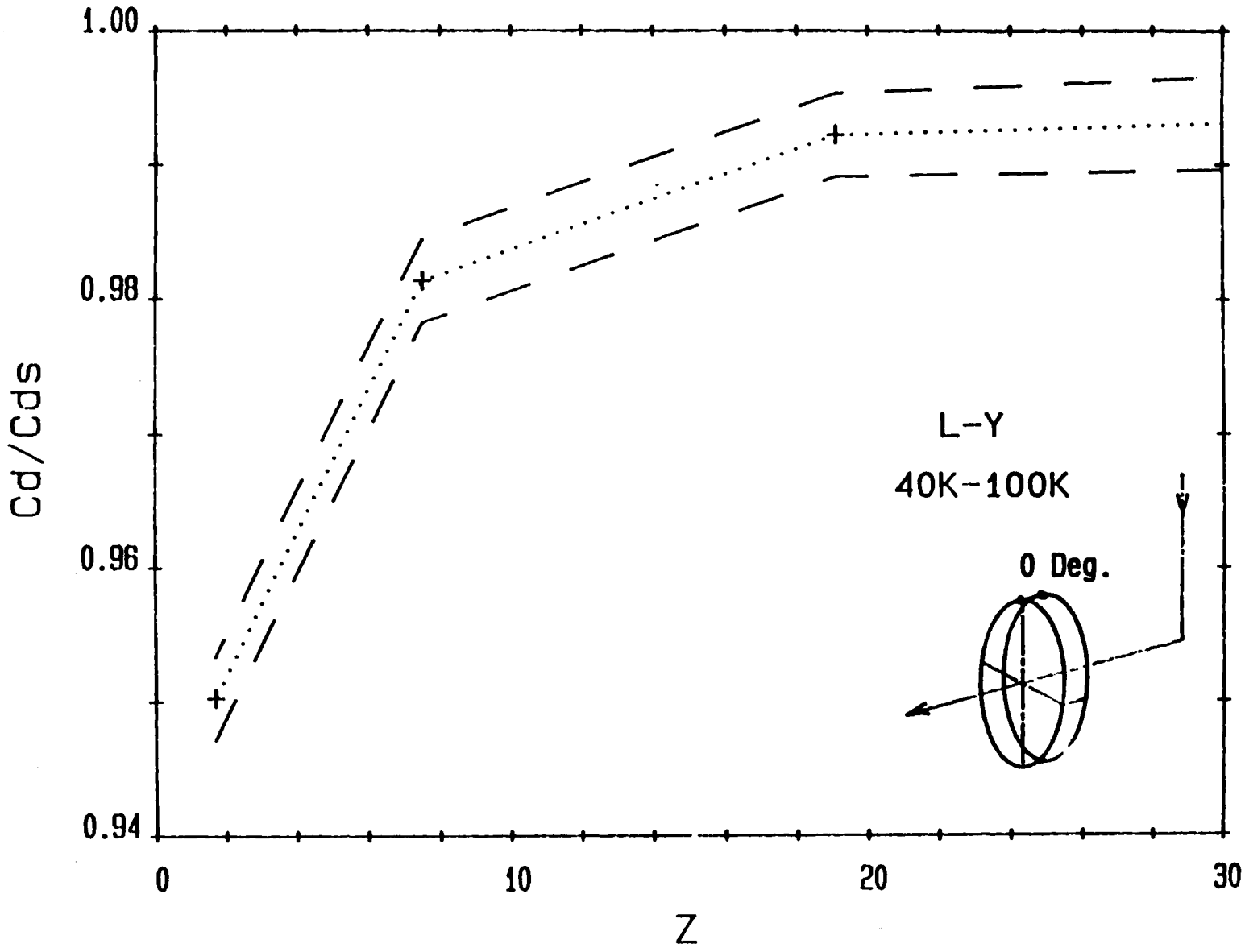

FIGURE 31. Normalized Calibration Data For An Orifice-Type Flowmeter Having Beta Ratio 0.750.

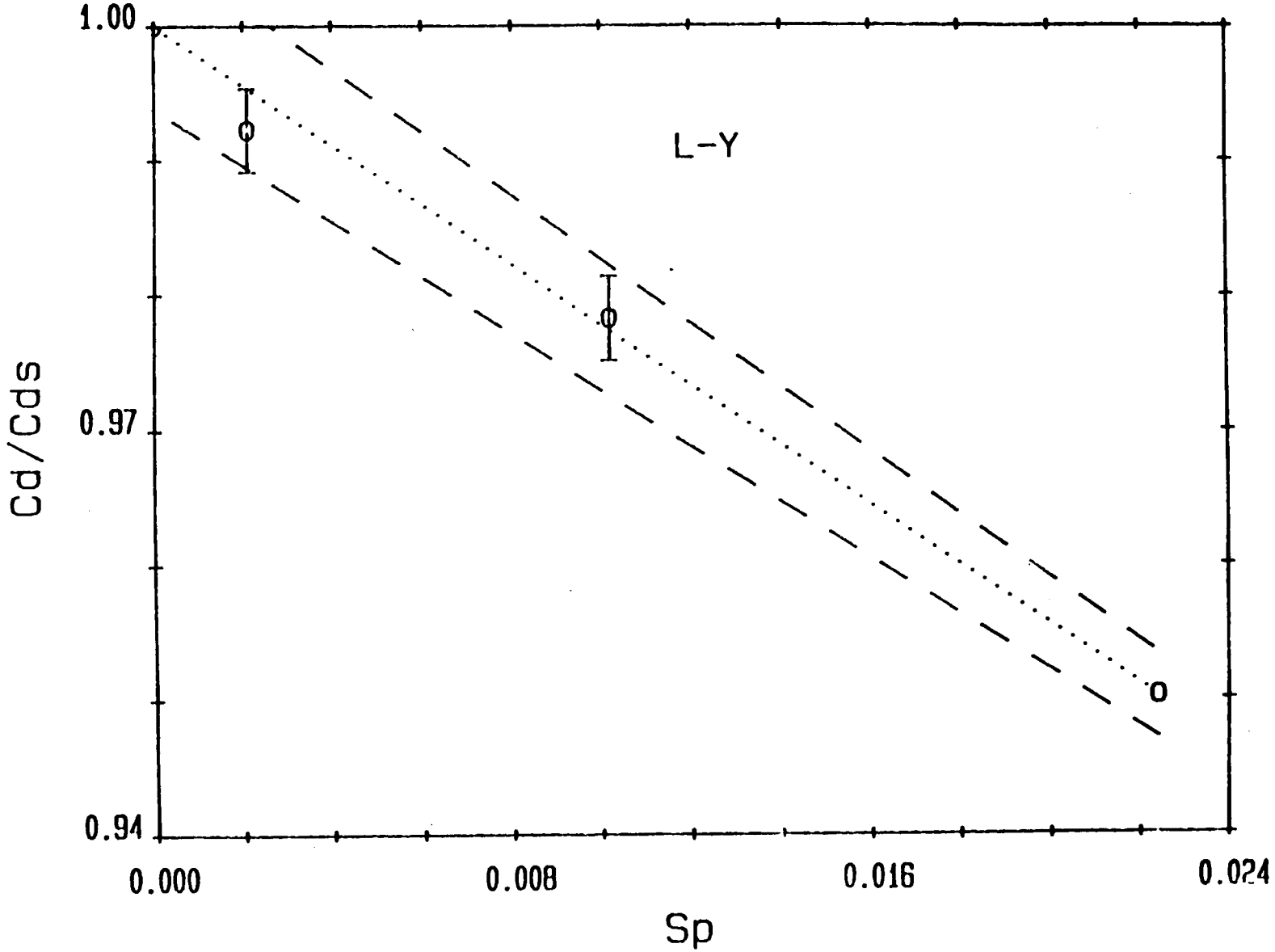

FIGURE 32. Correlation Results For The Pipe Swirl Parameter, S_p, For An Orifice Type Flowmeter Having Beta Ratio 0.750.

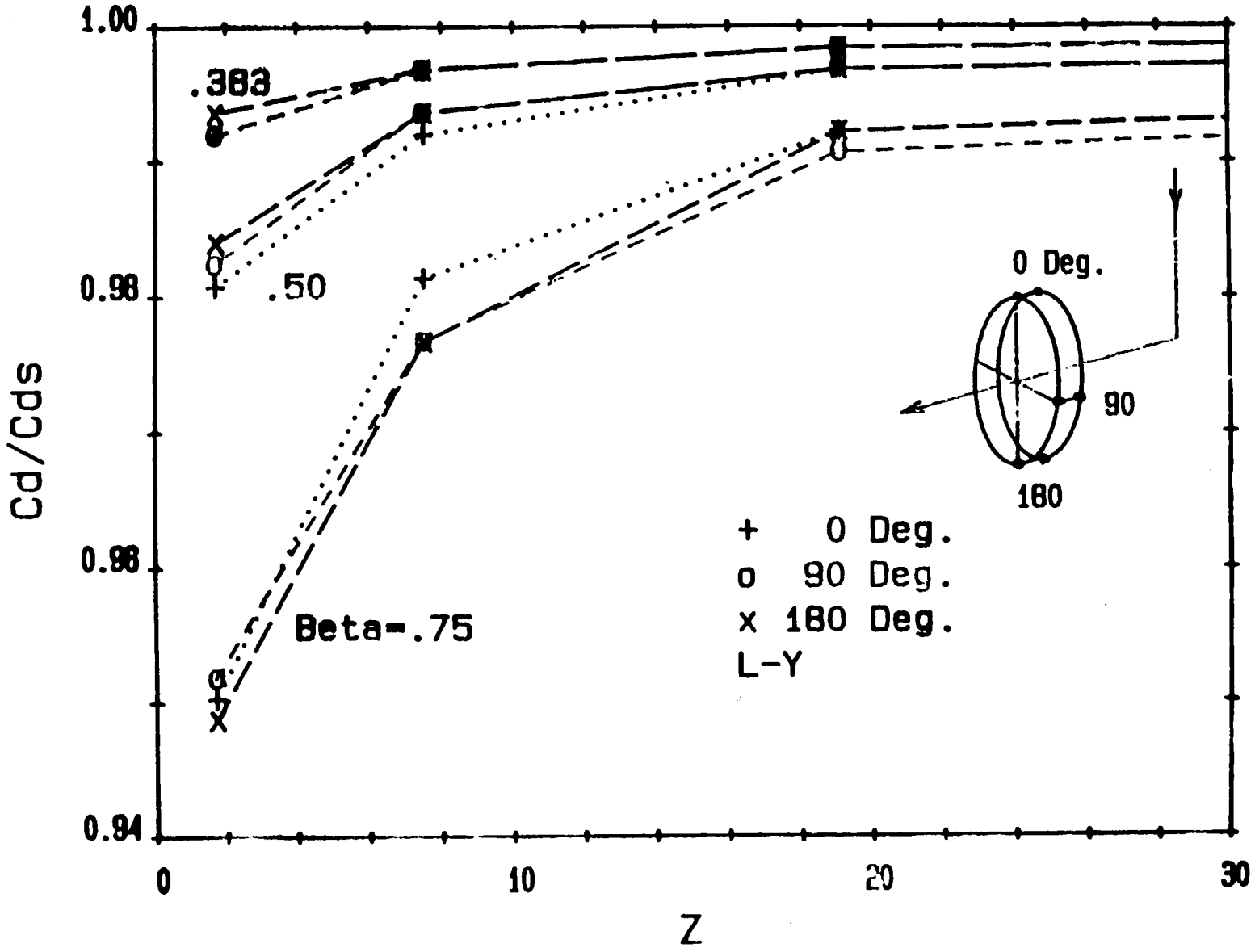

FIGURE 33. Normalized Performance For An Orifice-Type Flowmeter For Different Beta Ratios and For Different Pressure Tap Locations.

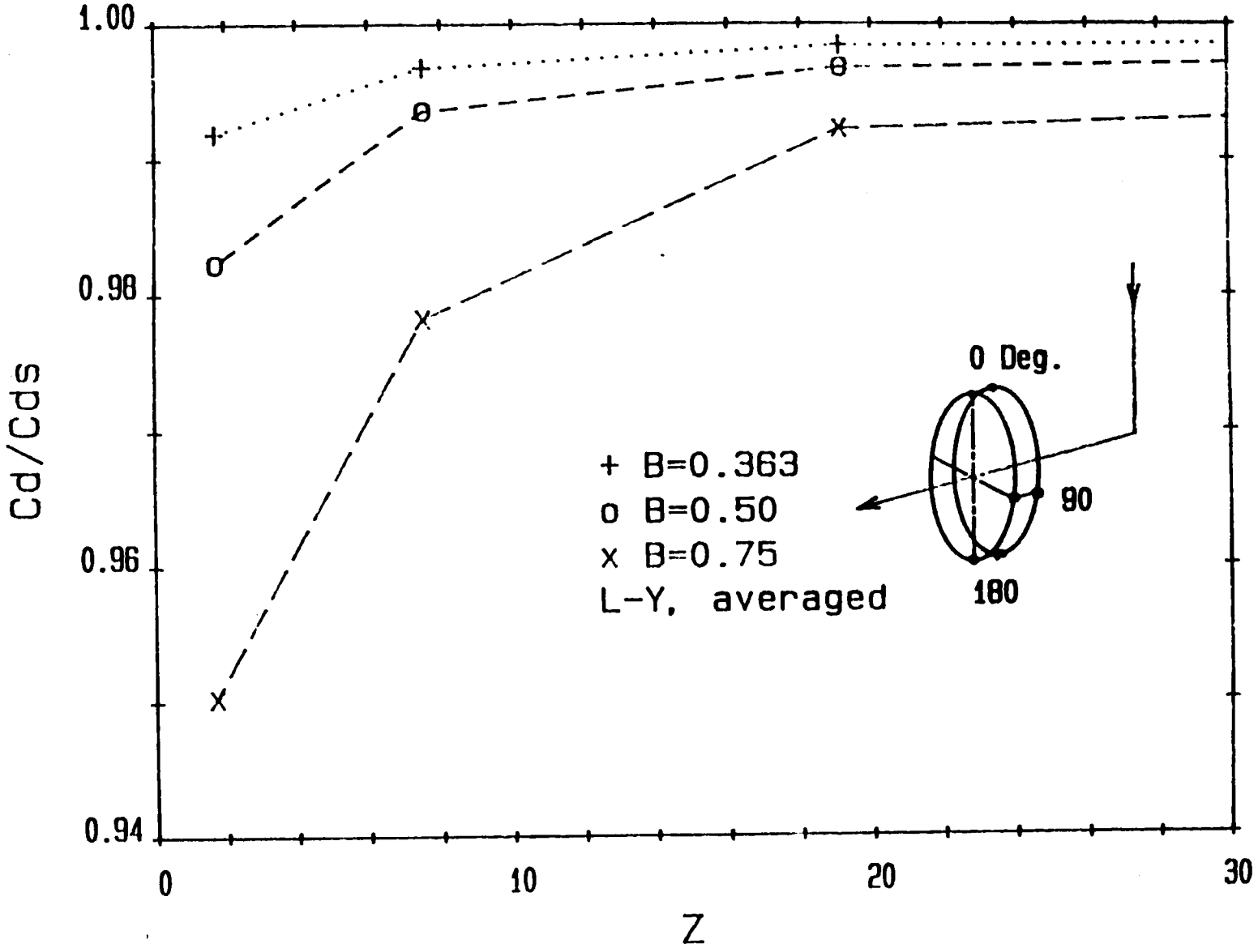

FIGURE 34. Normalized Performance For An Orifice-Type Flowmeter For Different Beta Ratios Averaged Over Three Tap Locations.

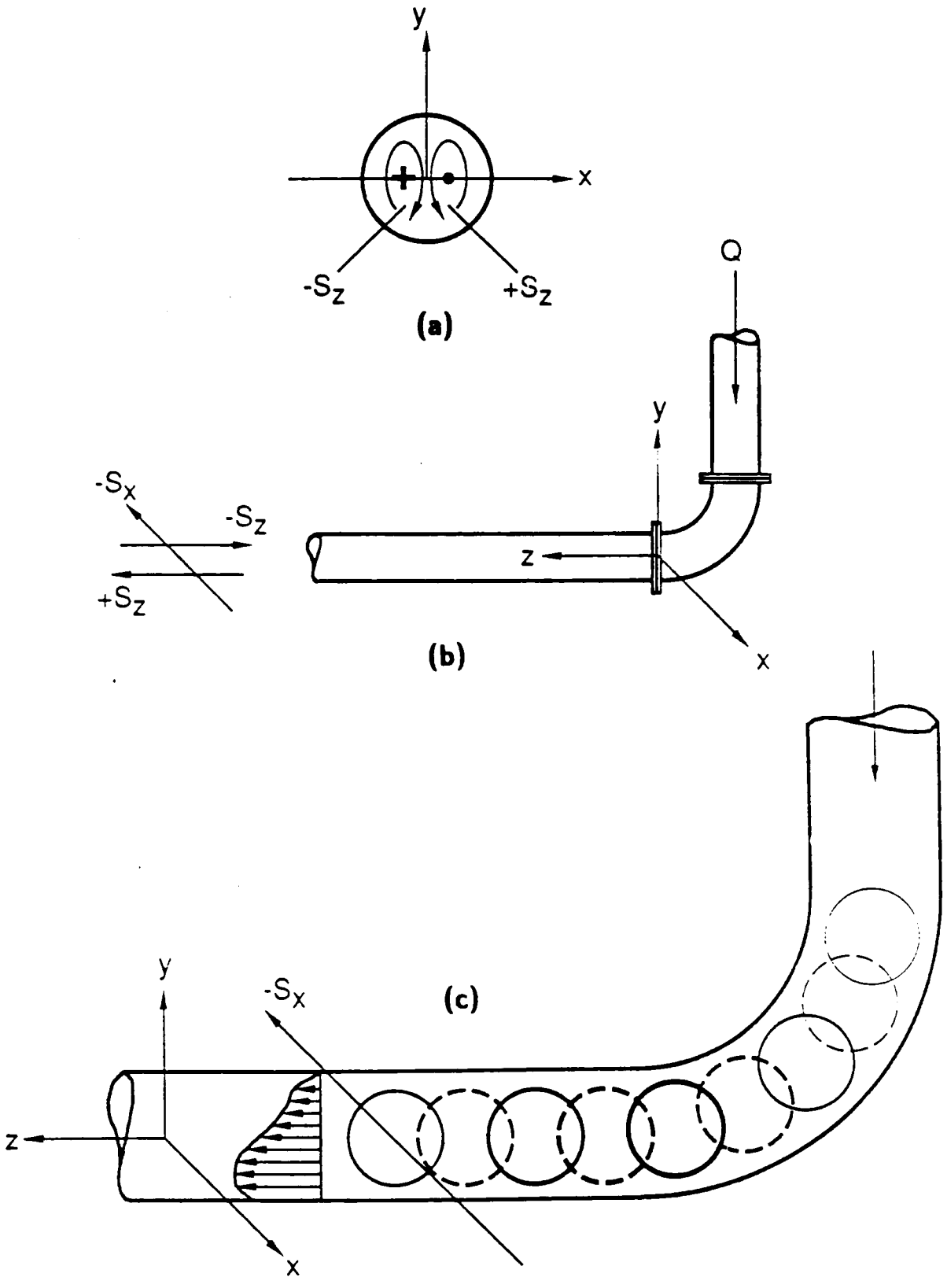

FIGURE 35. Sketches of Vorticity Vectors In The Secondary Flow Produced By A Single Elbow.

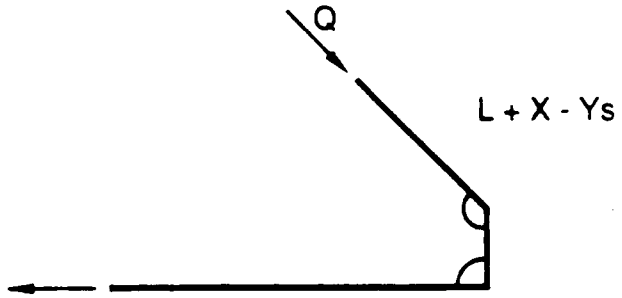

(a)

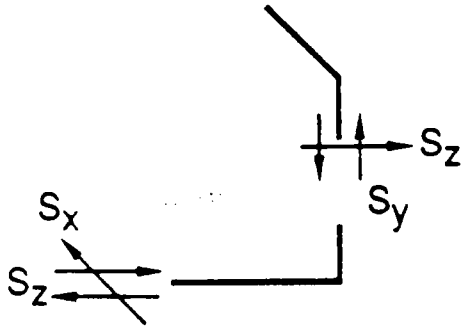

(b)

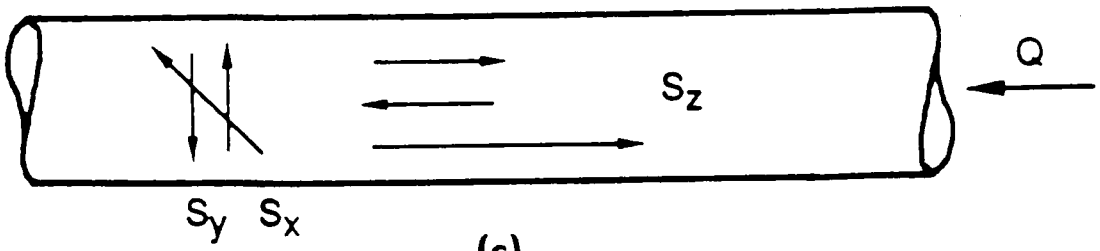

(c)

FIGURE 36. Sketches of Vorticity Vectors In The Secondary Flow Produced By Two Elbows-Out-Of-Plane.

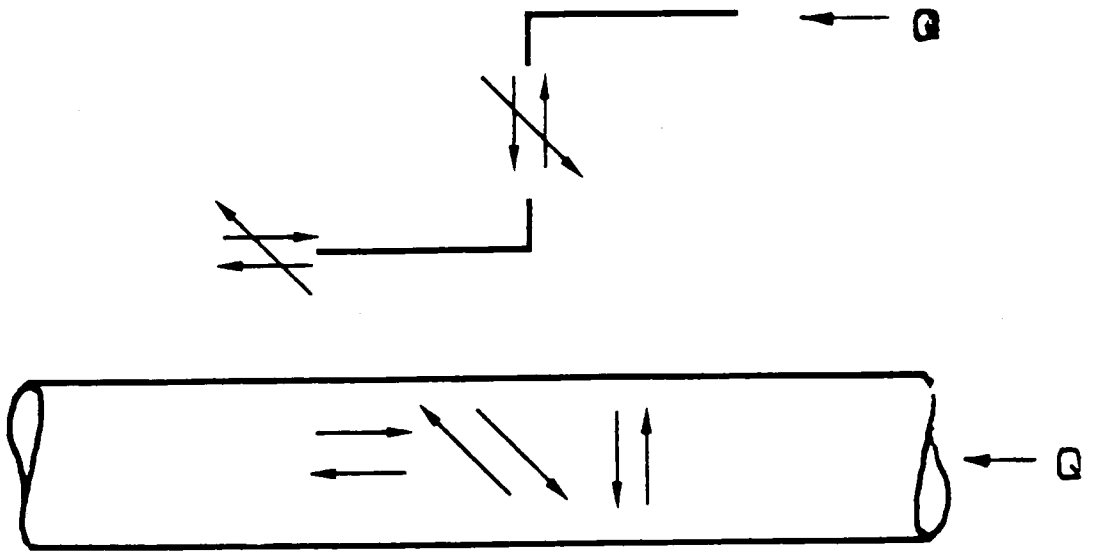

a) Same direction, L + Z - Ys

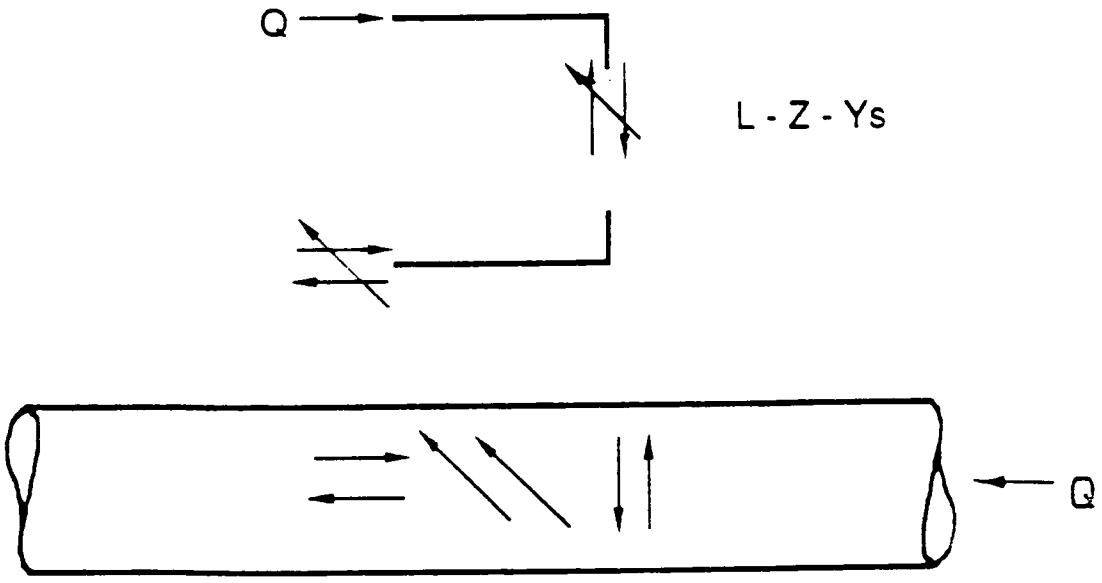

b) Reversed Direction, L - Z - Ys

FIGURE 37. Sketches of Vorticity Vectors In The Secondary Flow Produced By Two Elbows-In-Plane.

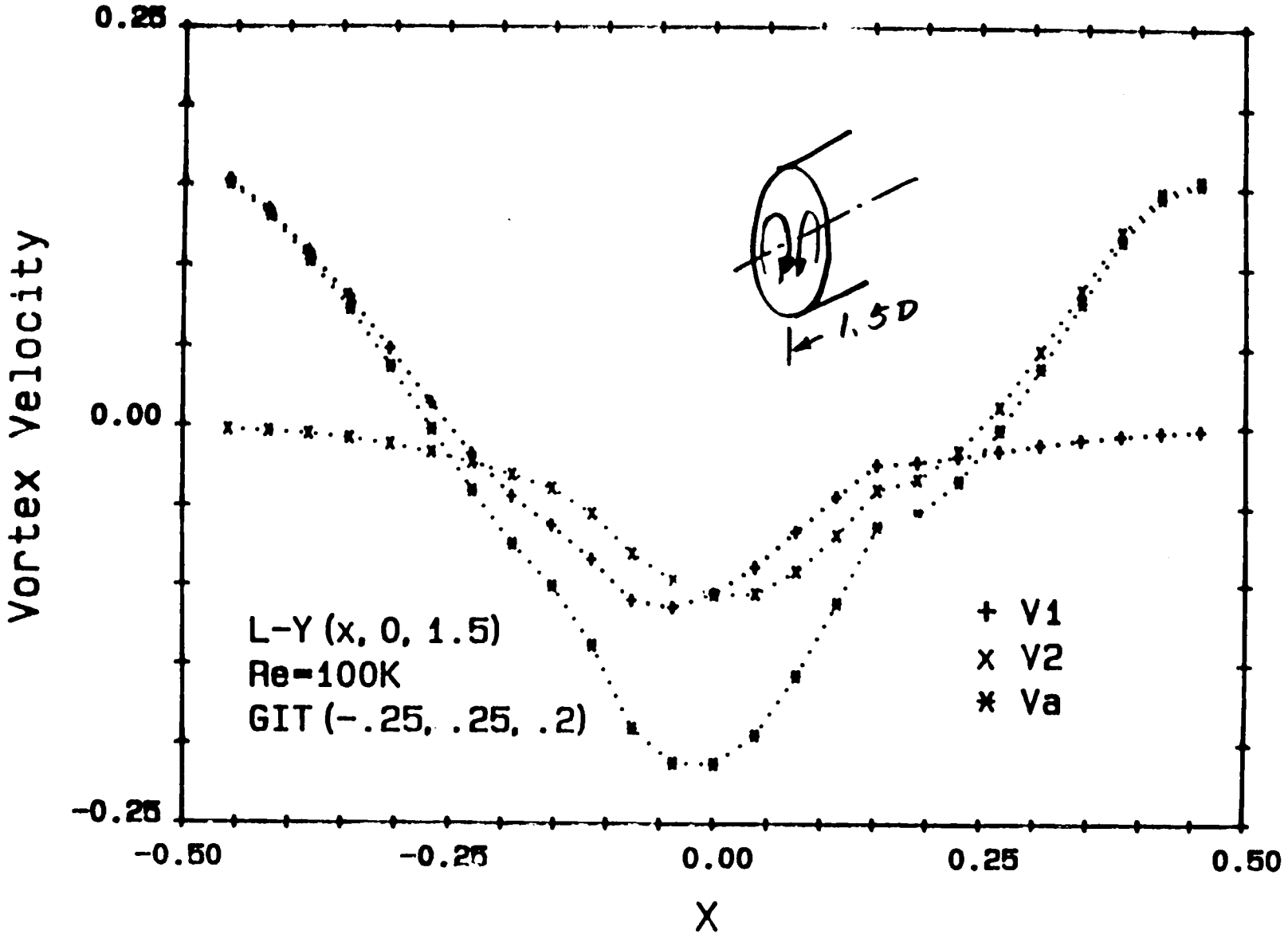

FIGURE A1. Mean Velocity Distributions For A G.I. Taylor Vortex.

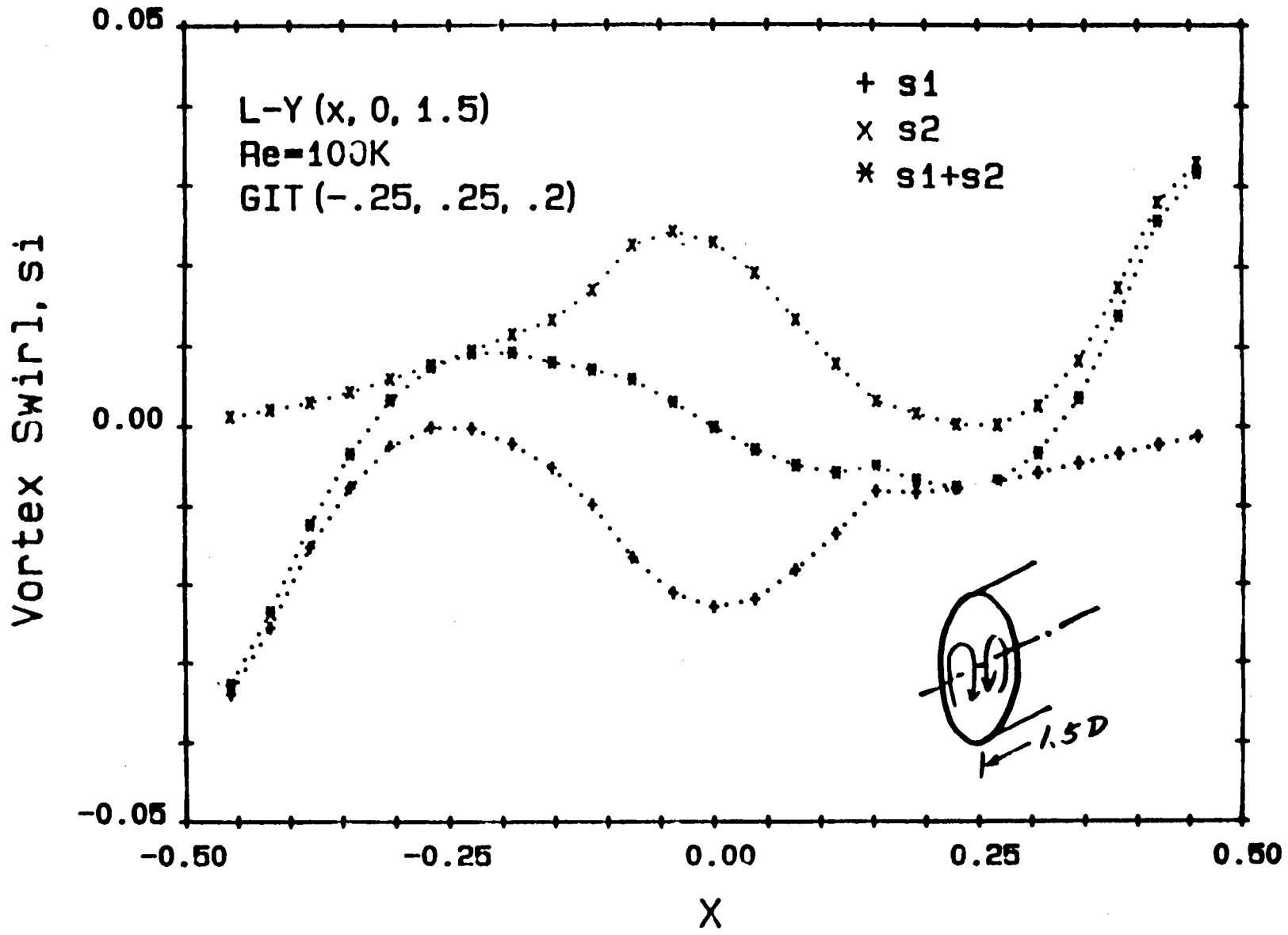

FIGURE A2. Distributions of Vortex Swirl, S_i For A G.I. Taylor Vortex.

NBS-114A (REV. 2-8C)

U.S. DEPT. OF COMM. **BIBLIOGRAPHIC DATA SHEET** (See instructions)	1. PUBLICATION OR REPORT NO. NISTIR-89/4080	2. Performing Organ. Report No.	3. Publication Date APRIL 1989

4. TITLE AND SUBTITLE

NIST's Industry-Government Consortium Research Program on Flowmeter Installation Effects: Report of Results from the Research Period Jan.-July 1988

5. AUTHOR(S)

G.E. Mattingly, T.T. Yeh

6. PERFORMING ORGANIZATION (If joint or other than NBS, see instructions)

NATIONAL BUREAU OF STANDARDS
DEPARTMENT OF COMMERCE
WASHINGTON, D.C. 20234

7. Contract/Grant No.

8. Type of Report & Period Covered

9. SPONSORING ORGANIZATION NAME AND COMPLETE ADDRESS (Street, City, State, ZIP)

10. SUPPLEMENTARY NOTES

☐ Document describes a computer program; SF-185, FIPS Software Summary, is attached.

11. ABSTRACT (A 200-word or less factual summary of most significant information. If document includes a significant bibliography or literature survey, mention it here)

This report presents results produced in a consortium-sponsored research program on Flowmeter Installation Effects. This project is a collaborative one that has been underway for three years; it is supported by an industry-government consortium that meets twice yearly to review and discuss results and to plan subsequent phases of the work. This report contains the results and conclusions of the recent meeting of this consortium at NIST-Gaithersburg, MD on Aug. 1988. Specific results included in this report include research results for the pipe flow from a conventional, long radius elbow:

1. the distributions of the mean and the turbulence velocities in the axial and vertical directions,
2. the pressure loss measurements,
3. the performance of selected types of flowmeter installed downstream of this elbow, and
4. the demonstration that satisfactory performance for the selected meters can be predicted using the research results of this study.

12. KEY WORDS (Six to twelve entries; alphabetical order; capitalize only proper names; and separate key words by semicolons)

Calibrations; Installation Effects; LDV flow measurements; pipeflow profiles; swirl; turbulence; vorticity

13. AVAILABILITY

☒ Unlimited

☐ For Official Distribution. Do Not Release to NTIS

☐ Order From Superintendent of Documents, U.S. Government Printing Office, Washington, D.C. 20402.

☒ Order From National Technical Information Service (NTIS), Springfield, VA. 22161

14. NO. OF PRINTED PAGES

77

15. Price

$14.95

USCOMM-DC 6043-P80